# Acoustoelectric Transport in Graphene

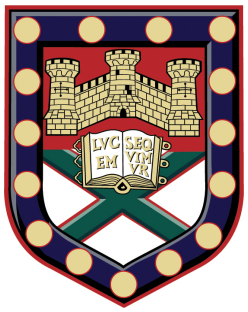


Submitted by Lokeshwar Bandhu to the University of Exeter

as a thesis for the degree of

Doctor of Philosophy in Engineering

In May 25, 2015.



I certify that all material in this thesis which is not my own work has been identified and that no material has previously been submitted and approved for the award of a degree by this or any other University.

Signature .....

# Abstract

The acoustoelectric effect in graphene is studied in a graphene/lithium niobate hybrid system, which was prepared by transferring large area single-layer graphene grown on copper onto lithium niobate SAW devices. The transfer of momentum from the surface acoustic waves (SAWs), generated on the surface of the lithium niobate, to the carriers in graphene results in an attenuation and velocity shift of the wave, and gives rise to an acoustoelectric current. The acoustoelectric current, and the amplitude and velocity of the SAW are measured using a sourcemeter and oscilloscope, respectively.

Macroscopic acoustoelectric current flowing over several hundred micrometers is demonstrated in graphene, which is measured to be directly proportional to the SAW intensity and frequency at room temperature. A relatively simple classical relaxation model, which describes the piezoelectric interaction between SAWs and the carriers in a two-dimensional electron system, is used to explain the experimental observations. The investigation of the acoustoelectric current as a function of temperature demonstrates the ability of SAWs of different wavelengths to probe graphene at different length scales.

By tuning the conductivity of the graphene through the use of a top gate, voltage-controlled phase (velocity) shifters are demonstrated. The acoustoelectric current measured as a function of gate voltage demonstrates that an equal density of electrons and holes are transported at the charge neutrality point, reflecting the unique properties of graphene.

# Acknowledgements

I have had the privilege of working with a wonderful group of people, without whose guidance and support this work would not have been possible.

Firstly, I would like to express my deepest gratitude to Professor Geoffrey Nash, whose guidance and motivation has been the major driving force during this work. His great knowledge of the subject, enthusiasm for exploring new ideas, and mentoring have immensely helped in developing my scientific rigour. I only hope some of his research skills and work ethics have rubbed off on me. At times, the experiments were frustrating, but his patience to withstand the failures encouraged me to persevere. His cheerful presence has been a constant during all these years, which made it an absolute joy to work in his group.

I had the opportunity to work and learn from some experienced professionals, including the post-docs in our group. It would have been difficult to survive the first year of research without the helpful company of Dr Loretta Lawton. I am thankful for her support in getting acquainted with the clean-room and other lab equipments. I would also like to extend my gratitude to Dr Choon How Gan, Dr Isaac Luxmoore and Dr Penglei Li for their insightful discussions. Although I did not work directly with them, but those discussions improved my understanding and I appreciate their patience in answering and explaining my often silly questions.

I had a great time with my fellow graduate students Benjamin Ash, Nathan Mahlmeister and Tim Poole in the group. Their support and kind co-operation in managing the time on lab equipments is also appreciable. I am grateful to Tim Poole for kindly proof-reading most of this thesis, which improved my writing skills. I would also like to thank all the people I worked with in Physics clean-room, without their assistance I would not have developed the technical expertise required for the device fabrication.

Off the research field, I am highly indebted to Dr Bharani Pakki and his family for helping me out when I broke my arm. The injury turned out to be a great excuse to enjoy his hospitality and delicious food. Apart from that, his experience and words of wisdom have been consistently supportive. A special thanks to Laura Colombo for being so understanding and caring during my injury. Also, her support and encouragement provided the necessary impetus during the exhaustive periods of writing. I consider myself lucky to be surrounded with a great bunch of friends in Atul, Sneha, and Varun, with whom I have shared some priceless moments that I am going to cherish for long. The celebration of all the festivals, birthdays and special occasions together made me feel slightly closer to home. My apologies and sincere thanks to all the people who are not named here, for the list is too long, but they deserve a mention as they have etched a beautiful Exeter in my memories forever.

I am extremely grateful to my family and relatives whose blessings and prayers have always been with me. I would not have achieved any landmark with my little effort if not for their support.

To all the under-privileged people in India.

# Contents

# List of Tables

# List of Figures

# 1 Introduction

## 1.1 Motivation

Since the early 1970s, surface acoustic wave (SAW) based devices have been widely used as delay lines, band-pass filters, and resonators for a variety of applications ranging from consumer needs to military purposes. However, in the last three decades the use of SAWs as a contact-less method to probe the electronic properties of low-dimensional systems, including quantum dots [8], nanowires [9] and two-dimensional electron gases (2DEGs) [10], has attracted a lot of attention. The strong influence of 2DEGs on the propagation of SAWs was first shown by Wixforth *et al.* in 1986, where giant quantum oscillations in the SAW attenuation were observed in GaAs/GaAlAs hetero-structures when the conductivity was quantized [10][11]. Additionally, the electric fields associated with the SAWs can also trap and transport charge carriers along the wave, giving rise to an acoustoelectric current. This phenomenon has been seen as a reliable means of transporting and controlling charge carriers, which can be instrumental in the fields of metrology and quantum information processing. To make use of this property many hybrid systems, involving SAWs and low-dimensional materials, have been intensively investigated. GaAs/GaAlAs hetero-structures have been the most preferred hybrid system for this study, where Talyanski *et al.* observed single electron transport along a one-dimensional (1-D) channel defined using split gates [3]. Similar hetero-structures were used by Rocke *et al.* to dissociate optically generated excitons and transport them with the SAWs to be recombined at a distant quantum dot (0-D), which effectively is light storage in a quantum well [12]. Acoustoelectric effects have also been studied in single walled carbon nanotubes (1-D), where

electron heating [13], phase-coherence breaking [13] and adiabatic charge pumping [14] has been observed. Apart from those in GaAs though, acoustoelectric current in other 2-D materials have been relatively unexplored.

Graphene [15], a flat mono-layer of $sp^2$ hybridised carbon atoms in a hexagonal lattice, has been the subject of considerable interest since its discovery in 2004. It has undeniably revolutionised materials research owing to its incredible electronic [5] and mechanical properties [16][17]. The electrical attributes of graphene include: ballistic transport with mobilities as high as 200,000 $cm^2V^{-1}s^{-1}$ [18]; ambi polar carriers; zero band gap of semiconductor; and Dirac behaviour of fermions [5]. A substantial amount of interest in graphene though, is due to the possibility of realising a wide range of commercial devices including but not limited to flexible electronics, chemical and bio-sensors, and ultra-capacitors. The large-area growth of graphene on transition metals such as copper, via. chemical vapour deposition (CVD) [19] is a promising step towards this goal. This cost-effective and high-yield method produces graphene of consistent quality, which is preferred over exfoliated graphene for device applications [20].

With its unique properties, graphene naturally lends itself to potential integration with SAWs. Yet surprisingly, the possibilities in this area are relatively untapped. So far, the little work reported in this area includes theoretical studies of the coupling of electrons in graphene with SAW observables by Thalmeier *et al.* [21] and Zhang *et al.* [22], and the use of graphene-like nano-sheets for gas sensing application in SAW devices [23]. Miseikis *et al.* demonstrated the acoustoelectric current in graphene for the first time in 2012 [24], but if this technology is ever to be commercialised there remains a significant need to study the acoustoelectric current in graphene as a function of SAW variables and temperature. This forms the basis of the research conducted in this work. The devices were studied from eventual applications point of view, therefore large devices (an order of magnitude bigger than previously been reported) were fabricated and investigated under different conditions.

## 1.2 Overview

The results presented in this thesis are among the first in the study of acoustoelectric current in graphene, where all the SAW variables including the SAW intensity, frequency and temperature dependence is considered. Large-area graphene-SAW devices are investigated at different temperature, pressure and gate bias as a function of SAW variables (intensity and frequency). Devices with potential applications in gas sensing and phase shifting have been demonstrated in this work, which is structured in the following manner:

An introduction to SAWs with a historical overview and some of its properties are discussed in Chapter 2, which includes the generation and propagation of SAWs in a piezoelectric medium, and the determination of center frequency of the SAWs generated by single and double electrode inter-digital transducers. This is followed by a discussion on the origin of acoustoelectric current and its occurrence in semiconductors and two-dimensional electron gases. The applications of SAW devices with special emphasis on the devices integrated with the two-dimensional electron gases are discussed here.

Chapter 3 gives an introduction to graphene and discusses some of its relevant properties useful in the explanation of the results presented in this work, which includes the electric field effect, mobility of CVD graphene, and temperature dependence of its conductivity. Graphene preparation techniques with special emphasis on chemical vapour deposition method and its applications are discussed, which is followed by different methods of its characterisation.

Chapter 4 discusses the experimental methodology involved in the fabrication and measurement of the devices discussed in this work. The devices were fabricated in a clean-room environment using conventional electron-beam lithography techniques, which is discussed along with the processes involved in the transfer of CVD graphene to different substrates. The processes involving the characterisation of graphene and identification of the sources of impurities, fabrication of metal contacts, and the mounting of devices on a custom designed printed circuit board for electrical measurements, are also discussed. This is fol-

lowed by the description of the experimental set up used for the electrical measurements and the experiments conducted on bare lithium niobate which is used as a control for other graphene-SAW devices.

Chapter 5 investigates the acoustoelectric current in graphene as a function of SAW intensity and frequency at room temperature. Macroscopic acoustoelectric current is observed at length scales more than an order of magnitude larger than previously been reported [24], demonstrating the feasibility of large scale graphene-SAW devices for various applications such as gas and chemical sensors. The observations are explained by using a relatively simple classical relaxation model, which describes the interaction of carriers in graphene with SAWs. The mobility obtained from these observations are reported for the first time in graphene/lithium niobate hybrid systems. A modified version of this chapter is published in *Applied Physics Letters*, **103**, 133101 (2013).

In chapter 6, the acoustoelectric current is investigated as a function of temperature, SAW intensity and frequency. It was observed that the SAWs of different wavelengths probe the conductivity of graphene at different length scales. The simple classical relaxation model is found to be valid for high frequency SAWs throughout the temperature range studied (50-300 K), whereas for low frequency SAWs a non-monotonous change in acoustoelectric current is observed. The temperature dependence of the conductivity of graphene owing to the impurities, charge puddles, *etc.* in determining the direction of acoustoelectric current is discussed. An adapted form of this chapter is published in *Applied Physics Letters*, **105**, 263106 (2015).

In chapter 7, the devices with a top-gate configuration were investigated to study the electric field-effect of graphene on lithium niobate. The resistance modulation in graphene is achieved by applying a small gate voltage, and the corresponding effect on the SAW variables is measured. The acoustoelectric current measured as a function of gate voltage and SAW intensity at different SAW frequencies demonstrates the absence of acoustoelectric current at the charge neutrality point. In addition, voltage-controlled amplitude and phase (velocity) shifter devices are demonstrated for the first time in graphene/lithium

niobate hybrid systems, which work at much smaller voltages as compared to other phase shifters on lithium niobate.

Chapter 8 gives a brief summary of all the results presented in this work along with some suggestions for future research.

# 2 Surface Acoustic Waves

## 2.1 Overview

Surface acoustic waves (SAWs) are a kind of mechanical wave that travel along the surface of a medium, with their amplitude decaying exponentially away from the surface (see Figure 2.1). Their existence was first demonstrated by Lord Rayleigh in 1885 while investigating the behaviour of waves on the plane of homogeneous isotropic elastic solids [25]. These surface waves, also known as Rayleigh waves, in combination with the shear surface waves (Love waves) and bulk waves were used to detect cracks in the solid medium. In the mid 1940s after the end of World War II, the developments needed in radar technology brought the interest in SAWs towards electronic applications. The improvements in range capability of a radar required a delay line, such that the received signals can be delayed by different amounts to have a coherent output. The received signals are in the form of electromagnetic waves, hence the use of SAWs, which travels 100 times slower than them, came as a natural solution for introducing such delay. This resulted in the development of transducers that could generate high frequency waves along the surface of a medium. The first inter-digital transducers (IDTs) were reported by White and Voltmer in 1965, where they used thin cadmium sulfide (CdS) films on quartz for surface wave generation [26]. IDTs are thin metallic electrodes on the surface of a piezoelectric material like lithium niobate or quartz and could be easily fabricated using photo-lithography, which proved to be a very convenient and low-cost method for the generation and detection of SAWs. In the subsequent years, there were rapid developments in the understanding of SAWs and a huge range of devices emerged [27]. For example, apodised IDTs were used in bandpass

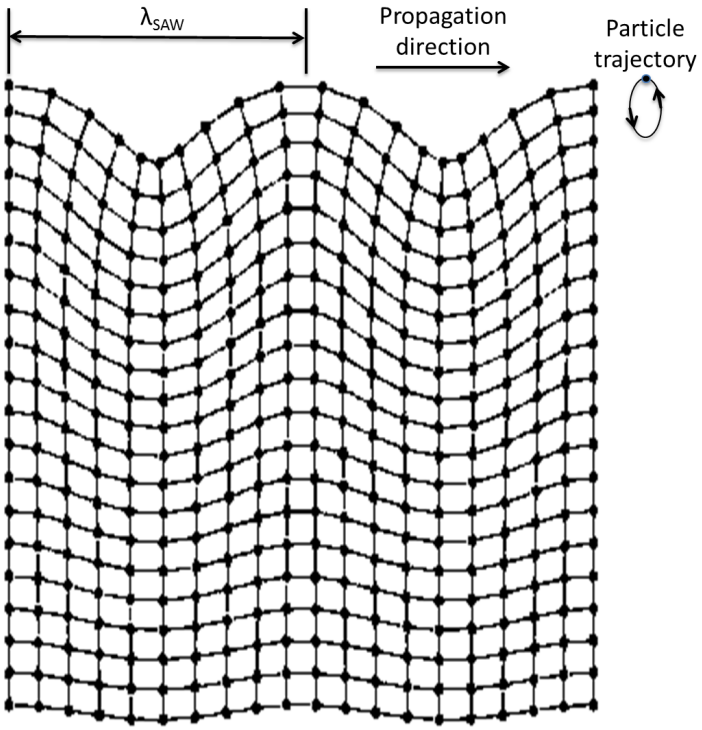


**Figure 2.1** The instantaneous displacement of each particle during SAW propagation in an isotropic medium.

filtering that can generate any desired frequency response [28]; microwave acoustic circuit components such as gratings, resonators, and oscillators based on SAW devices [29], and many more. Today, SAW devices are used widely in applications ranging from radar systems to consumer electronics including televisions and mobile phones. In this chapter we will discuss: the fundamental theory of SAWs, and different piezoelectric materials used in the fabrication of SAW devices in section 2.2; acoustoelectric phenomenon in semiconductors and two-dimensional electron system (2DES) in section 2.3; and some applications of the SAW-based electronic devices in section 2.4.

## 2.2 Equations of Motion

In an elastic medium, when atoms are subjected to strain, the displacement of atoms is countered by a restoring internal force that tries to bring the atom back to its equilibrium position. This creates a stress in the medium causing further strain at distant points,

which in turn creates stress again. This eventually results in the propagation of strain in the medium. SAWs propagate by causing such longitudinal and vertical strains in the medium. To understand the motion for SAWs, let us first consider a particle in the isotropic medium in an equilibrium state located at $\mathbf{x} = (x_1, x_2, x_3)$ displaced by an amount $\mathbf{u} = (u_1, u_2, u_3)$, where $u_1, u_2$ and $u_3$ are functions of $x_1, x_2$ and $x_3$ respectively. The resultant strain generated in the isotropic medium is defined as

$$S_{ij}(x_1, x_2, x_3) = \frac{1}{2}\left(\frac{\partial u_i}{\partial x_j} + \frac{\partial u_j}{\partial x_i}\right) \qquad i, j = 1, 2, 3 \tag{2.1}$$

Assuming that the resulting stress ($T_{ij}$) is proportional to the strain given by Equation (2.1), we have

$$T_{ij} = \sum_k \sum_l c_{ijkl} S_{kl} \qquad i, j, k, l = 1, 2, 3 \tag{2.2}$$

where $c_{ijkl}$ is the stiffness tensor. In this isotropic medium, consider an elementary cube of length $\delta$ at $\mathbf{x} = (x_1, x_2, x_3)$ under a stress given by Equation (2.2) then the resultant force acting on this cube along the x-direction would be

$$F_1 = \delta^2(T_{i1}(x_1 + \delta/2, x_2, x_3) - T_{i1}(x_1 - \delta/2, x_2, x_3)) \tag{2.3}$$

The total force in the y and z direction can be calculated similarly, and the combined form can be expressed as

$$F_i = \delta^3 \left(\sum_j \frac{\partial T_{ij}}{\partial x_j}\right) \qquad i, j = 1, 2, 3 \tag{2.4}$$

From Newton's law of motion, for a material of density $\rho$ Equation (2.4) must be equal to

$$\rho \frac{\partial^2 u_i}{\partial t^2} = \sum_j \frac{\partial T_{ij}}{\partial x_{ij}} \qquad i, j = 1, 2, 3 \tag{2.5}$$

Now, to understand the case of anisotropic materials, let us consider a homogenous piezoelectric insulator. In many piezoelectric materials, the elastic stress and strain are strongly coupled with the electric field and displacement. For such cases, the stress tensor given by Equation (2.2) needs to be modified to incorporate the stress induced by the electric

field **E**, therefore

$$T_{ij} = \sum_k \sum_l c^E_{ijkl} S_{kl} - \sum_k e_{kij} E_k \qquad i,j,k,l = 1,2,3 \tag{2.6}$$

where $c^E_{ijkl}$ is the stiffness tensor in the presence of an electric field **E**. Similarly the electric displacement **D** is also affected by the strain factor and is given by

$$\mathbf{D}_i = \sum_j \epsilon^S_{ij} E_j + \sum_j \sum_k e_{ijk} S_{jk} \qquad i,j,k = 1,2,3 \tag{2.7}$$

where $\epsilon^S_{ij}$ is the permittivity tensor at constant strain and $e_{ijk}$ is the piezoelectric tensor that relates elastic to electric fields. Please note that the derivation of the relations in Equations (2.6) and (2.7) is beyond the scope of this work, but is available in the literature [30].

The substitution of $E_i = -\partial\phi/\partial x_i$, where $\phi$ is the electric potential, into Equation (2.6) reduces the equation of motion to

$$\rho \frac{\partial^2 u_i}{\partial t^2} = \sum_j \sum_k \left( e_{kij} \frac{\partial^2 \phi}{\partial x_j \partial x_k} + \sum_l c^E_{ijkl} \frac{\partial^2 u_k}{\partial x_j \partial x_l} \right) \tag{2.8}$$

As the piezoelectric material considered here is an insulator, the conservation of charge reduces Equation (2.7) to

$$\sum_i \sum_j \left( \epsilon^S_{ij} \frac{\partial^2 \phi}{\partial x_i \partial x_j} + \sum_k e_{ijk} \frac{\partial^2 u_j}{\partial x_i \partial x_k} \right) = 0 \tag{2.9}$$

The schematic of the chosen axis and the wavefronts of the surface-wave solution is shown in Figure 2.2. The wave propagates in the $x_1$ direction and the wavefronts are perpendicular to it. The plane formed by the surface normal $x_3$ and the propagation direction $x_1$ is called the sagittal plane. In case of surface-waves, the motion is restricted to this plane only. In an infinite medium a plane wave of the following form can be substituted

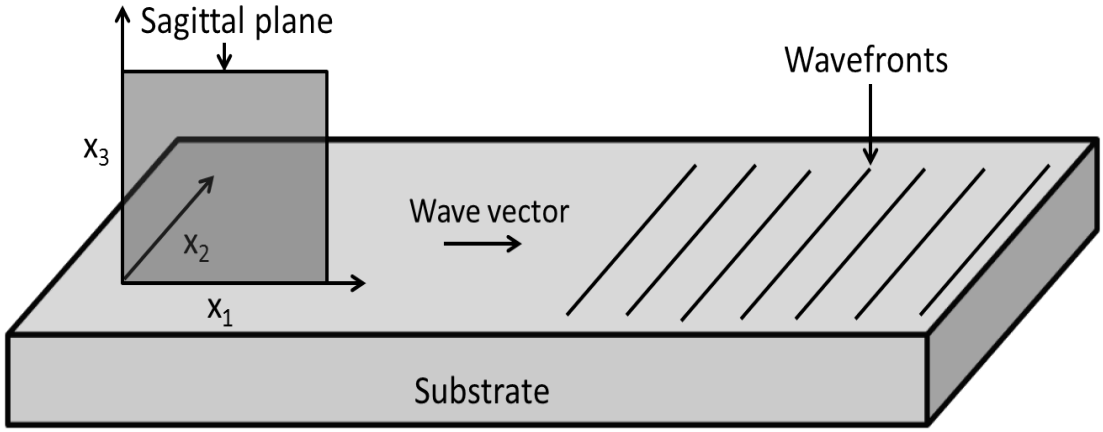


**Figure 2.2** A schematic of the substrate showing the sagittal plane, wave propagation direction, and wavefronts.

for **u** and $\phi$ to find a solution to Equations (2.8) and (2.9)

$$\mathbf{u} = u_0 \exp(j(\omega t - \mathbf{k}.\mathbf{x})) \tag{2.10}$$

$$\phi = \phi_0 \exp(j(\omega t - \mathbf{k}.\mathbf{x})) \tag{2.11}$$

where $u_0$, $\phi_0$ are constants, $\omega$ is the wave frequency and $\mathbf{k} = (k_1, k_2, k_3)$ is a wave vector that defines the direction of wave propagation.

With appropriate boundary conditions, four solutions in four variables including $u_i$, where (i=1,2,3), and $\phi_0$ can be obtained. One way of finding the solutions is to set the determinant of the coefficients of Equations (2.8) and (2.9) to be equal to zero. This gives four solutions with different **k** values. One of these solutions correspond to the electrostatic solution of an isotropic medium while the other three are non-dispersive acoustic waves. Now, to obtain the solutions for a piezoelectric half-space (*i.e.* at the surface of a piezoelectric medium) we have to apply appropriate boundary conditions. Let us consider the free-surface case where the surface above the piezoelectric material is vacuum. The first boundary condition is that the net force acting on the surface must be equal to zero *i.e.*

$$T_{13} = T_{23} = T_{33} = 0 \qquad at \quad x_3 = 0 \tag{2.12}$$

Secondly, $D_3$ is expected to be continuous at the interface of the piezoelectric and the vacuum. Since there are no free charges, we must have

$$D_3 = \epsilon_0 \left|\beta\right| \phi \qquad\qquad at \quad x_3 = 0 \tag{2.13}$$

where $\epsilon_0$ is the permittivity of free space, $\beta$ is the wavenumber, and $\phi$ is the potential in vacuum, which can be written as

$$\phi = f(x_3) \exp(j\omega t - \beta x_1) \tag{2.14}$$

Now, since the space above the piezoelectric surface is empty, the potential should satisfy Laplace's equation, *i.e.* $\nabla^2 \phi = 0$, and vanish at $x_3 = \infty$. Given these conditions, the potential $\phi$ for $x \geq 0$ is expected to be of the following form:

$$\phi = \phi_0 \exp(-\left|\beta\right| x_3) \exp(j\omega t - \beta x_1) \tag{2.15}$$

In case of a metallised surface, in addition to the condition mentioned in Equation (2.12), the necessary boundary condition is that the potential at the surface is zero *i.e.* $\phi = 0$ at $x_3 = 0$.

To find the solution for surface waves, we have to consider the partial waves that satisfies the equation of motion for an infinite material given by Equations (2.8) and (2.9). These partial waves can be written as

$$\mathbf{u}' = {u_0}' \exp(j\gamma x_3) \exp(j(\omega t - \beta x_1)) \tag{2.16}$$

$$\phi' = {\phi_0}' \exp(j\gamma x_3) \exp(j(\omega t - \beta x_1)) \tag{2.17}$$

where $\beta$ is assumed to be real, and $\gamma$ is a function of $v_R/v_T$ that is always positive ($v_R$, and $v_T$ are the respective velocities of the Rayleigh and transverse wave). For a particular value of $\beta$, Equations (2.16) and (2.17) can be substituted in Equations (2.8) and (2.9) to find four quadratic equations for $\gamma$. This gives eight complex solutions for $\gamma$, but only the solutions with negative imaginary parts are allowed as it requires $\mathbf{u}'$ and $\phi'$ to vanish at

$x_3 = -\infty$. In general, four out of these eight solutions satisfy this condition. The partial waves corresponding to these values of $\gamma_m$ ($m$=1,2,3,4) can be written as

$$\mathbf{u}_m^{'} = u_0^{'} \exp(j\gamma_m x_3) \exp(j(\omega t - \beta x_1)), \tag{2.18a}$$

$$\phi_m^{'} = \phi_0^{'} \exp(j\gamma_m x_3) \exp(j(\omega t - \beta x_1)). \tag{2.18b}$$

The final solution of the equation of motion is assumed to be a linear combination of these partial waves given by

$$\mathbf{u} = \sum_{m=1}^{4} A_m \mathbf{u}_m^{'}, \tag{2.19a}$$

$$\phi = \sum_{m=1}^{4} A_m \phi_m^{'}, \tag{2.19b}$$

where the coefficients $A_m$ are such that the solutions satisfy the boundary conditions mentioned in Equations (2.12) and (2.13). This gives the value of the determinant of the coefficients in Equations (2.8) and (2.9), which must be equal to zero for a valid solution. This determinant value would reduce to zero for an appropriate choice of $\beta$. The whole procedure is iterated several times for different values of $\beta$ until the determinant reduces to zero. The solutions obtained here are strongly dependent on the anisotropy and the orientation of the material that makes it extremely difficult to generalise the surface-wave characteristics for different materials. The most frequently found surface-wave solution has its displacement almost parallel to the sagittal plane and is called the Rayleigh wave. In case of a piezoelectric material like Y-Z lithium niobate, it also has a corresponding electric field and is called the piezoelectric Rayleigh wave. For Y-Z lithium niobate, this solution is well known, the variation of the displacement and potential of this piezoelectric Rayleigh wave as a function of depth in the substrate is shown in Figure 2.3(a). It should be noted that the half space above the material is vacuum and by definition the material occupy the space from the surface down. The displacement is allowed only in the sagittal plane, therefore only $u_1$ and $u_3$ are plotted in the figure. The difference between the potential of a free-surface and a metallised one is illustrated in Figure 2.3(b). In case of a free surface, the half-space above the material is vacuum, therefore the potential decays as

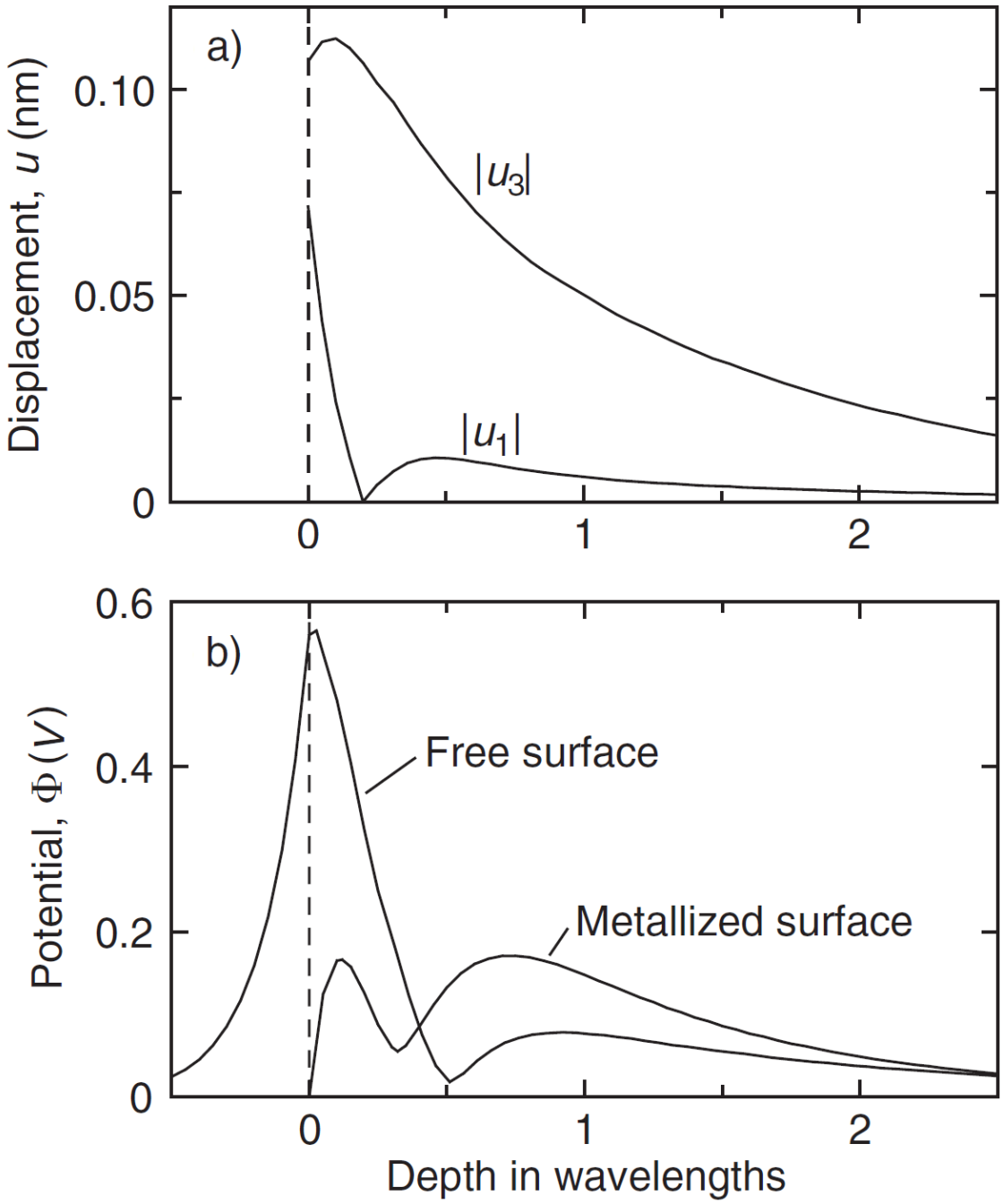


**Figure 2.3** Displacement and potential obtained from the equation of motions in Eqs. (2.19a) and (2.19b) are plotted as a function of depth below the surface. a) Displacement for free-surface case b) Potential for free- and metallised-surface. Displacement for the metallised case is identical to the free-surface (illustration taken from [1]).

we go away from the surface. The surface-wave characteristics determined by this solution reveals some important information about the material which is essential in determining its suitability as a substrate.

### 2.2.1 Piezoelectric Materials

The applications of the SAW devices are strongly dependent on the properties of the substrate. Many factors, including the availability of the substrate, ease of lithographic process, SAW velocity, coupling constant, temperature coefficient of delay (TCD) (depends on the rate of change of time delay as a function of temperature), coupling with the bulk waves, *etc.* needs to be examined before selecting the substrate. Different piezoelectric materials of II-VI and III-V type semiconductors have been studied for SAW device applications [31] such as designing frequency control systems and high-frequency signal processing devices. In piezoelectric materials, the elasticity is coupled with the electric fields that help the transduction process by converting the electric field into acoustic waves and vice versa. The velocity and TCD are the two most important characteristics used to determine the properties of the substrate for different applications. For example, when the surface of the piezoelectric substrate is shorted by thin metal films, the velocity changes from $v_f$ (free surface velocity) to $v_m$ (metallised surface velocity). This change in velocity can be used to determine the extent of piezoelectric coupling. The coupling constant $K^2$ is defined as

$$\frac{K^2}{2} \equiv \frac{v_f - v_m}{v_f} = \frac{\Delta v}{v_f}. \tag{2.20}$$

Also, if we have two transducers, a source and a receiver, separated by a distance $l$ the delay $T$ can be calculated as $T = l/v_f$. The distance $l$ varies as a function of temperature due to the thermal expansion of the material, which affects the delay $T$. This change in time delay as a function of temperature can be used to define a temperature coefficient of delay $\alpha_T$ for a material, which is given by

$$\alpha_T \equiv \frac{1}{T}\frac{\mathrm{d}T}{\mathrm{d}\Theta} = \frac{1}{l}\frac{\mathrm{d}l}{\mathrm{d}\Theta} - \frac{1}{v_f}\frac{\mathrm{d}v_f}{\mathrm{d}\Theta}, \tag{2.21}$$

where $\Theta$ is temperature. Materials with large TCD generally have a strong coupling constants.

#### 2.2.1.1 Quartz

A quartz substrate was used in the fabrication of the first prototype of a SAW device [26]. Its weak piezoelectric coupling and good temperature stability makes it an excellent substrate for devices such as narrow band-pass filters, oscillators, pulse compressors and resonators. Due to the anisotropy of the material, the orientation plays an important role in determining its properties (see Figure 2.4). For example, the $\psi$=42.5° rotated Y-cut, also known as ST-cut, quartz with propagation along the X-axis (ST-X), was found to have comparatively higher material efficiency; parallel power flux and velocity; and a low TCD that is weakly dependent on the propagation direction [32]. The free velocity ($v_f$) measured in ST-X quartz substrate is 3159 $ms^{-1}$. These substrates can be used to study gas loading effect in graphene-quartz SAW devices [33].

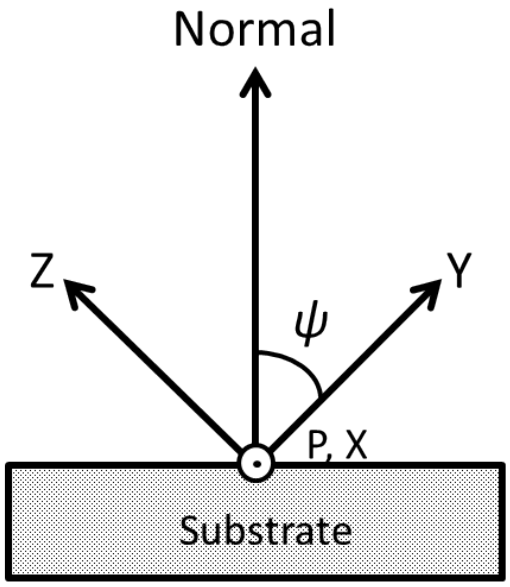


**Figure 2.4** Schematic of a Y-cut substrate with the propagation direction P and X axis, coming out of the plane. The Y-axis is rotated by an angle $\psi$ from the normal.

#### 2.2.1.2 Lithium niobate

Lithium niobate has relatively strong coupling but poor temperature stability. The commonly used YZ-cut lithium niobate, with propagation along the Z-direction has several advantages; for example, strong coupling value (2.4%) as compared to ST-X quartz (0.06%), and the absence of beam steering, which helps in the minimisation of the diffraction of SAWs [34]. However the disadvantage of YZ-cut lithium niobate is the unwanted coupling with bulk waves along with the low TCD ($\alpha_T$=9.4×10$^{-5}$ °C$^{-1}$). For minimum bulk wave generation 128° YX lithium niobate can be used instead of YZ-cut as it has a similar coupling value (2.7%) but there is relatively more diffraction of SAWs. This diffraction is similar to the diffraction of light in the manner that it does not diffract much in the near-field region (near the source transducer) but in the far-field (away from the transducer) the diffraction becomes significant. This is due to the fact that the velocity of the SAW is strongly orientation dependent and the diffracted beam travels on a different axis with a different speed, hence the difference becomes apparent in the far-field region. The free wave velocity ($v_f$) measured in 128° YX- and YZ-cut lithium niobate is 3979 ms$^{-1}$ and 3488 ms$^{-1}$ respectively. These substrates are commonly used in making wide band-pass filters. The work presented in this thesis solely includes the devices fabricated on these substrates.

### 2.2.2 SAW Generation

SAWs of various shapes can be generated using transducers of different types on a piezoelectric substrate. To understand the basic transducer response, let us consider two uniform single-electrode transducers with a pitch length $p$ and transducer width $W$ (as shown in Figure 2.5). Each transducer has $M$ electrodes centered at $x_1, x_2, \ldots, x_M$ respectively. When a voltage $V$ is applied across the source, it generates a periodic electric field and a corresponding elastic stress in the medium, resulting in a SAW in both the directions perpendicular to the transducer. Here, we consider only the SAW going towards the receiver. The transducers are assumed to be non-reflective and composed of identical electrodes.

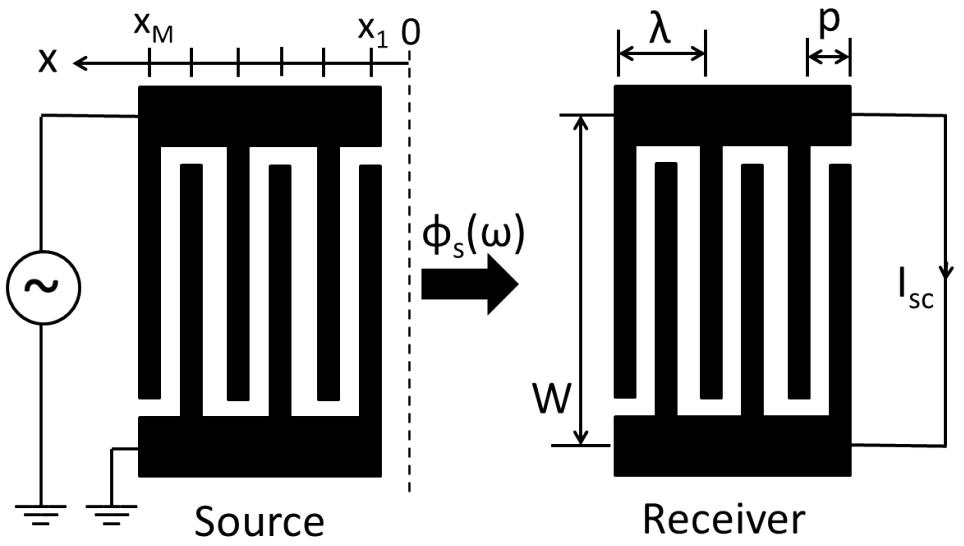


**Figure 2.5** The schematic of a source and receiver transducer used in the generation of SAWs.

Each active electrode (connected to positive voltage supply) acts as a source for generating SAWs that travel with phase velocity $\nu$ and frequency $\omega$. The electrodes connected to the lower bar (inactive electrodes) of the transducers are grounded, so they do not generate any SAW. The amplitude of the wave generated by the electrode at $x_m$ has the form $\exp(jk(x - x_m))$ where $k$ is the wavenumber. Thus, the wave generated by electrode $m$ is given by

$$\phi_m(x, \omega) = \hat{P}_m V E(\omega) \exp(jk(x - x_m)) \tag{2.22}$$

where $E(\omega)$ corresponds to the electrode response and $\hat{P}_m = 0, 1$ for m = even, odd respectively. All electrodes are assumed to be identical, therefore $E(\omega)$ is independent of m. The sequence of $\hat{P}_m$ for a single and double-electrode transducer (see Figure 2.6) can be given by

$$\hat{P}_m = \begin{cases} 1, 0, 1, 0, 1, 0, 1, 0, \ldots & \text{for single-electrode} \\ 1, 1, 0, 0, 1, 1, 0, 0, \ldots & \text{for double-electrode} \end{cases} \tag{2.23}$$

The total wave amplitude $\phi_T(\omega)$ generated by the source can be calculated as the sum of

all the SAWs generated by its electrodes *i.e.* the amplitude at x=0 can be given by

$$\phi_T(\omega) = \sum_{m=1}^{M} \phi_m(0,\omega) = VE(\omega) \sum_{m=1}^{M} \hat{P}_m \exp(jk(-x_m)) \tag{2.24}$$

where $M$ represents the total number of electrodes. An array factor $A(\omega)$ can be defined for convenience to calculate the frequency of the generated SAW as

$$A(\omega) = \sum_{m=1}^{M} \hat{P}_m \exp(jk(-x_m)) \tag{2.25}$$

such that the transducer response can be given by

$$\phi_T(\omega)/V = E(\omega)A(\omega) \tag{2.26}$$

For a single-electrode transducer, Equation (2.25) can be simplified using Equation (2.23) with pitch length $p$ such that the electrode $m$ is at $x_m = mp$. Hence, it can be reduced to a sum of $N = M/2$ terms given by

$$A(\omega) = \sum_{m=1}^{N} \exp(-2jkmp) = \frac{\sin Nkp}{\sin kp} \exp(-j(Np+1)kp) \tag{2.27}$$

Equation (2.27) gives the solution at $kp = n\pi$ *i.e.* at $p = n\lambda/2$ where $\lambda$ is the wavelength of the SAW. The fundamental frequency correspond to the $n = 1$ value when $\lambda = 2p$, whereas the solutions for $n > 1$ are its harmonics. The array factor calculated for the single- and double-electrode transducers is plotted as a function of wavenumber $k$ in Figure 2.6, where the peaks correspond to the solutions obtained at n=0, 1, 2, and so on. The first peak observed at k=0 gives the null solution, whereas the peaks thereafter are observed at the wavenumbers corresponding to the fundamental frequency and its higher harmonics respectively. The only difference between the single- and double-electrode transducer response is that the center or fundamental frequency observed in double-electrode transducers occurs at the wavenumber, which corresponds to the first harmonics in case of single-electrode transducer. The higher harmonics in double-electrode transducer are an integer multiple of this fundamental frequency (see Figure 2.6(a)), which is similar to

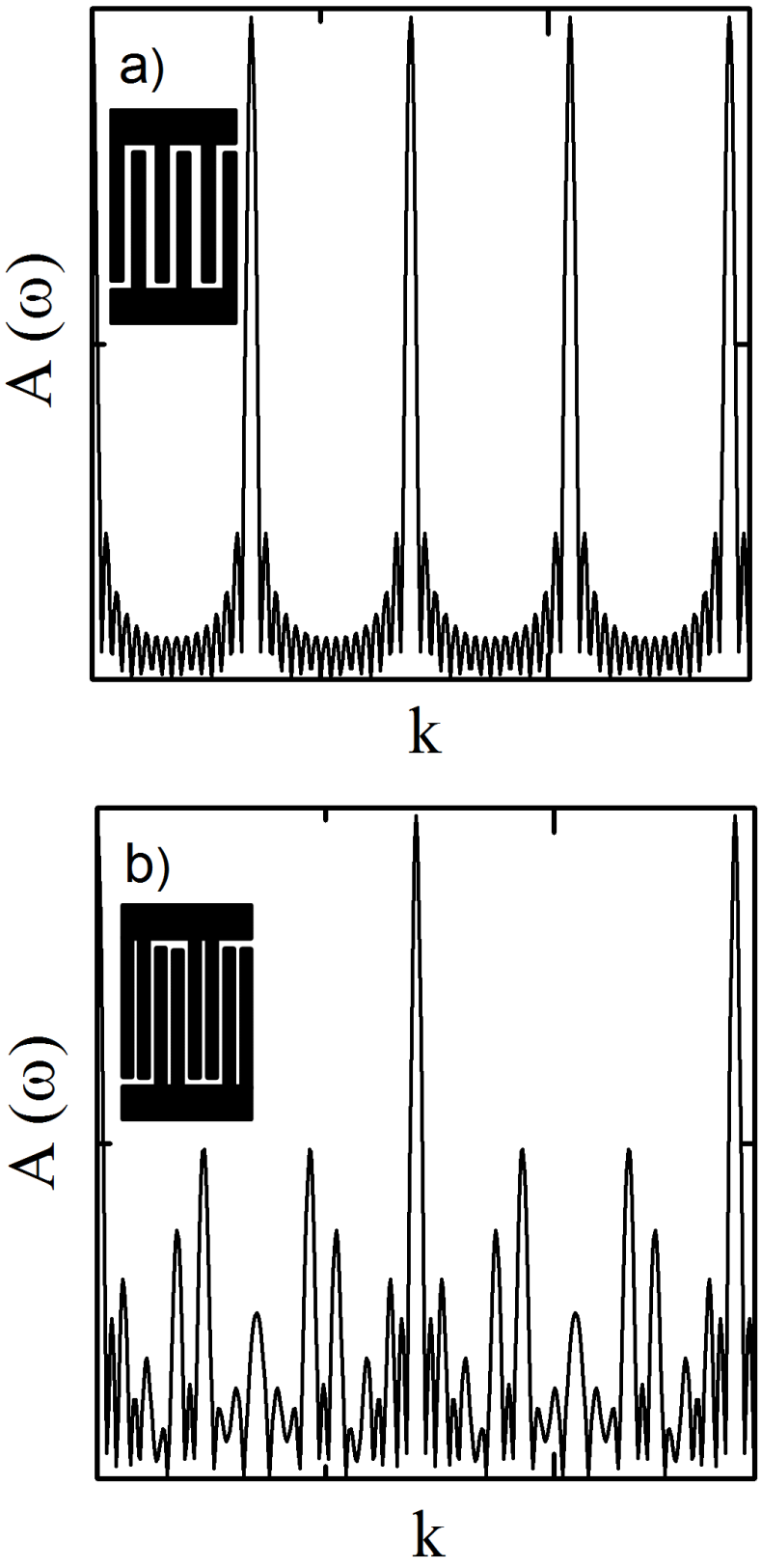


**Figure 2.6** The transducer response, in the form of array factor A($\omega$), is plotted as a function of the wavenumber k (in arbitrary units) a) Double-electrode b) Single-electrode.

the single-electrode transducer response at the odd multiples of its center frequency (see Figure 2.6(b)).

## 2.3 Acoustoelectric Phenomenon

When SAWs interact with charge carriers in the traveling medium two important effects can be observed. Firstly, the charge carriers could change the amplitude and velocity of the wave, and secondly, the SAWs could trap the charge carriers in their potential mimima and generate a current along the direction of wave propagation. This second class of effect, known as the acoustoelectric effect, was predicted by Parmenter [35] in 1953. He suggested that as a longitudinal periodic acoustic wave travels in a medium it gives rise to a periodic electric field that travels with the same speed as the wave. The conduction electrons of the medium can interact with this field and those having a velocity component along the direction of wave propagation and speed comparable to that of the wave, can be trapped by the moving potential minima of the acoustic wave. This gives rise to an acoustoelectric current along the direction of wave propagation. Parmenter argued that it would therefore be possible to measure the acoustoelectric effect in metals and semi-conductors. The numerical calculations followed by Beukel were in partial contradiction with the predictions made by Parmenter. He estimated that the acoustoelectric current generated in metals was too small to measure, where as in semi-conductors, it was $10^3$-$10^4$ times larger than in metals at room temperature [36]. Weinreich also investigated the motion of electrons and holes in a semiconductor in the presence of an acoustic wave [37] and identified the flaws in the arguments made by Beukel and Parmenter. He explained the acoustoelectric effect as a wave-particle interaction mechanism where the momentum transfer from the wave leads to the dragging of particle along the wave. His classical treatment of the wave-particle drag also considers the relaxation time $\tau$ of the carrier distribution. The carriers tend to attain the lowest energy state of the wave, which generally takes a non-zero time to reach equilibrium, therefore the carriers are always lagging behind the wave by a small amount. Weinreich showed that for very low ($\omega\tau \rightarrow 0$) and very high values ($\omega\tau \rightarrow \infty$) of $\omega\tau$, where $\omega$ is the SAW frequency, the net force exerted by the wave

on the charge vanishes, therefore the acoustoelectric effect can only be observed for the intermediate values of $\omega\tau$ where a non-zero force is exerted by the wave on the carriers [38]. In the following, we briefly discuss the analysis of Weinreich to understand the origin of acoustoelectric current [37]. He showed that the acoustoelectric current can be explained using the concept of deformation potential with an assumption that the particle's potential energy $V_I$ is proportional to the dilatation $\Delta$ (deformation of the crystal under stress) *i.e.*

$$V_I = -\epsilon_1 \Delta \tag{2.28}$$

where $\epsilon_1$ is a constant. The force exerted on the particles by the acoustic wave may result in an acoustoelectric current. In general, the net particle current $j$ in a macroscopic system comprises of a drift term and a diffusion term, which can be written as

$$j = D(F/kT - \nabla V_I)n \tag{2.29}$$

where $n$ is the particle density, $F$ is the force applied to the particles, $kT$ is the thermal energy, and $D$ is the diffusion coefficient. To simplify the space charge difficulties arising from the bunching of charges caused due to the force exerted by the SAW, an approximation was made that the SAW wavelength is much greater than the carrier mean free path. With this approximation, the charge neutrality is maintained and the induced electric field can be considered proportional to the deformation potential of the SAW for small sinusoidal disturbances. The potential of a plane wave traveling in a semiconducting medium can be of the form

$$\phi = \phi_0 \exp(ik(x - ct)) \tag{2.30}$$

where $\phi_0$ is a constant, $k$ is the wavevector and $c$ is the velocity of the wave. The interaction energy between the field and particles can be defined as

$$U_I = \sum_i q_i \phi_i \tag{2.31}$$

where $q_i$ is called the acoustic charge. In the presence of a constant electric field, such that the drift velocity of the charge carriers is $\beta c$ in the x-direction, the acoustoelectric

current densities are given by

$$j_n = n\beta c + \frac{nD_n}{kT}\frac{\partial}{\partial x}(q_n\phi + e\gamma_k\phi) - D_n\frac{\partial n}{\partial x} \tag{2.32}$$

$$j_p = \frac{p\beta c}{b} + \frac{pD_n}{bkT}\frac{\partial}{\partial x}(q_p\phi - e\gamma_k\phi) - \frac{D_n}{b}\frac{\partial n}{\partial x} \tag{2.33}$$

where $n$ and $p$ are the concentration of electrons and holes respectively; $b$ is the ratio of their mobilities; $q_n$, $q_p$ are the respective acoustic charges; $kT$ is the thermal energy; and $\gamma_k\phi$ is the induced electrostatic potential. The equation of continuity takes the form

$$\frac{\partial n}{\partial t} + \frac{\partial j_n}{\partial x} + \frac{1}{\tau}\left[n - n_0\left(1 + \frac{q}{1+s}\frac{\phi}{kT}\right)\right] = 0 \tag{2.34}$$

$$\frac{\partial p}{\partial t} + \frac{\partial j_p}{\partial x} + \frac{1}{\tau}\left[p - p_0\left(1 + \frac{qs}{1+s}\frac{\phi}{kT}\right)\right] = 0 \tag{2.35}$$

where $s \equiv n_0/p_0$ is the ratio of equilibrium concentration of electrons and holes, $\tau$ is the lifetime, and $q = q_n + q_p$. The last term in Equations (2.34) and (2.35) refers to the first order change in the concentration of carriers under the influence of field $\phi$. If we assume $n - n_0 << n_0$ and $p - p_0 << p_0$, then $n$ and $p$ can be expressed as

$$n = n_0 + n_1\exp(ik(x - ct)) \tag{2.36}$$

$$p = p_0 + p_1\exp(ik(x - ct)) \tag{2.37}$$

The expressions for $n_1$ and $p_1$ can be obtained by substituting these values of $n$ and $p$ into Equations (2.34) and (2.35). From the charge neutrality condition, we have

$$n_1 = p_1 = \frac{n_0}{1+s}\frac{q\phi_0}{kT}M \tag{2.38}$$

where

$M \equiv \frac{1+\omega_0(1+sb)/\omega^2\tau(1+s)}{1+\omega_0(1+sb)/\omega^2\tau(1+s)-i(\beta_0-\beta)(1-s)\omega_0/(1+s)\omega}$,

$\omega \equiv kc$,

$\omega \equiv c^2/D_n$,

and $\beta_0 = (1+sb)/(1-s)$.

The factor $M$ accounts for the bunching of carriers based on the frequency, applied field and the type of material (n- or p-type). This solution can be used to compute the time-average value of the dc particle current described by Equation (2.32) and (2.33). The net acoustoelectric current can be calculated as

$$I_{ae} = -e(\bar{j_n} - \bar{j_p}) \tag{2.39}$$

Since, only the first order change in carrier concentration is taken into account, Equation (2.39) is not adequate for the second order calculations. However, Weinreich argued that if $\tau$ is assumed to be very large, then the whole recombination term would be negligible. Thus, the final acoustoelectric current can be given by

$$I_{ae} = -\frac{1}{2}\frac{en_0c}{(1+s)^2}\left(\frac{q\phi_0}{kT}\right)^2 \frac{(1-s)-\beta(1+s/b)}{1+(\beta_0-\beta)^2\left[(1-s)/(1+s)\right]^2(\omega_0/\omega)^2} \tag{2.40}$$

Weinreich *et al.* [38] qualitatively observed the acoustoelectric effect in n-type germanium and simplified the expression in Equation (2.40) for a transverse wave in quartz traveling along the $\langle 100 \rangle$ direction and polarised in the $\langle 010 \rangle$ direction, for which the acoustoelectric field $E_{ae}$ is given by

$$E_{ae} = -\frac{6\pi^2 q^2 \tau S}{e\lambda^2 kT} \tag{2.41}$$

where $S$ is the acoustic power density, $q$ is the acoustic charge, $\tau$ is the relaxation time and $\lambda$ is the acoustic wavelength. This expression can be further simplified to give the current density $j$ for different systems, as given by

$$j = -\frac{\mu\Gamma F}{v} \tag{2.42}$$

where $\mu$ is the mobility of the charge carriers, $\Gamma$ is the attenuation coefficient, $F$ is the SAW intensity flux, and $v$ is the velocity of the SAW. Equation (2.42) is referred to as the Weinreich relation in this work. This relation formed the basis for further investigation in the acoustoelectric behaviour of various semiconductor superlattices and nanostructures. Here, this relation is used in the study of the behaviour of acoustoelectric current in graphene at room and low temperatures. In the following section, we review

the acoustoelectric current measured in semiconductor hetero-structures, one-dimensional (1-D) channels, quantum dots and two-dimensional electron gases (2DEGs).

### 2.3.1 Acoustoelectric Current in Semiconductors

In many piezoelectric semiconductors, it was observed that beyond a certain threshold of applied voltage, the current begins to saturate [39]. Ozaki and Mikoshiba investigated this effect in cadmium sulfide (CdS) at room temperature [40] and proposed a non-linear theory to quantitatively explain the current-voltage characteristics, decay time of current from Ohmic to saturation value, and the characteristics of the acoustoelectric current in piezoelectric materials. By increasing the applied field in a piezoelectric medium, the drift velocity exceeds the speed of sound and the acoustoelectric field $E_{ae}$ becomes large enough to oppose the applied electric field $E$. When the acoustic flux is large enough to satisfy the condition, $dE_{ae}/dE \geq 1$ for negative differential conductivity, large deviations from Ohmic behaviour were observed in the medium [41]. The acoustoelectric theory was further developed by Tien with the concept of charge bunching in the wave troughs [42]. When the intensity of SAWs is smaller than the thermal energy, the particles are able to move freely in the crystal. However, as the SAW intensity increases, the piezoelectric potential $\phi_{SAW}$ becomes dominant over the thermal energy $kT$ and the charge particles gets trapped in the wave potential (see Figure 2.7). Therefore, the drift velocity of the carriers approaches the SAW velocity, which results in current saturation. This dragging of charges consumes the energy of the SAW which is reflected in its attenuation $\Gamma$ and change in the velocity $\Delta v$ of the SAW. The equations for $\Gamma$ and $\Delta v$ can be obtained from the equations of motion given in Equations (2.8) and (2.9), but the derivation of the same is not in the scope of this work. In a simple classical relaxation model where the diffusion effects can be neglected in the weak-signal limit (negligible modulation of carrier concentration by the SAW), the attenuation and velocity change in a piezoelectric semi-conductor, with homogenous bulk conductivity $\sigma$, are given by

$$\Gamma = K^2 \frac{\pi}{\lambda} \left[ \frac{\omega_c/\omega}{1 + (\omega_c/\omega)^2} \right] \tag{2.43}$$

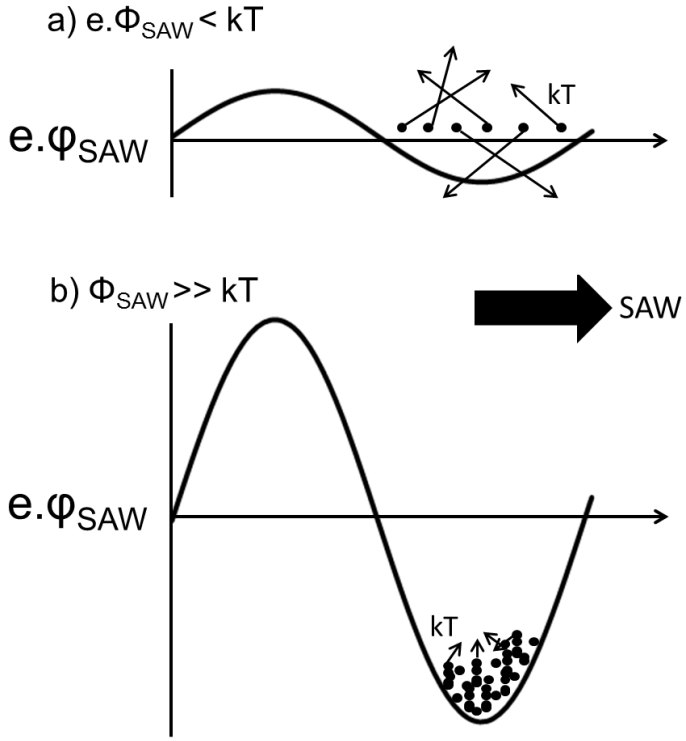


**Figure 2.7** A schematic representation of the bunching of charge carriers, with thermal energy kT, in SAWs of different amplitudes $\phi_{SAW}$. a) e.$\phi_{SAW}$<kT, b) e.$\phi_{SAW}$>>kT

$$\frac{\Delta v}{v} = \frac{K^2}{2}\left[\frac{1}{1+(\omega_c/\omega)^2}\right] \tag{2.44}$$

where $\omega_c = \sigma/(\epsilon_1 + \epsilon_2)$ is the conductivity relaxation frequency, here $\epsilon_1$ and $\epsilon_2$ are the dielectric constants of the piezoelectric substrate and the half space above it respectively [11]. This conductivity relaxation frequency gives the time in which the electron system comes back to its equilibrium state when it is perturbed by an external electric field. When the ultrasonic frequency $\omega$ of the piezoelectric field is much smaller than $\omega_c$, electrons can redistribute itself to screen its effect. As $\omega$ increases, this screening becomes less prominent and eventually for $\omega >> \omega_c$, the piezoelectric field becomes too dominant and the substrate effectively starts behaving like an insulator.

### 2.3.2 Acoustoelectric Current in 2DEGs

The interaction of SAWs with a 2DEG can be observed in a hybrid system of 2DEG over a piezoelectric substrate. The simple classical relaxation model used for semi-conductors is also applicable in this case with an assumption that the 2DEG is in close proximity with the surface of the substrate such that the separation $d$ is much smaller than the wavelength of SAW $\lambda_{SAW}$. For such hybrid systems, the induced acoustoelectric current is assumed to be only in the 2DEG. The conductivity relaxation frequency and the frequency of the piezoelectric field is related to the 2DEG conductivity and the characteristic conductivity of the substrate, as given by

$$\omega_c = \frac{k\sigma_{2D}}{\epsilon_1 + \epsilon_2} \tag{2.45a}$$

$$\omega = \frac{k\sigma_M}{\epsilon_1 + \epsilon_2} \tag{2.45b}$$

It is convenient to express the ratio $\omega_c/\omega$ in Equations (2.43) and (2.44) in terms of $\sigma_{2D}/\sigma_M$, where $\sigma_{2D}$ and $\sigma_M$ are the conductivity of the 2DEG and the substrate, respectively. Hence, the equation for the attenuation $\Gamma$ and velocity $v$ of the SAW can be expressed as

$$\Gamma = K^2 \frac{\pi}{\lambda} \left[ \frac{\sigma_{2D}/\sigma_M}{1 + (\sigma_{2D}/\sigma_M)^2} \right] \tag{2.46}$$

$$\frac{\Delta v}{v} = \frac{K^2}{2} \left[ \frac{1}{1 + (\sigma_{2D}/\sigma_M)^2} \right] \tag{2.47}$$

where $K^2$ is the effective piezoelectric coupling coefficient, and $\lambda$ is the wavelength of SAW. The plot of $\Gamma$/q, where q is the wave vector, and $\Delta v/v$ as a function of $\sigma_{2D}/\sigma_M$ is given in Figure 2.8. When $\sigma_{2D} >> \sigma_M$, the redistribution of carriers can occur rapidly enough to screen the effect of external piezoelectric field, and $\Gamma$ becomes proportional to $\sigma_{2D}$. On the other hand, when $\sigma_{2D} << \sigma_M$ the piezoelectric field itself would be similar to that of an insulator, and $\Gamma$ becomes inversely proportional to $\sigma_{2D}$. Therefore, the maximum attenuation per unit length occurs when $\sigma_{2D} = \sigma_M$ as seen in Figure 2.8(a). When the acoustic wave propagates in a good piezoelectric conductor, the internal electric fields have to vanish, which is similar to its propagation in a non-piezoelectric material

but with reduced velocity compared to a piezoelectric insulator. In addition, the current flowing while the electric field is screened are of short durations, and the Ohmic losses, and therefore the attenuation, associated with them is small. In case of a piezoelectric insulator no such current or Ohmic losses exist. However, at some finite conductivity current flows for the whole time between wave crests to screen the electrostatic electric field of the acoustic wave. In such cases, the Ohmic losses are at a maximum, and the wave velocity is at an intermediate value. This shift in velocity can be seen when $\sigma_{2D}$ changes form insulating to metallic, and a distinct step-like behaviour is observed near $\sigma_{2D} = \sigma_M$, as seen in Figure 2.8(b).

The acoustic behaviour is quantitatively well described by Equations (2.46) and (2.47) in the regime where $\lambda$ is much larger than the intrinsic mean free path $l_{int}$. In this non-ballistic regime ($\lambda >> l_{int}$), the observed acoustoelectric current in the absence of magnetic field can be described by substituting the attenuation coefficient $\Gamma$ form Equation (2.46) in the Weinreich relation given by Equation (2.41). In the presence of a magnetic field and control over induced charge carriers through gate electrode, it is also possible to probe the quantum Hall regime in such hybrid systems [11].

#### 2.3.2.1 Acoustoelectric Current in Graphene

Graphene, a 2-D sheet of carbon atoms arranged in hexagonal lattice, has been widely investigated to explore its electronic, transport, and optoelectronic properties. Due to its large surface area and unique properties, graphene deposited on a piezoelectric substrate like quartz, lithium niobate, and lithium tantalate provides a good system for the integration of 2DEGs with SAWs. Graphene and its properties are discussed in more detail in the following chapter. The probing of large-area graphene using SAWs of different wavelengths could be very useful in determining its electronic properties at different length scales. Theoretical investigations by Thalmeier *et al.* [21] and Zhang *et al.* [22] shows the coupling of SAW observables with the charge carriers in graphene. Large Landau oscillations were predicted in both the attenuation and velocity changes of the SAW traveling

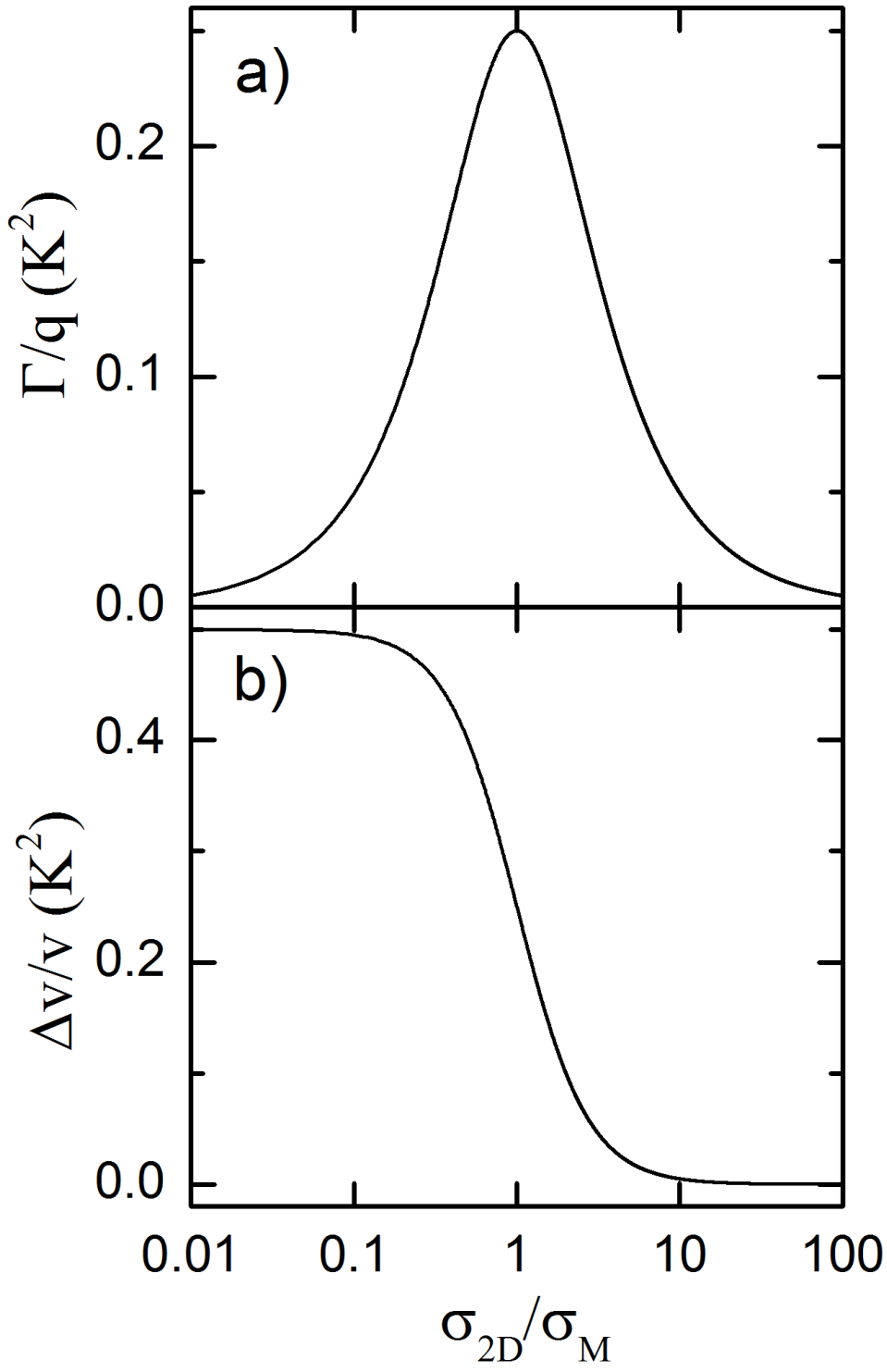


**Figure 2.8** a) Attenuation coefficient Γ per unit wave vector q and b) Fractional change in sound velocity $\Delta v/v$, both in units of $K^2$, plotted as a function of $\sigma_{2D}/\sigma_M$.

in pristine graphene. The selective reactivity of reduced graphene-oxides along with the mass sensitivity of the SAWs has been used to develop hydrogen and carbon monoxide gas sensors [23]. Also, the effect of mass loading of argon and air in graphene-quartz SAW devices has been investigated [33]. However, relatively little work has been done in the study of acoustoelectric current in graphene. Acoustoelectric current in large-area graphene [24] has been reported by Miseikis *et al.* but a comprehensive understanding of its dependence on various SAW parameters, namely wavelength and intensity, has been lacking. In this work, we have addressed this problem and have tried to develop a model for acoustoelectric current as a function of different SAW parameters and at different temperatures.

## 2.4 SAW-based Devices

SAW-based sensors serves a wide variety of applications ranging from day-to-day use in mobile phones and television [43] to sophisticated measurements, such as sensors for detecting temperature [44], mass [45], humidity [46], and in bio-sensing applications like detecting antibodies, enzymes, and proteins [47]. They are commonly used as low and high band-pass filters, resonators, and oscillators in electronics. The recent developments in the use of SAWs for probing low-dimensional systems has also created exciting opportunities in metrology for the quantisation of electric current [3]; storage of light in quantum wells [12] and in quantum computation [48]. Here we briefly review the device applications that relate to the work presented in this thesis.

### 2.4.1 Single Electron/Photon Transport

The interaction of SAWs with the charge carriers can be used to probe the electronic properties of low-dimensional systems. At low temperatures, in the ballistic conductance regime ($qL >> 1$), where $q$ and $L$ are the wavenumber and the length of the low dimensional channel respectively , the interaction of ultrasonic phonons of SAW and electrons in nanostructures (1-D nanowires or 2-D constricted channels) could induce huge oscilla-

tions in acoustoelectric current as a function of gate voltage [49]. This phenomenon was observed in quasi 1-D ballistic channels (quantum point contact), defined by split gates on GaAs/$Ga_{1-x}Al_xAs$ hetero-structures, whose conductance $G$ is given by

$$G = n\frac{2e^2}{h}, \tag{2.48}$$

where $n$ is the number of occupied one-dimensional sub-bands. Contrary to the step like rise in conductance, the acoustoelectric current in the ballistic conductance channel undergoes giant oscillations as a function of gate voltage [2], with the maxima lying between the plateaus of conductance steps (see Figure 2.9).

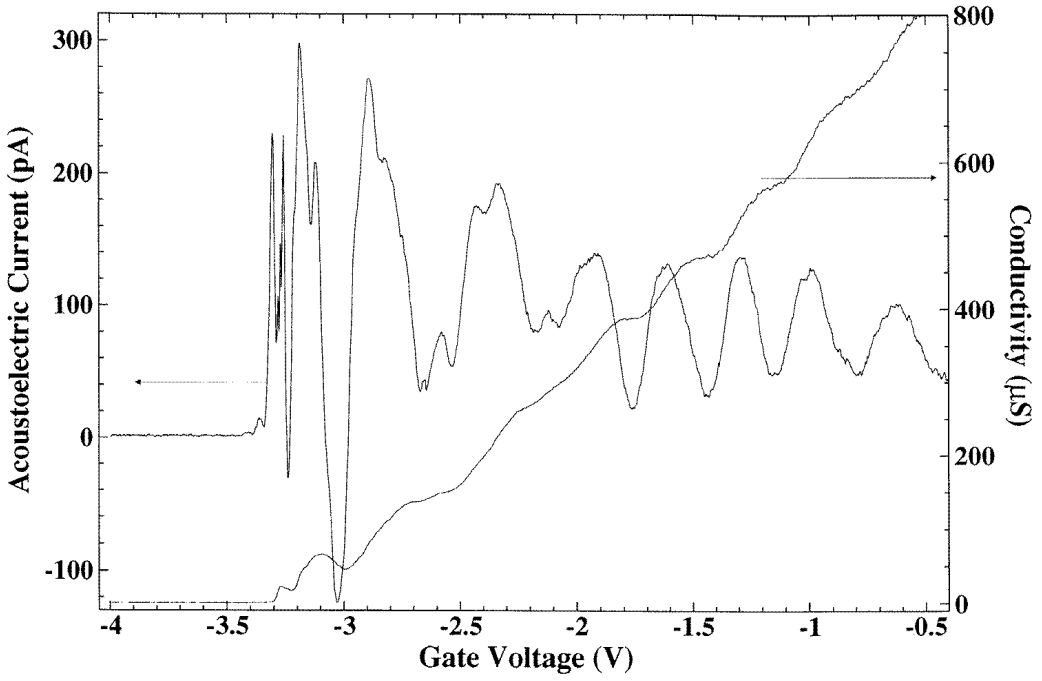


**Figure 2.9** Acoustoelectric current and conductivity plotted as a function of gate voltage for GaAs/$Ga_{1-x}Al_xAs$ hetero-structures (illustration taken from [2]).

The acoustoelectric current density as described by Shilton *et al.* [2], depends on the product of two sharply peaked functions of the electron velocity and only the electronic states in the vicinity of the Fermi level contributes to the acoustoelectric current. The electrons with velocities close to the velocity of the SAW feels the drag, where as electrons with different velocities feel the rapidly oscillating field of the SAW and remain unaffected. This drag is most prominent between the steps observed in the conductance values (see

Figure 2.9), where the energy of the electrons in the Fermi level is very low, and therefore the interaction time of the electrons and the SAW diverges.

Further investigations outside the ballistic regime revealed an interesting acoustoelectric behaviour, where the effect of single-electron transport by SAWs was captured. When the wavelength of a SAW is smaller than the 1-D channel length, the acoustoelectric current was found to be quantized in units of $ef$ where $e$ is the electronic charge and $f$ is the frequency of the SAW. As a function of gate voltage, the acoustoelectric current was found to increase in steps corresponding to the transfer of an integer number of electrons per SAW cycle (see Figure 2.10) [3].

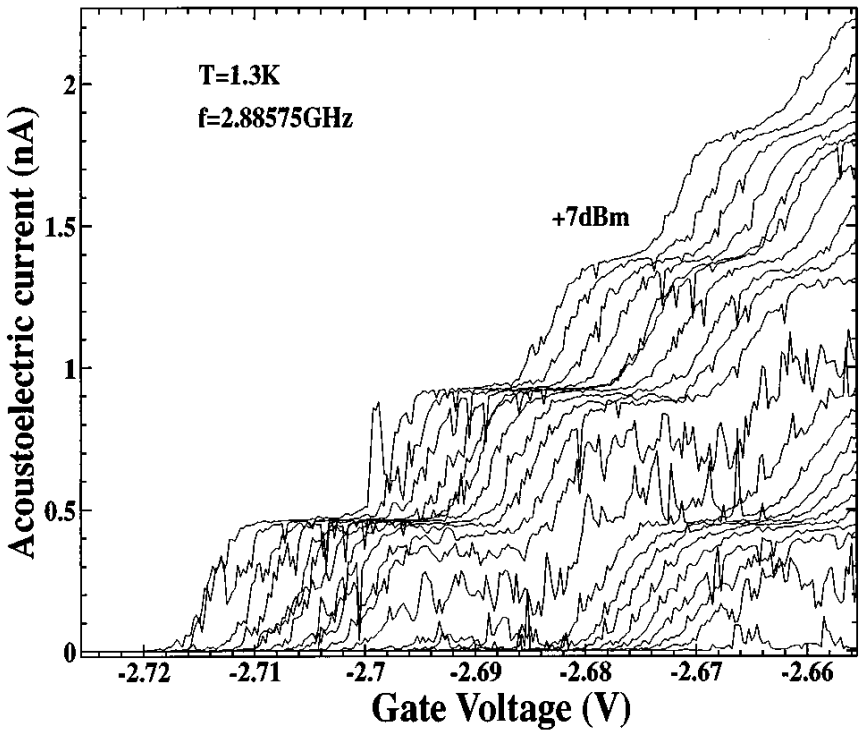


**Figure 2.10** Acoustoelectric current as a function of gate voltage for different SAW intensities. The leftmost curve represents 7 dBm power level that decreases by 0.2 dBm for successive curves (illustration taken from [3]).

When the 1-D channel defined by split gates is pinched off, a potential hill is created and the electrons trapped in the trough of the SAW travel up hill with it. The number of electrons trapped in a wave depends on its amplitude as schematically shown in Figure 2.7. At the entrance of the channel, if the local potential minima of the SAW is not big

enough to account for the Coulombic repulsion of the electrons in the wave, some of the electrons are knocked back. With the help of gate voltage, more electrons can be carried up hill by the SAW. Hence, the intensity of the SAW and the gate voltage can be used to control the single electron transport in such systems. A qualitative analysis of the quantized current can be found in the literature [50–52]. Such control over the transport of single electron has generated numerous concepts such as photon trains [53], quantum computation using electrons trapped in SAWs [48], and accurate current standards [54].

From a metrological perspective it is important to perform experiments to resolve the 'electrical triangle', which illustrates the relationship between the current, voltage, and resistance as given by Ohm's law in terms of the fundamental quantities Planck's constant $h$ and electron charge $e$ (see Figure 2.11).

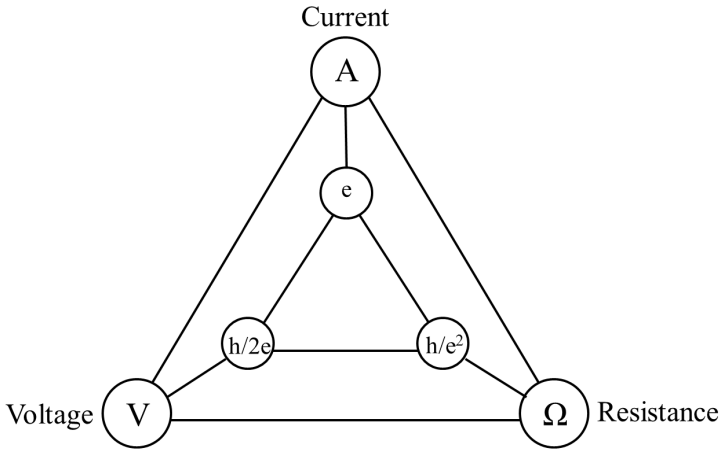


**Figure 2.11** Electrical triangle illustrating the relationship between the current, voltage and resistance in terms of the fundamental quantities Planck's constant h and electronic charge e.

The quantization of current in 1-D channels provides an exciting possibility to realise this experimentally at a fundamental level, but it requires a great deal of accuracy to perform such experiments. The relative uncertainty in measuring the current has to be smaller than 1 part in $10^7$ [54], considering the fact that the acoustoelectric current measured is of the order of nA, it would need a resolution of $10^{-16}$ A. This is significantly better than the conventional devices based on the Coulomb blockade phenomenon where the order of the current measured is in pA [55].

SAWs can also be used for the propagation and detection of electrons in well separated quantum dots, required for various quantum electro-optical measurements involving single electrons and photons [56]. The trapping of electrons in the SAW prevents the loss of quantum information stored in the electron's spin and charge, that happens otherwise when the electron interacts with other electrons in the Fermi sea. SAW-based single electron transport devices can also be potentially used in quantum computers for building complex quantum gate networks. A 'flying qubit' design was proposed to perform single and double-qubit operation by using such networks [48]. SAWs can be employed to dissociate the optically generated excitons into electron-hole pairs that can be trapped in the moving potential super-lattice of the SAW. This spatial separation of the electron-hole pair drastically increases the recombination time by several orders of magnitude compared to an un-separated electron-hole pair [12]. They can recombine efficiently to release a photon after the prolonged separation that can act as an optical delay line. The periodic transport of electrons and holes by a SAW at localised single, or an array of, quantum dots can possibly be used for generating single- or N-photon devices in quantum optical applications [53].

### 2.4.2 Sensor Applications

The traveling SAWs are confined to a very thin region near the surface of the piezoelectric material. This acoustic confinement makes them very sensitive to anything in contact with the material's surface. Any interaction with the adsorbed molecule in the form of mass loading or change in elasticity of the material could drastically change the attenuation and velocity of the SAW. This property, along with the possibility of having large area devices makes them suitable for sensing applications. The wireless sensing process and low production cost of SAW-based devices are some of the crucial advantages over other sensors used for wireless strain and temperature measurements [57]. The sensitivity to mass loading makes SAW devices an obvious candidate for gas sensors [58], some of which involve a thin semiconductor film on the piezoelectric substrate. Typically the temperature, pressure, and humidity changes can be detected by the attenuation and velocity

changes in the SAW, for example SAW-based relative humidity sensors [46] are found to be applicable over a wide range of relative humidity with fast response times during both adsorption and desorption processes. In addition to the sensing through the measurement of SAWs, these hybrid thin-film SAW devices can also detect the specific gas molecules via the change in their conductivity, mobility, and carrier concentration that can be measured in the form of acoustoelectric current. An exciting prospect for these systems is the use of graphene, which has a mono-atomic thickness and can be modified for selective gas sensing. Thin graphene-like nano-sheets have been tested for hydrogen and carbon monoxide sensing [23], and gas loading of air and argon on graphene-quartz SAW devices has been studied [33]. With the exciting properties of graphene, that we will discuss in the next chapter, there is a lot to be explored in the field of graphene-SAW sensors.

In summary, we discussed the origin of SAWs, its generation on the surface of a piezoelectric material with the help of single- and double-electrode transducers , and its importance in probing the electrical properties of low-dimensional materials. This work is focused on the interaction of SAWs with graphene, which is a 2DEG. As described in this chapter, this interaction can be described using a relatively simple classical relaxation model, which gives the attenuation and velocity shift of the SAW in the form of a non-monotonic function of the conductivity of graphene. In the following chapters, this model will be used to explain the acoustoelectric current observed in graphene.

# 3 Graphene

## 3.1 Overview

Graphene is the thinnest possible layer of graphite, a mono-layer of $sp^2$ hybridised carbon atoms arranged in a hexagonal lattice. It can be considered as the fundamental building block for all the graphitic forms of carbon (see Figure 3.1), which can be rolled into bucky balls or fullerene (0-D), carbon nanotubes (1-D) and stacked into graphite (3-D) (D refers to dimension). Although single-layer graphite has been under study since late 1940's, the term "graphene" was first coined by Mouras *et al.* in 1987 [59]. In 1947, P.R Wallace [60] investigated the band structures of graphene and highlighted its unusual semi-metallic properties before focusing his research on graphite. At that time, two-dimensional materials were believed to be thermodynamically unstable at any finite temperature and were presumed not to exist. Based on his general theory of second order phase transitions, Landau [61] argued that long range order in two dimensions is not possible. Peierls [62] reached the same conclusion qualitatively, when he used the harmonic approximation to extend his quantitative argument given for the one dimensional case to two dimensions. This theory of unstable low-dimensional crystal lattices proposed by Landau and Peierls in the 1930's remained uncontested for a long time and branded 2-D systems as only of theoretical importance. In 1962, the computer simulation experiments by Alder and Wainright [63] did show the possibility of stable two dimensional fluid and solid states, but the arguments were not irrefutable. Any ambiguity in the non-existence of 2-D systems were terminated by Mermin (in 1968), who developed the theory of Landau and Peierls by testing it for a large class of inter-particle interactions on a rigorous basis without using

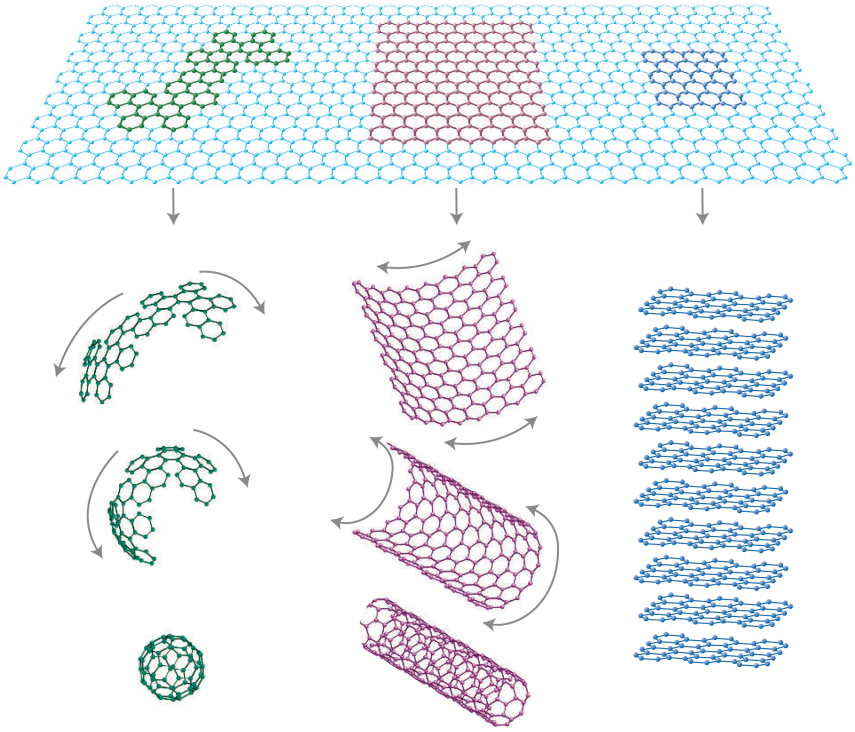

**Figure 3.1** 2-D Graphene and other graphitic forms: 0-D bucky balls; 1-D nanotubes and 3-D graphite (illustration taken from [4]).

either the harmonic approximation or an order-parameter expansion [64]. His analysis showed the non-existence of positional long range order in two dimensions but also acknowledged the presence of some long range orientation order, which was supported by conclusive experimental evidences showing that as the size of the low dimensional crystals grow above several nanometers, the phonon density available for thermal vibrations integrated over the 3-D space rapidly grows and forces the low dimensional crystals to either transform into stable 3-D structures or to decompose into small clusters [65]. Two dimensional materials were seen only as an integral part of their 3-D structures but they had no physical significance of their own. However, graphene continued to be a part of auxiliary studies for carbon nanotubes and graphite. There were attempts to chemically exfoliate the strongly layered materials, specifically the intercalated graphite that resulted in re-stacked and scrolled multilayer sheets [66]. It was only in 2004 that A. Geim and K. Novoselov were successful in isolating a single-layer graphene from graphite flakes using an adhesive tape [15].

Mechanically exfoliated graphite flakes of tens and hundreds of layers were reported earlier [66], but single-layer graphene remained undetected. With the benefit of hindsight, the missing case of graphene could have been due to a number of reasons. For example: these single-layer flakes occur in great minority compared to the other multi-layered exfoliated deposits; they have no signature in transmission electron microscopy; and they are transparent to the visible light on many substrates. Geim's group used oxidised silicon substrates that provided a subtle contrast difference between graphene and the substrate under an optical microscope, which proved critical in locating graphene. This technique was essentially like "finding a needle in a haystack", as painstaking efforts were needed to locate graphene among several graphite layers. But over the years it has developed as a skill and still remains the technique of preference for basic research and for fabricating proof-of-concept devices, as it produces crystals of high structural and electronic quality. The experiments conducted on graphene established that it is stable on top of non crystalline substrates, in suspensions and even as a free standing membranes contrary to earlier belief [15][67]. Studies done under transmission electron microscopy revealed that graphene exhibits intrinsic microscopic roughening that leads to its stability, which is not in complete disagreement with Mermin's theory as it does not forbid having "nearly" two-dimensional systems [67].

Apart from proving that stable 2D membranes can exist, graphene's exceptional electrical [5], mechanical [17][68], and optical [69] properties have attracted considerable interest. For example, the electrical conductivity in the plane of graphene, *i.e.* a single layer of graphite, is 100 times more than that between two layers of graphite [60]. The charge carriers in graphene can undergo ballistic transport (up to 3 $\mu$m) at sub-micrometer scale even at room temperature [70]. It can achieve high carrier mobilities >200,000 $cm^2V^{-1}s^{-1}$ in the absence of extrinsic disorder even at high carrier densities (>$10^{12}$ $cm^{-2}$) [71]. A large Young's modulus (>0.5 TPa) and high spring constants of up to 1-5 $Nm^{-1}$ have been measured in graphene sheets [17]. It has unique morphological properties with specific surface areas predicted to be >2500 $m^2g^{-1}$, which have been measured to be >270-1550 $m^2g^{-1}$ [72]. It has opened gates for a whole class of two-dimensional (2-D) materials like molybdenum disulfide ($MoS_2$) [73], silicene [74] and germanane [75]. Although 2-D

materials have always been of theoretical interest, the discovery of graphene has initiated intensive experimental research in this field.

Over the last decade graphene research has grown in leaps and bounds, and huge efforts are being made to realise its potential in various applications, for instance: a graphene/n-Si combination was found to improve the power efficiency of solar cells by a factor of 4.5 % [76] and is believed to perform better than conventional indium tin oxide (ITO)-based solar cells owing to the tunability of its work function; in fuel cells graphene sheets are used to modulate the electrocatalysis and electrochemical reaction in a controlled fashion [77], and makes these fuel cells more cost-effective by minimising the use of expensive metals like platinum (Pt) in them; graphene-silica composites as transparent conductors [78] have been shown to be more robust, easy to fabricate and free from the long term ion-diffusion problem encountered by other materials such as ITO; chemically modified graphene can be used as an ultra-capacitor for high performance energy storage devices [79]; and its quantum electronics applications could lead to new nano-photonics, and terahertz (THz) devices [80]. Furthermore, it can also be used as chemiresistors in chemical sensors [81][82], and in micro and opto-electronics [83][84]. In contrast to all the advancements in graphene applications in various fields, its potential in acoustoelectric devices has been relatively unexplored. In this work, we aim to study the acoustoelectric response in graphene when it is encountered by SAWs.

## 3.2 Properties of Graphene

### 3.2.1 Band Structure

Graphene has a hexagonal arrangement of carbon atoms in a plane with $sp^2$ hybridised valence orbitals. The electronic configuration of carbon is $1s^2\ 2s^2\ 2p_x^1 2p_y^1 2p_z^0$. The 2s, $2p_x$ and $2p_y$ orbitals hybridise to form three strong $\sigma$ bonds in the trigonal planar structure, and the $2p_z$ orbitals of the neighboring atoms that are perpendicular to the plane overlap to form delocalised $\pi$ (valence) and $\pi^*$ (conduction) bands. The $\sigma$ bond determines the

robustness of the lattice structure whereas the $\pi$ bond is responsible for its peculiar electronic properties. The hexagonal graphene structure can be seen as a triangular lattice of two atoms per unit cell as basis. The lattice vectors are given as $a_1 = \frac{a}{2}(3, \sqrt{3})$ and $a_2 = \frac{a}{2}(3, -\sqrt{3})$ where $a = 1.42$ Å is the C-C bond length. The corresponding reciprocal lattice vectors are $b_1 = \frac{2\pi}{3a}(1, \sqrt{3})$ and $b_2 = \frac{2\pi}{3a}(1, -\sqrt{3})$. The Brillouin zone formed in the reciprocal lattice space has two high-symmetry points $\mathbf{K}$ and $\mathbf{K'}$, which are given by

$$\vec{\mathbf{K}} = (\frac{2\pi}{3a}, -\frac{2\pi}{3\sqrt{3}a}), \vec{\mathbf{K}'} = (\frac{2\pi}{3a}, \frac{2\pi}{3\sqrt{3}a}) \tag{3.1}$$

The honeycomb lattice of graphene and the Brillouin zone are shown in Figure 3.2. The band structure of graphene can be determined by using the nearest neighbour tight-binding approach for electrons in the $\pi$ state, as described by Wallace [60]. Considering only the nearest neighbour hopping of electrons, the Hamiltonian of the system is given by

$$\hat{H}(\vec{k}) = \begin{pmatrix} 0 & tS(\vec{k}) \\ tS^*(\vec{k}) & 0 \end{pmatrix} \tag{3.2}$$

where $\vec{k}$ is the wave vector, $t$ is the hopping parameter and

$$S(\vec{k}) = \sum_{\vec{\delta}} e^{i\vec{k}\vec{\delta}} = 2\exp\left(\frac{ik_x a}{2}\right)\cos\left(\frac{k_y a\sqrt{3}}{2}\right) + \exp(-ik_x a) \tag{3.3}$$

The energy is given by

$$E(\vec{k}) = \pm t\left|S(\vec{k})\right| = \pm t\sqrt{3 + f(\vec{k})} \tag{3.4}$$

where

$$f(\vec{k}) = 2\cos(\sqrt{3}k_y a) + 4\cos\left(\frac{\sqrt{3}}{2}k_y a\right)\cos\left(\frac{3}{2}k_x a\right) \tag{3.5}$$

Since $S(\vec{\mathbf{K}}) = S(\vec{\mathbf{K}'}) = 0$, the effective Hamiltonian near $\mathbf{K}$ and $\mathbf{K'}$ becomes

$$\hat{H}_{\mathbf{K},\mathbf{K}'}(\vec{q}) = \hbar\nu_F \begin{pmatrix} 0 & q_x \mp iq_y \\ q_x \pm iq_y & 0 \end{pmatrix} \tag{3.6}$$

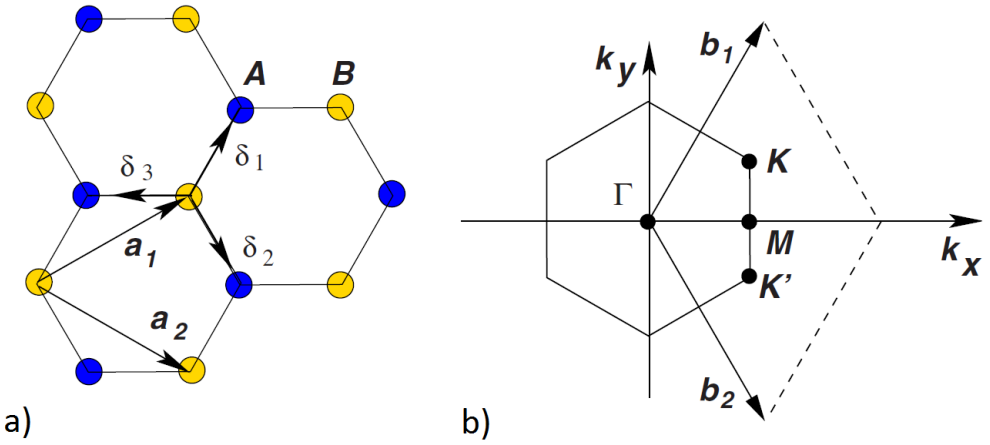


**Figure 3.2** a) Honeycomb lattice with lattice vectors ($a_1$ and $a_2$) and nearest neighbour vectors ($\delta_1$, $\delta_2$ and $\delta_3$) b) Brillouin zone with reciprocal lattice vectors ($b_1$ and $b_2$) with high symmetry points **K** and **K′** (illustration taken from [5]).

where $\vec{q} = \vec{k} - \vec{\mathbf{K}}$ and $\vec{k} - \mathbf{K}'$ at points **K** and **K′** respectively and $\nu_F = \frac{3a}{2}|t| \approx 10^6$ ms$^{-1}$ is the Fermi velocity near the **K** and **K′** points. Interestingly, the Fermi velocity in this case is independent of energy or momentum, unlike in common semiconductors.

If the next-nearest-neighbour hopping or the subsequent neighbours are taken into account it adds further terms with hopping parameter $t'$ , $t''$ and so on. For example if we consider the next-nearest neighbour hopping energy ($t'$), Equation (3.4) becomes

$$E(\vec{k}) = \pm t|S(\vec{k})| + t' f(\vec{k}) + ... \tag{3.7}$$

The energy dispersion of graphene as calculated for hopping parameters, $t$=2.7 eV and $t'$=-0.2$t$, is shown in Figure 3.3. It shows the conical structure at points **K** and **K′**, where the valence and conduction bands meet *i.e.* there is no band gap. These points are called charge neutrality or Dirac points. For pristine (undoped) graphene the Fermi energy level passes through these Dirac points such that it has a completely filled valence band and an empty conduction band.

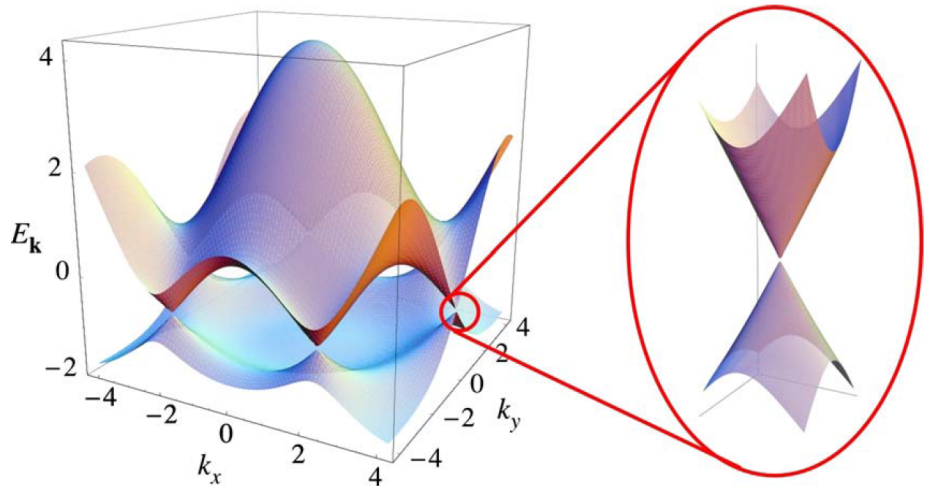


**Figure 3.3** The electron energy spectrum of graphene for $t$=2.7 eV and $t'$=-0.2$t$ (illustration taken from [5]).

### 3.2.2 Electrical Properties

#### 3.2.2.1 Massless Dirac Fermions

The band structure of graphene reveals a zero band gap, where the conduction and valence bands meet at charge neutrality points. In the reciprocal lattice space, these points are located at **K** and **K′** in the Brillouin zone (see Figure 3.2). The Hamiltonian near these points can be given by

$$\hat{H}_{\mathbf{K}} = -i\hbar\nu_F\vec{\sigma}\nabla \tag{3.8}$$

$$\hat{H}_{\mathbf{K}'} = \hat{H}_{\mathbf{K}}^T \tag{3.9}$$

where $\sigma$ refers to the pseudo-spin instead of the normal spin vector given by Equation (3.10). This is due to the interaction between the electrons and graphene sub-lattice that can be best described by pseudo-particles having pseudo-spins (only $\sigma_x$ and $\sigma_y$ are used to solve Equation (3.8)).

$$\sigma_0 = \begin{pmatrix} 1 & 0 \\ 0 & 1 \end{pmatrix}, \sigma_x = \begin{pmatrix} 0 & 1 \\ 1 & 0 \end{pmatrix}, \sigma_y = \begin{pmatrix} 0 & -i \\ i & 0 \end{pmatrix}, \sigma_z = \begin{pmatrix} 1 & 0 \\ 0 & -1 \end{pmatrix} \tag{3.10}$$

Equation (3.8) is a two-dimensional analogue of the Dirac Hamiltonian for massless fermions with a velocity $\nu_F \approx$ c/300, where c is the speed of light. Hence the points **K** and **K′** are also called Dirac points. Expanding Equations (3.6) and (3.7) near points **K** and **K′** shows a linear dispersion relationship between the energy and the wave vector:

$$E_{\pm}(\vec{k}) = \hbar\nu_F|k - K| \tag{3.11}$$

Because of the dimensionality the density of states vanishes at the Dirac point that gives rise to some profound properties such as: chiral anomalies [85] [86] which show Quantum Hall Effect (QHE) due to time reversal invariance even in the absence of any external magnetic field; relevance to high $T_c$ superconductors [87] resulting in enhanced uniform susceptibility and specific heat coefficients; unusual transport properties [88] [89] like half-integer QHE; and resembling meta-materials with negative refractive index [90].

#### 3.2.2.2 Electric Field Effect

The effect of electric field applied via a gate voltage allows control of the carrier concentration in a semi-conductor. The schematic of a typical device with Hall-bar geometry, which is commonly used to study this effect in graphene, is shown in Figure 3.4(a).

A source current $I_{xx}$ is passed through the source-drain contacts and the longitudinal potential drop $V_{xx}$ can be measured to calculate the conductivity of graphene. In the presence of a magnetic field B perpendicular to the plane of the bar, there is also a potential drop $V_{xy}$ across the transverse direction, which is used to calculate the Hall coefficient $R_H$. The top and back gates, separated from graphene by a dielectric layer, can be applied independently or together to induce carriers in graphene (see Figure 3.4(b)). In $Si/SiO_2$ substrates the insulating $SiO_2$ layer acts as a dielectric, whereas the Si, which is denegerately doped to make it conducting, can be used as back gate. For insulating substrates like lithium niobate, top gate configuration is needed to achieve conductance modulation in graphene. A positive (negative) gate voltage induces electrons (holes) in graphene, the charge density of which can be calculated if the gate capacitance is known.

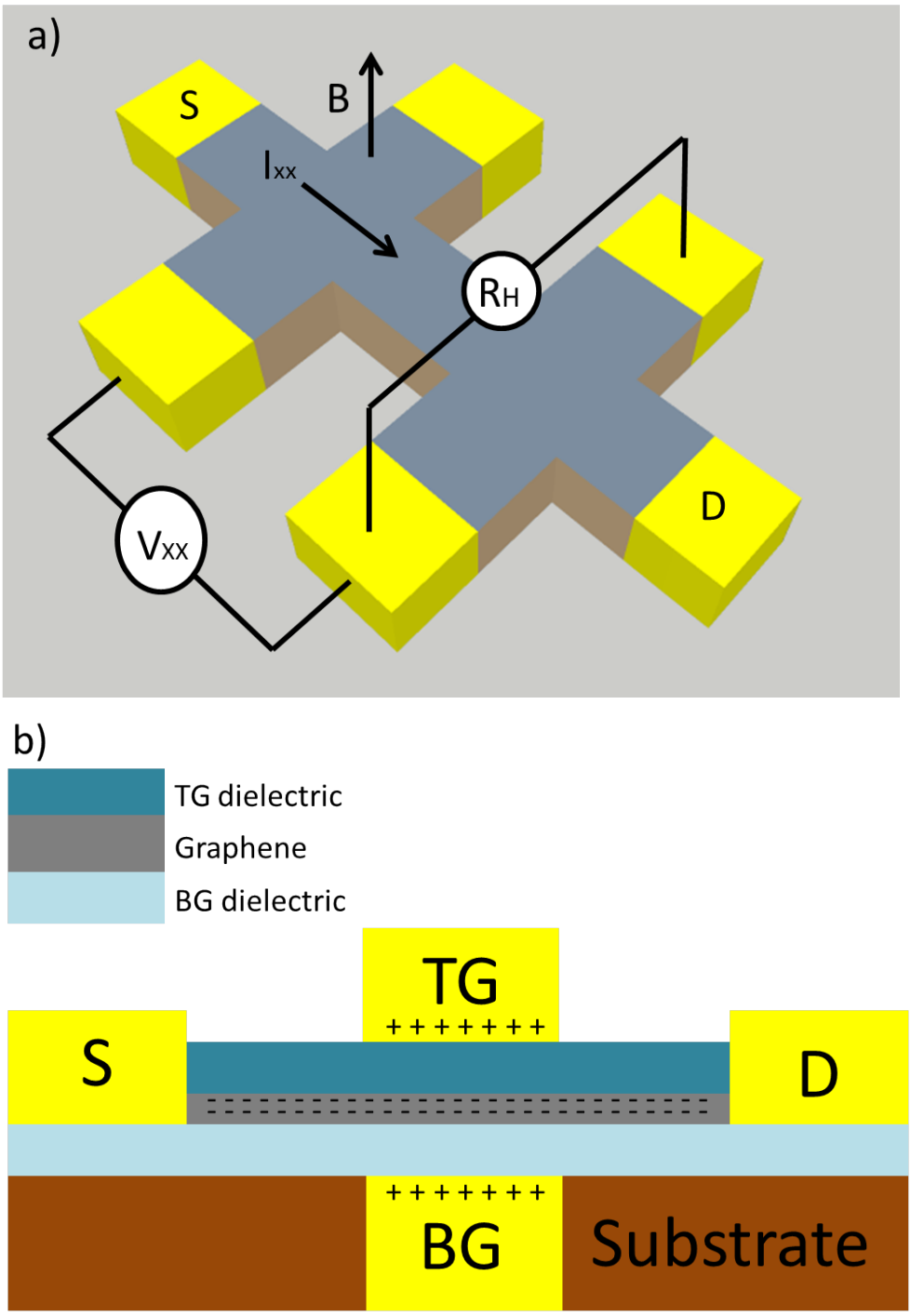


**Figure 3.4** a) A typical Hall-bar geometry used in the electric field effect measurement, where $I_{xx}$ is the source current passed between the source (S) and drain (D) contacts. $V_{xx}$ represents the longitudinal voltage drop, $R_H$ is the Hall coefficient measured in the transverse direction, and B is the magnetic field perpendicular to the Hall-bar geometry. b) The schematic of a typical device with top (TG) and bottom (BG) gates. The inset shows the different dielectrics that may be used for top and bottom gates.

For widely used $Si/SiO_2$ substrates of thickness 300 nm, the gate capacitance is known to be $1.15 \times 10^{-4}$ $Fm^{-2}$.

The experiments conducted for graphene on $Si/SiO_2$ reveals a sharp peak in sheet resistivity [15] of graphene when measured as a function of gate voltage $V_g$, as shown in Figure 3.5.

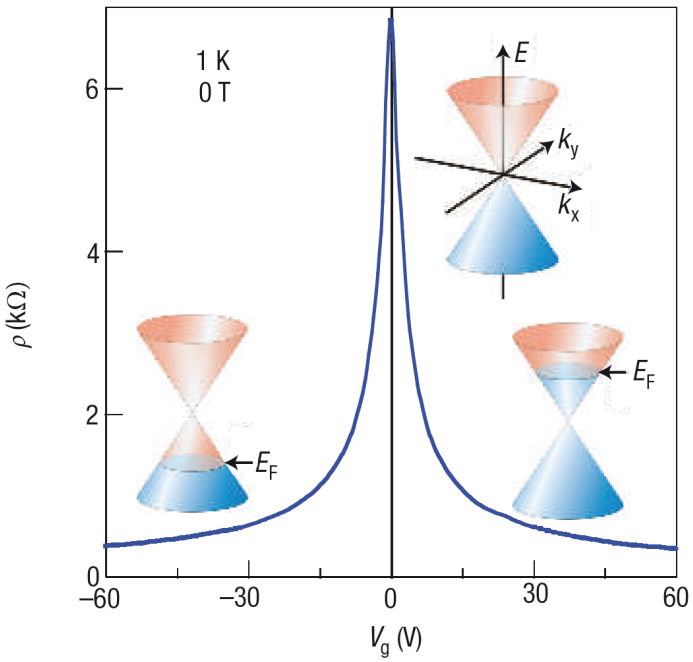


**Figure 3.5** The resistivity of graphene measured as a function of gate voltage in $Si/SiO_2$ substrate shows the ambi polar effect in graphene. The inset indicates the changes in the position of the Fermi level ($E_F$) as the carriers are induced with the help of the gate voltage (illustration taken from [4]).

This peak is termed as the Dirac peak corresponding to the charge neutrality point. In the vicinity of this point, the sheet conductivity $\sigma_{2D}$ is linear with respect to $V_g$ therefore the field effect mobility of the carriers (electrons and holes) can be calculated as

$$\mu = \frac{d\sigma}{dV}\frac{1}{C} \tag{3.12}$$

where $C$ is the gate capacitance per unit area.

In case of pristine graphene, the Dirac peak lies at $V_g$=0 V. Any dopants either in the

form of tape residues or absorbed water molecules push the Dirac peak away from $V_g$=0 V. For example, the exposure of graphene to water vapour and ammonia ($NH_3$) leads to p- and n-doping respectively [91], which correspondingly shifts the Dirac peak towards positive and negative $V_g$. The effect of doping on the conductivity and the position of Dirac peak was demonstrated by Chen *et al.* [92] through controlled doping of potassium in clean graphene samples under ultra-high vacuum (UHV) at low temperature. The relative shift in Dirac peak was attributed to the charge transfer between the graphene and absorbed molecules. First-principles calculation on graphene [93] predicts that such charge transfer can occur via two mechanisms : (i) The charge transfer due to the relative position of highest occupied molecular orbital (HOMO) and lowest unoccupied molecular orbital (LUMO) of the dopant with respect to the Fermi level of graphene. If the HOMO is above the Fermi level of graphene, there is a charge transfer from the dopant to graphene, whereas if the LUMO is below the Fermi level, charge transfers from graphene to the dopant. (ii) The relative mixing of HOMO and LUMO with the graphene orbitals, which scales with the overlap of the interacting orbital and the difference of their energy levels.

#### 3.2.2.3 Mobility

Ballistic transport (the transport of electrons with negligible resistance) over a range of 100 nm is typically observed in graphene [70]. At room temperature, a typical mobility value of 10,000 $cm^2V^{-1}s^{-1}$ for a carrier density of $n$=$10^{12}$ $cm^{-2}$ translates to a mean free path $l$ of the order of 100 nm, where $l$ is given by

$$l = \frac{h\mu}{2e}\sqrt{\frac{n}{\pi}} \tag{3.13}$$

where $h$ is the Planck's constant and $e$ is the electron charge. In the absence of extrinsic disorder the mobility values are expected to be >200,000 $cm^2V^{-1}s^{-1}$ [71], which is usually limited by charge impurity scattering. High mobility values approaching 200,000 $cm^2V^{-1}s^{-1}$ at low temperature have been reported in suspended graphene [94], where the weak electron-phonon interaction makes it possible to achieve even higher mobili-

ties, although it is fragile and susceptible to the ambient atmosphere. Recently, graphene encapsulated by hBN (hexagonal boron nitride) crystals have shown considerable improvement in mobility and structural stability compared to suspended graphene. It has been reported to have $\mu$>100,000 $cm^2V^{-1}s^{-1}$ even at room temperature for $n$=$10^{11}$ $cm^{-2}$ [70], which is predicted to rise up to 500,000 $cm^2V^{-1}s^{-1}$ when subjected to low temperatures, corresponding to an increase in mean free path from 1 $\mu$m to 3 $\mu$m.

Comparatively much smaller values of mobility have been reported for graphene grown by chemical vapour deposition (CVD) method, typically in the range 100-45,000 $cm^2V^{-1}s^{-1}$ [95][96][97]. The electronic properties of CVD graphene are strongly influenced by the defects, ripples, tears, wrinkles, impurities in the form of etchant residues or growth leftovers, and grain boundaries in particular. Several protocols have been developed to yield reasonably clean CVD graphene minimising the defects and impurities, but the grain boundaries are intrinsic to the growth mechanism by CVD method, where the graphene consists of large number of highly crystalline but randomly oriented graphene grains. The mobility obtained on single grain CVD graphene (exceeding 50,000 $cm^2V^{-1}s^{-1}$ at low densities) is found to be comparable to the quality of exfoliated graphene [97]. The mis-oriented graphene grains gives rise to line defects at the junction of grains dividing the graphene into high and low resistivity areas, which affects the overall mobility. A potential barrier model [98] can be used to qualitatively explain the effect of grain boundaries, according to which the overall mobility $\mu$ of the CVD graphene sample with the high (low) resistivity region of length $l_h$ ($l_l$), resistivity $\rho_h$ ($\rho_l$), and mobility $\mu_h$ ($\mu_l$) respectively can be expressed as:

$$\mu = \frac{\alpha}{\alpha + \beta}\left(\mu_h + 2\beta\mu_l\right) \tag{3.14}$$

where $\alpha$=$\rho_h/\rho_l$ and $\beta$=$l_h/l_l$. For typical conditions, $\alpha << 1$ and $\beta < 1$, the Equation (3.14) can be simplified as $\mu$=$\alpha\mu_h/(\alpha + \beta)$. With the increase in grain boundaries $\beta$ increases, and therefore the mobility decreases. This is supported by the experiments conducted on intra- and inter-grain CVD graphene, where the mobility of the latter was

found to be an order of magnitude smaller than the former [99].

#### 3.2.2.4 Temperature Dependence

The field effect performance of graphene is strongly limited by carrier scattering from impurity sites, surface phonons of the dielectric and acoustic phonons of graphene. The phonon scattering naturally gives a temperature dependence to the resistivity $\rho$ of graphene. For low carrier densities ($10^{12}$ cm$^{-2}$), $\rho$ for exfoliated graphene on Si/$SiO_2$ shows a linear dependence at lower temperatures (<150 K) and increases rapidly with the increase in temperature above 150 K [100][101], which may be attributed to the thermally activated optical phonons in $SiO_2$, thermally quenched graphene ripples or Coulomb impurities. These extrinsic effects becomes less evident at high carrier densities ($10^{14}$ cm$^{-2}$) due to the enhanced carrier screening. The observations for high carrier density shows a linear dependence on temperature $T$ at high temperatures (>150 K), whereas for low temperatures (<150 K) $\rho \propto T^4$ [100]. The low temperature behaviour is different from the conductors where $\rho \propto T^5$, which is due to the 2-D nature of electrons and phonons in graphene.

The graphene made by CVD method inevitably brings a lot of impurities in the form of residues, inhomogeneous charge puddles and non-uniformity due to grain boundaries, tears, wrinkles, *etc.* The temperature dependence of the conductivity of CVD graphene gets strongly affected by this charge impurity scattering. It was observed that at low densities and low temperatures, the carrier activation across the potential landscape created by the inhomogeneous charge densities determines the temperature dependence of the conductivity. Heo *et al.* [102] demonstrated a metallic character ($d\rho/dT>0$) for high mobility samples irrespective of the carrier density. The low mobility samples however show a non-monotonic behaviour with $d\rho/dT<0$ for low temperatures and $d\rho/dT>0$ for high temperatures. This non-monotonicity is a result of the combination of two competing mechanisms of charge transport: the diffusive metallic transport, driven by phonons and carrier screening; and local activated transport driven by the potential fluctuations created by the inhomogeneous charge puddles and Fermi surface effects. These mechanisms

are non-trivially dependent on carrier densities and temperature [103][104]. A metallic behaviour is observed at high carrier densities where the charge screening and phonons dominate the charge transport characteristics, as compared to the low carrier densities where the Fermi surface effects and carrier activation across charge puddles play an important role. At higher temperatures, the phonon scattering effects eventually dominate all other mechanisms and graphene exhibits a metallic character irrespective of the carrier density. At low temperature and lower densities, the local carrier activation across the potential fluctuations due to the random inhomogeneous charge puddles and impurities becomes significant and contributes to the temperature dependent conductivity. This amounts to a complex temperature dependence of the conductivity of CVD graphene which may be conducting, insulating ($d\rho/dT<0$), or a non-monotonic function of both, depending upon the mobility, carrier density and range of temperature studied.

### 3.2.3 Mechanical Properties

The mechanical properties of graphene has also attracted a lot of attention due to its potential application in areas such as nano electromechanical systems (NEMS). Density functional theory, quantum mechanics, molecular dynamics (MD) simulations and continuum mechanics were implemented as theoretical methods to investigate graphene's elastic and mechanical properties. Different groups have predicted the intrinsic graphene strength to be of the order of 100 GPa. For instance Lee *et al.* [105] measured the intrinsic strength of graphene to be 42 $Nm^{-1}$ that corresponds to an intrinsic stress value of 130 GPa, among the highest ever measured. The study of anisotropic behaviour of single-layer graphene by Ni *et al.* [68] demonstrates that the armchair arrangement is stronger than the zig-zag arrangement. Any defect in the form of vacancies, dislocations, topological defects (rings instead of hexagons) and heterogeneous defects (due to doping) are expected to significantly reduce the strength of single-layer graphene [106]. Frank *et al.* [17] used an AFM tip of spring constant 2 $Nm^{-1}$ to push the suspended graphene sheets, and the deflection of the tip was measured to yield a spring constant of 1-5 $Nm^{-1}$ corresponding to a Young's modulus of 0.5 TPa. Owing to its high Young's modulus and elasticity along with the

high surface area, graphene-based NEMS resonators are expected to be extremely sensitive as ultra-sensitive detectors for force and mass measurements. Schedin *et al.* [81] have shown the effectiveness of graphene sensors in detecting the molecular mass, charge and chemicals absorbed by them.

The piezoelectric coupling of surface acoustic waves with graphene can be used to probe both the electrical and mechanical properties of graphene. In the following chapters, we have investigated the electrical properties of graphene using SAWs of different wavelengths at different temperatures as a function of SAW intensity.

## 3.3 Graphene Preparation

Huge efforts are made in developing methods for consistently producing high-yield good-quality graphene. The primary methods of making graphene may be classified under mechanical exfoliation, epitaxial growth, nanotube slicing, reduction of graphene-oxides, and intercalation of graphite layers [107]. Large-area epitaxial growth of graphene on SiC (silicon carbide) [108] has been shown to be of high quality, but the only drawback remains the transfer of graphene on insulating substrates like $SiO_2$ for electronic applications, which requires either the graphene to be peeled from the SiC or the SiC to be etched, neither of which is an efficient process. The growth of graphene on transition metals via chemical vapour deposition method has developed as the most promising technique for inexpensive growth of large-area graphene films, which along with the mechanical exfoliation technique is discussed in the following section.

### 3.3.1 Exfoliation

Graphene was discovered by a very simple yet novel technique, where the graphite flakes were mechanically exfoliated using adhesive tape and transferred on oxidised silicon substrates. It is essentially the mechanical exfoliation of Kish graphite or highly oriented pyrolitic graphite (HOPG) crystals several times such that some mono-layers get cleaved

in the process. The adhesive tape with these exfoliated crystals containing hundreds and thousands of different number of layers of graphite is stamped on an oxidised silicon wafer, which is then scanned under an optical microscope to identify monolayers. Ideally, this micro-mechanical cleavage technique should work on any substrate where the adhesion between the substrate and the graphene layer is strong enough to counter the inter-layer force. Although this method produces graphene every time, it also leaves a lot of tape residues and many-layer graphite flakes. Scanning the substrate under an optical microscope is time consuming but still is the preferred way for preliminary characterisation of graphene. One of the big disadvantages of this method is the unreliability involved, where the shape, size, number of layers and position of graphene is subject to chance. Over the years, quick identification of graphene under the optical microscope has developed as a skill but no breakthrough has been made so far in consistently producing single-layer graphene at the desired position by mechanical exfoliation.

### 3.3.2 Chemical Vapour Deposition

One of the most promising techniques for inexpensive growth of large-area graphene films is the chemical vapor deposition (CVD) of hydrocarbons on transition metal substrates, such as nickel (Ni), copper (Cu) and palladium (Pd) [96]. The principal growth mechanism in CVD is the decomposition of a carbon source (commonly hydrocarbons like $CH_4$) at high temperatures, which become adsorbed by the transition metals. The substrates are typically annealed at 900-1000 °C under $Ar/H_2$ atmosphere to increase the grain size for large-domain graphene growth. Then it is exposed to the hydrocarbon, which decomposes and the carbon atoms are adsorbed by the substrate. As the sample cools down in inert atmosphere (like Ar), the adsorbed atoms come to the surface and arrange themselves to form graphene. CVD graphene grown on Ni shows a typical mobility of $\approx 3000\ cm^2V^{-1}s^{-1}$ but has often been found to be non-homogenous (single- to few-layer graphene growth was reported near grain boundaries) [109]. The graphene grown on thin Cu foils however was found to be homogenous and independent of the growth time, heating or cooling rates [96]. The growth process on Cu is self-limiting process and is restricted to single-layer graphene

only. As large as 30 inches of single-layer graphene have been reported on Cu [110]. Apart from being inexpensive, Cu is also relatively easy to etch which makes it the preferred choice of substrate for graphene growth. The Raman characterisation of CVD graphene on Cu shows that more than 93 % of the given area is typically covered by single-layer graphene with 2D/G peak intensity ratio of 2-4 (please see Section 3.4.2). The biggest advantage of this method is the possible transfer of graphene to any desired substrate by covering its top layer with a polymer resist (like polymethyl methacrylate (PMMA)) and etching the Cu from underneath. Different transfer techniques have been developed to ensure a good quality transfer, for example Suk *et al.* developed a dry transfer technique using polydimethylsiloxame (PDMS) to transfer CVD graphene to any arbitrary substrate [111]. The quality of the transfer can be tested by measuring the mobility, sheet resistance or conductance of the sample. Bae *et al.* have reported a mobility of 5000 $cm^2V^{-1}s^{-1}$ and 7000 $cm^2V^{-1}s^{-1}$ at room and low temperature respectively [110] for a graphene sheet of resistance 30 $\Omega/\square$, transferred using wet transfer method to release the graphene from Cu.

#### 3.3.2.1 Applications

Current efforts to utilise CVD graphene have targeted a number of areas, including: high-speed, transparent, flexible electronics; chemical and biochemical sensors; RF communications; optoelectronic devices; composite materials; photovoltaic cells; and energy storage. Kim *et al.* have demonstrated the use of transferred graphene as a highly conducting and transparent electrodes in flexible electronics [109]. The semiconductor most commonly used as a transparent electrode is ITO, which has several limitations including increasing cost due to its scarcity, difficulties in processing and a brittleness that prevents its use in flexible components. Both industrial and academic researchers are seeking to overcome these limitations by employing materials such as carbon nanotubes (CNTs) and graphene sheets in place of ITO. Arco *et al.* [112] have demonstrated the high resilience of graphene electrodes under a bending angle of 138° compared to the ITO electrodes, which displayed cracks under bending of 60°.

Photodetectors made of graphene could absorb a wide range of wavelength (from the ultra-violet to terahertz range). In addition, ultra-fast response time can be achieved owing to the high mobilities of graphene [113]. The operational band-width, which is typically limited by the transit time (duration of photogenerated current), of graphene photodetectors (1500 GHz) surpasses that of the conventional photodetectors [114].

Lastly, graphene's prospects as biosensing material have been demonstrated by in numerous areas; functionalised CVD graphene with specific redox agents were used to detect the glucose and glutamate molecules by measuring the relative change in conductance of graphene [115], Wang *et al.* [116] used N-doped graphene to enhance the electron transfer kinetics of glucose oxidase and it was also found to exhibit excellent electrocatalytic activity for the reduction of hydrogen peroxide.

## 3.4 Characterisation Method

Modern imaging techniques like atomic force microscopy, scanning electron microscopy and tunneling electron microscopy have not been very successful in identifying graphene among many graphite layers. Generally optical microscopy is used for the preliminary identification of graphene flakes followed by Raman spectroscopy, which gives an unambiguous, non-destructive evidence for distinguishing up to 5 layers of graphene. The following section briefly discusses these characterisation techniques.

### 3.4.1 Optical Microscopy

The atomically thin graphene flakes when transferred on the oxidised silicon ($SiO_2$) substrate add an optical length to the light reflected off the substrate. This provides a very small contrast difference that can be processed by the human eye to distinguish the single and the multi-layer graphene flakes from the substrate. This contrast can be enhanced by choosing a suitable thickness of $SiO_2$ in the substrate [4]. Blake *et al.* investigated the contrast dependence of $SiO_2$ thickness for different wavelengths of light and found that in

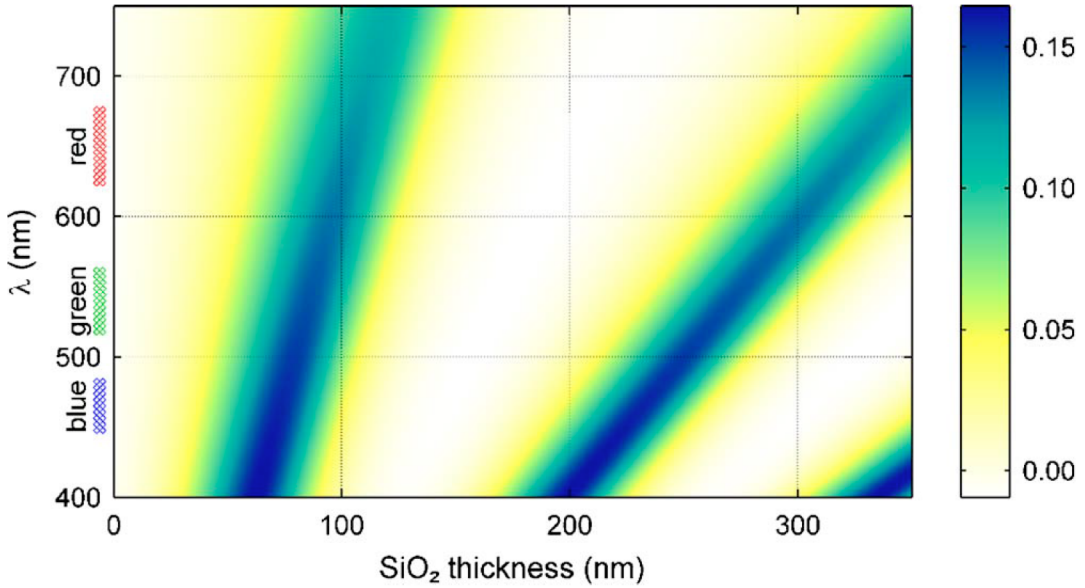


**Figure 3.6** Colour plot of contrast as a function of $SiO_2$ thickness and wavelength (illustration taken from [6]).

addition to the extra path length, the inherent opacity of graphene was also responsible for the contrast [6]. Figure 3.6 shows the contrast obtained on $SiO_2$ as a function of wavelength of light used and the thickness of $SiO_2$. It was found that the visualisation can be enhanced by using suitable filters. A model based on Fresnel equations show that the $SiO_2$ thickness of 90 nm and 280 nm provides the best contrast for graphene detection [6]. Additionally, green filters were found to offer the greatest viewing comfort for graphene on $SiO_2$ substrates, whereas blue filters are recommended when the graphene is on 50 nm $Si_3N_4$, and unfiltered white light is advised when viewing graphene on 90 nm of PMMA [6].

### 3.4.2 Raman Spectroscopy

Raman spectroscopy uniquely captures the electronic spectrum of graphene. Therefore, it is a highly reliable technique for identifying graphene layers. It is based on the inelastic scattering of monochromatic light in the near-infrared, visible and near-ultraviolet regions. The photons of the incident monochromatic light are absorbed by the electrons in the sample, which excites them to higher energy levels. When these excited electrons

relax back to the ground state, they re-emit photons, which can be of the same frequency as the incident one or may be different. The emission of photons of the same frequency is called Rayleigh or elastic scattering, whereas the emission of higher or lower frequency photons is called Raman or inelastic scattering. The molecules for which inelastic scattering is observed are called Raman-active molecules, and the energy levels involved in this scattering are called Raman-active modes. The shift in the frequency $\Delta w$, which is also called Raman shift is typically reported in terms of wavenumbers as given by

$$\Delta w = \frac{1}{\lambda_0} - \frac{1}{\lambda_1} \tag{3.15}$$

where $\lambda_0$, and $\lambda_1$ are the wavelengths of the incident and emitted photons, respectively. The Raman shift $\Delta w$ is typically measured in the units of $cm^{-1}$ and provides information about the vibrational, rotational and other low frequency modes of a sample.

The intense Raman features observed in graphite at 1350 $cm^{-1}$ (D band), 1580 $cm^{-1}$ (G band) and 2700 $cm^{-1}$ (2D band) are used in graphene characterisation. Out of all the zone center optical modes predicted by the group theory analysis for hexagonal graphite only $E_{2g}$ is Raman active. The G-band is assigned to the in-plane $E_{2g}$ mode, the D band is attributed to the $A_{1g}$ zone-edge mode, which is silent in defect free graphite, whereas the 2D peak is due to the second order double resonant scattering from the zone boundary. As the zone boundary phonons do not follow Raman fundamental selection rules, they are also not visible in the first order Raman spectra of defect less graphite. The in-plane vibrations of the graphite layers gives rise to these bands and the spectra evolves depending on the structural quality of these layers [117]. In a pristine single-layer graphene, the D peaks do not show up in the Raman spectra whereas the 2D peak, which is much weaker compared to the G peak in graphite, becomes 3-4 times more intense. The intensity of the G peak remains fairly consistent for bulk graphite and graphene [7]. The 2D peak splits into $2D_{1B}$, $2D_{1A}$, $2D_{2A}$, $2D_{2B}$ due to the splitting of electronic bands, out of which $2D_{1A}$ and $2D_{2A}$ are the prominent ones that evolves the most with the number of layers in graphene. The reason for a strong 2D peak in graphene is the double resonance that connects the electronic band structure with the phonon modes. This double resonance

involves four virtual transitions as explained by Thomsen *et al.* [118] (see Figure 3.7).

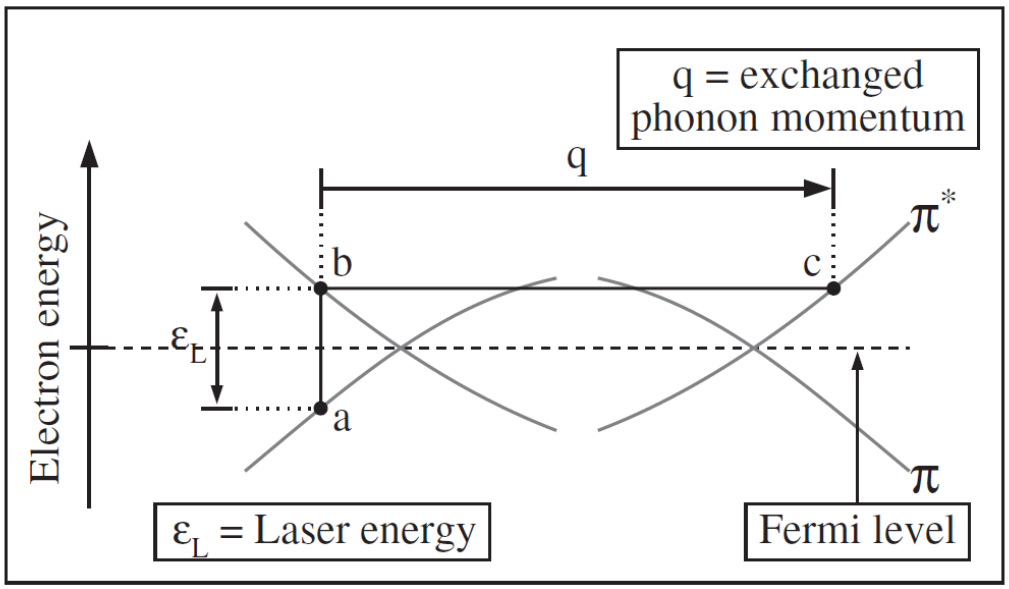


**Figure 3.7** A schematic showing the double resonance of the 2D peak in single-layer graphene (illustration taken from [7]).

Firstly, the laser excitation causes a electron-hole pair generation at the **K** point according to the energy difference between the conduction and the valence band leading to a vertical transition from ($a \rightarrow b$). Then, due to monotonous phonon dispersion the electron-phonon scattering leads to a transition in the second state ($b \rightarrow c$) with an exchange of momentum **q**. Then the electron is elastically scattered back with **-q** momentum exchange. This is where the double resonance occurs ($c \rightarrow b$). Finally the recombination process happens leading to the transition back to the initial state ($b \rightarrow a$). For multilayer graphene, the interaction between the layers results in the splitting of the energy band that can be captured by the evolution of the 2D peak. For example, in bi-layer graphene the corresponding transition when excited by a laser involves momentum corresponding to $q_{1B}$, $q_{1A}$, $q_{2A}$, $q_{2B}$, which have different frequencies arising due to the strong electron-phonon coupling near the **K** point. Similarly, the band structure and correspondingly the Raman spectrum, evolves with the increasing number of layers of graphene. The Raman spectra of graphene is compared with graphite in Figure 3.8(a) illustrating the difference in 2D/G peak ratios. Even though the Raman spectra of more than five layers start resembling graphite, it

still provides conclusive evidence for distinguishing between few-layers graphene (up to 5 layers) as shown in Figure 3.8(b) and (c), where the evolution of the 2D peak with the layers of graphene is illustrated using a laser beam of 514 nm and 633 nm respectively.

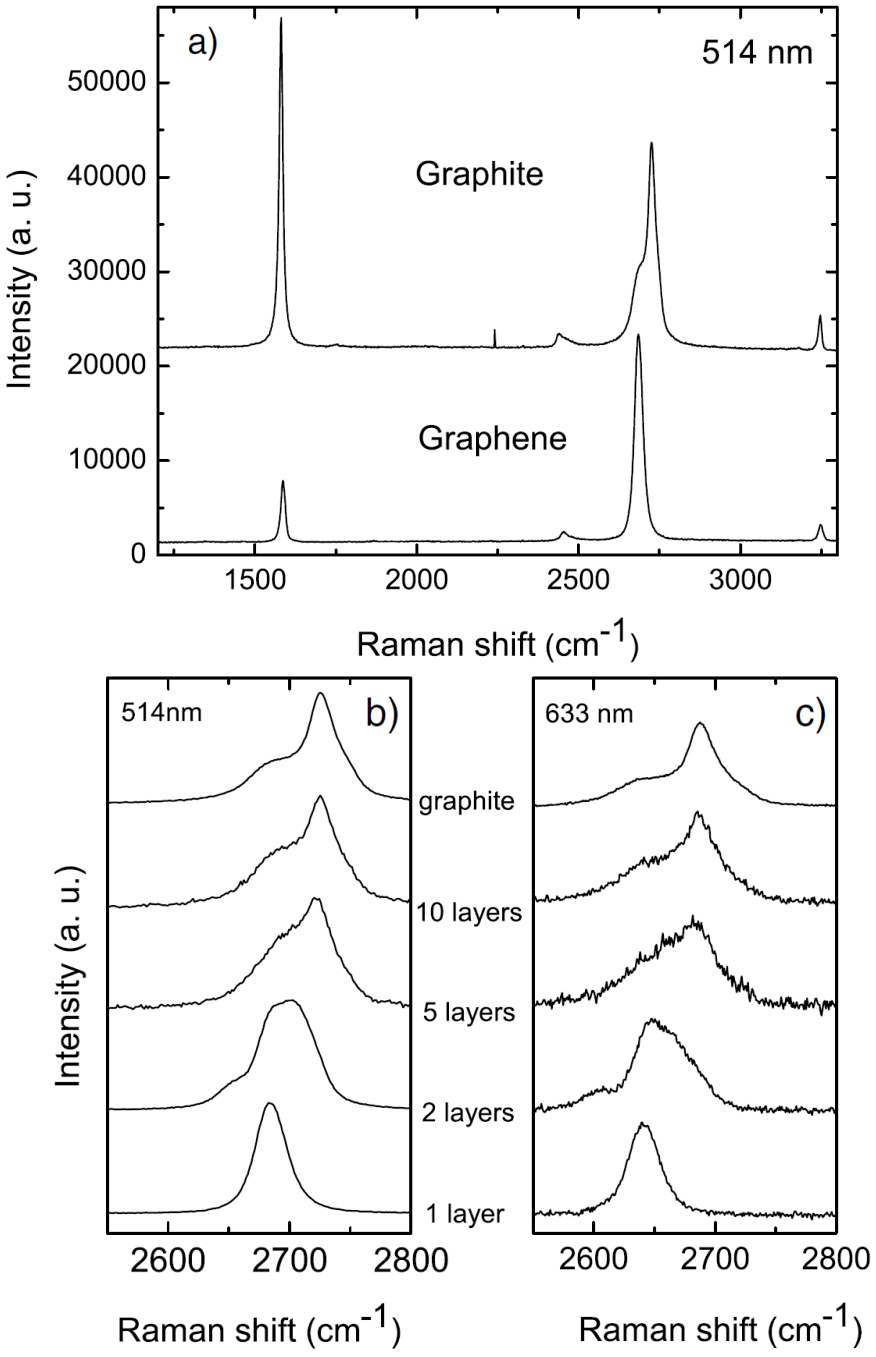


**Figure 3.8** a) A comparison between the Raman spectra of graphite and graphene at 514 nm. The evolution of 2D peak with the number of layers in graphene, when incident with a laser beam of b) 514 nm and c) 633 nm (illustration taken from [7]).

# 4 Device Fabrication and Experimental Setup

This chapter describes the specific steps involved in making graphene-SAW devices, from transferring graphene onto lithium niobate to the fabrication of gold contacts for electrical measurement. The first section illustrates the transfer technique used to transfer large-area CVD graphene from copper to arbitrary substrates. In section 4.2, the characterisation techniques used for the identification of single-layer graphene and impurities, in the form of etchant salt or PMMA residues coming from the graphene transfer process, are described. After characterisation, gold contacts are fabricated using electron-beam lithography process, discussed in section 4.3. The device fabrication was followed by mounting the sample on a printed circuit board (PCB) and wire-bonding with gold wires, which is described in section 4.4. In section 4.5, the use of an ion-gel solution for introducing charge carriers in graphene through the top gate is described. A summary of all the devices fabricated during the experiments is given in section 4.6. The experiments are performed by exciting the transducers with the radio frequency (RF) waves to generate SAWs which gives rise to an acoustoelectric current in graphene. The change in amplitude and velocity of the SAW was measured using an oscilloscope. The details of the measurement setup used are discussed in Section 4.7. A bare lithium niobate sample, without any graphene transferred, was measured to check the effect of pressure and temperature on it. It is further used to measure the velocity of SAWs and establish the absence of acoustoelectric current in lithium niobate, as discussed in section 4.8.

## 4.1 Graphene Transfer Process

The most convenient and cost-effective method to produce large-area graphene is chemical vapor deposition on copper substrates. CVD graphene is widely used for research purposes and is easily available commercially. In the experiments described in this work, a single-layer CVD graphene grown on copper (from Graphene Supermarket) was used. The single-layer graphene is transferred onto lithium niobate substrates using a standard polymethyl methacrylate (PMMA) transfer technique, originally developed by Ruoff's group [111]. PMMA is a thermoplastic polymer, commonly used as a positive resist in microlithographic processes. In this graphene transfer process, PMMA is used as a protective layer on top of graphene, which also permits its easier handling. The standard PMMA solutions used for this purpose are PMMA 495K and PMMA 950K, where 495K and 950K describes their molecular weight. It can be deposited on a substrate using a spinner, the thickness of PMMA being dictated by its molecular weight (generally, a resist with higher molecular weight is thicker), the rate of revolution of the spinner and the time for which it is spun. A PMMA 950K A4 solution, which is PMMA 950K dissolved in anisole in the ratio 2:1, is used to deposit a 100 nm thick layer on a 5 mm $\times$ 5 mm piece, cut from a $2'' \times 2''$ sheet, of CVD graphene grown on copper. The spinner is operated at 3500 rpm for 50 s, which includes the total ramping up and down time of 5 s, and 45 s for which it was held constant. After spinning, the sample is baked at 180 °C for 8 minutes on a hot plate. The baking temperature is kept slightly above the melting point of PMMA (160 °C) to allow it to melt, recrystallise and arrange itself according to the corrugations in the substrate. This ensures better contact with graphene, necessary for its homogenous transfer. The layer of PMMA protects graphene on one side of Cu, the other side (with no PMMA) is etched in a reactive ion-etcher using argon (Ar) plasma. An etching recipe of plasma with power 10 W, Ar supply 8 sccm (standard cubic centimeters per minute) at 20 s is used for etching single-layer graphene. This process is repeated twice to ensure the removal of any graphene layer on the non-coated side of the copper. This copper foil with PMMA on top was placed on the meniscus of a liquid etchant, which etches the copper from underneath. Both ferric chloride and ammonium persulfate were tried as copper

etchants, the latter of which was found to leave fewer residues on the substrate. A 0.2 M solution of ammonium persulfate was used to etch the copper for 8 hours; a solution with higher concentration was found to be possible to use for faster etching but it tended to leave more etchant residues. After the copper is completely dissolved in etchant, a thin transparent layer of PMMA with graphene floats on the surface of the etchant, which was then scooped out using a glass spoon to rinse in distilled water. The rinsing process was repeated several times to reduce the etchant residues. This layer of PMMA with graphene was initially transferred to $Si/SiO_2$ substrates to test the transfer process, but later was transferred directly on lithium niobate and quartz. The layer of PMMA with graphene was dried in atmosphere to allow the distilled water between graphene and the substrate to squeeze out slowly, which ensures better contact between them. Once it was dry, the PMMA layer on top was removed by acetone.

### 4.1.1 Etching Chemicals

A layer of PMMA can ideally be dissolved in acetone, however attempts to dissolve PMMA on graphene left significant residues on the surface of the sample. These residues can arise either from the etchant solution or the PMMA. We found that dissolving the PMMA layer in chloroform followed by washing in acetone or just boiling in acetone itself at 80 °C gave much more homogenous transfer and significantly less PMMA residues as shown in Figure 4.1(b). This was significantly better than cleaning in acetone at room temperature, which gives a non-homogenous transfer of graphene with a lot of residues, wrinkles and cracks in the sample (see Figure 4.1(a)). The few residues present are thought to have come from the etchant solution. The images from the microscope in Figure 4.1 illustrates the difference between the surface of the transferred graphene in each case. This homogenous graphene transfer technique as tested on silicon substrate was applied to lithium niobate. As described in Section 3.4, the optical contrast difference between graphene and the substrate plays an important role in preliminary identification of graphene. It is easier to view graphene on $Si/SiO_2$ rather than on lithium niobate because of the discernable contrast between graphene and $Si/SiO_2$ under an optical microscope: since lithium niobate

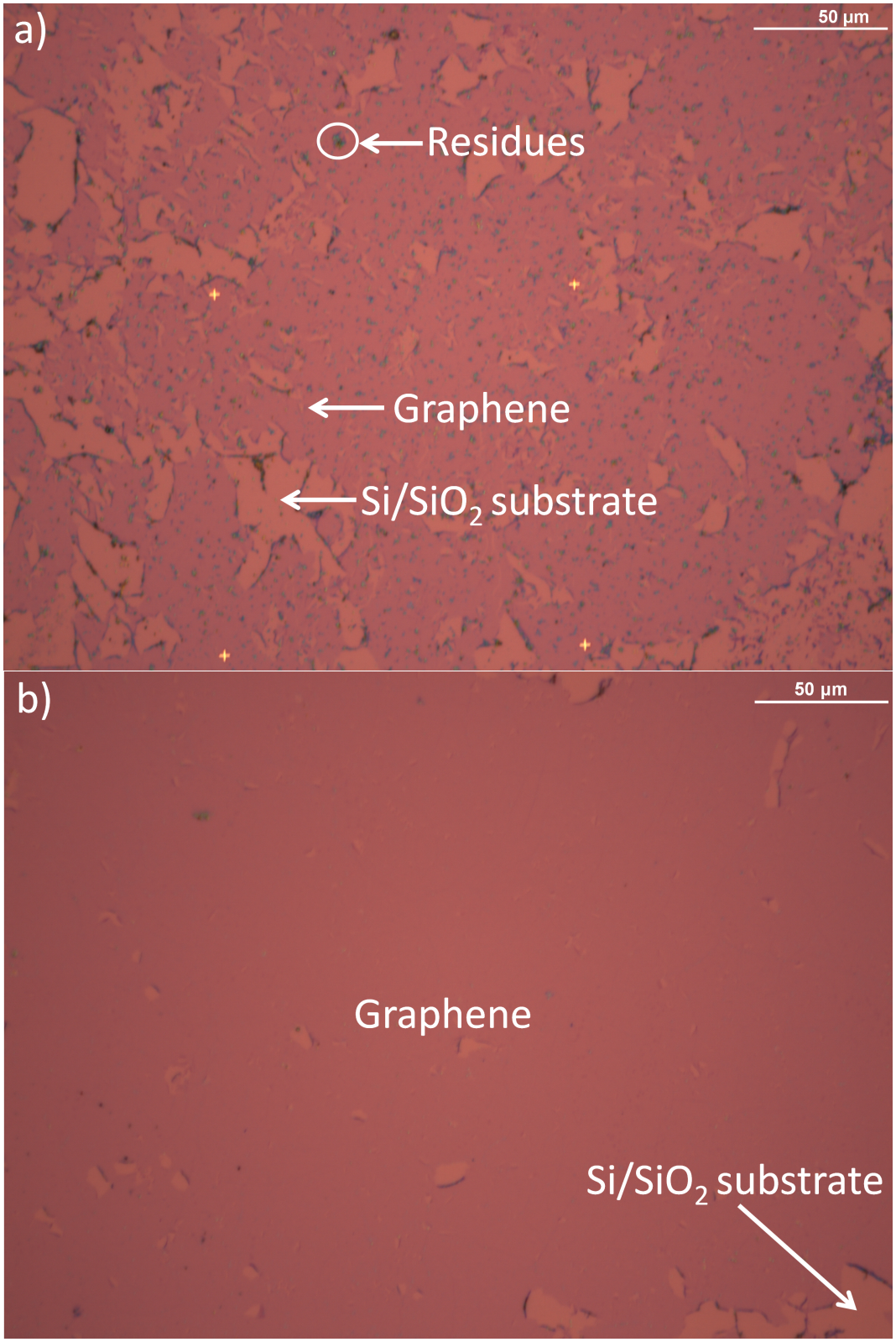


**Figure 4.1** Different solutions can be used to wash the PMMA layer from the substrate. Optical microscope images showing the difference between PMMA being washed in a) acetone at room temperature for 30 minutes and b) chloroform followed by boiling acetone for 30 minutes in each.

is transparent, no such contrast is available to clearly differentiate graphene with lithium niobate as shown in Figure 4.2, where a green filter was used to aid visibility. The techniques used for identifying the sources of residues, and characterisation of graphene are discussed in the following section.

## 4.2 Characterisation

### 4.2.1 Energy Dispersive Spectroscopy

Energy Dispersive Spectroscopy (EDS) was used to determine the source of contaminating residues in our samples. The images of the samples revealed a roughly even distribution of predominantly greenish-blue residues (see Figure 4.1(a)). The sample fabrication technique meant that the only sources of these contaminants could be the etchant solution, unetched copper and the PMMA. EDS, a widely used elemental analysis technique in scanning electron microscopy (SEM), is employed to help determine the source of residues. In this process, the surface of the sample is exposed to a highly-focused beam of electrons, which interacts with the electrons of the sample, and excites them from their ground states. The vacancy created by this excitation, is filled by electrons from higher energy levels. This process causes the emission of an X-ray equivalent to the difference of the energy levels involved. Since each element has a unique atomic structure, the emitted X-rays uniquely identifies the element under study. Areas showing a particularly high density of contaminants are scanned and the typical results obtained are shown in Figure 4.3. The statistical analysis of the results shows a very low percentage of copper (Cu), iron (Fe), and chlorine (Cl). A high percentage of silicon (Si) and oxygen (O) are expected from the $Si/SiO_2$ substrate whereas graphene or PMMA could act as the carbon (C) source. Since the etchant solution contains traces of Fe and Cl, a relatively low percentage shows that the etchant residues are not the major source of contaminants. Also, negligible amounts of Cu indicate that little un-etched Cu remains on the sample. Therefore, the residues are believed to originate from the PMMA, and more emphasis was put on refining the cleaning mechanisms to reduce the PMMA residues, for example, different etching chemicals were

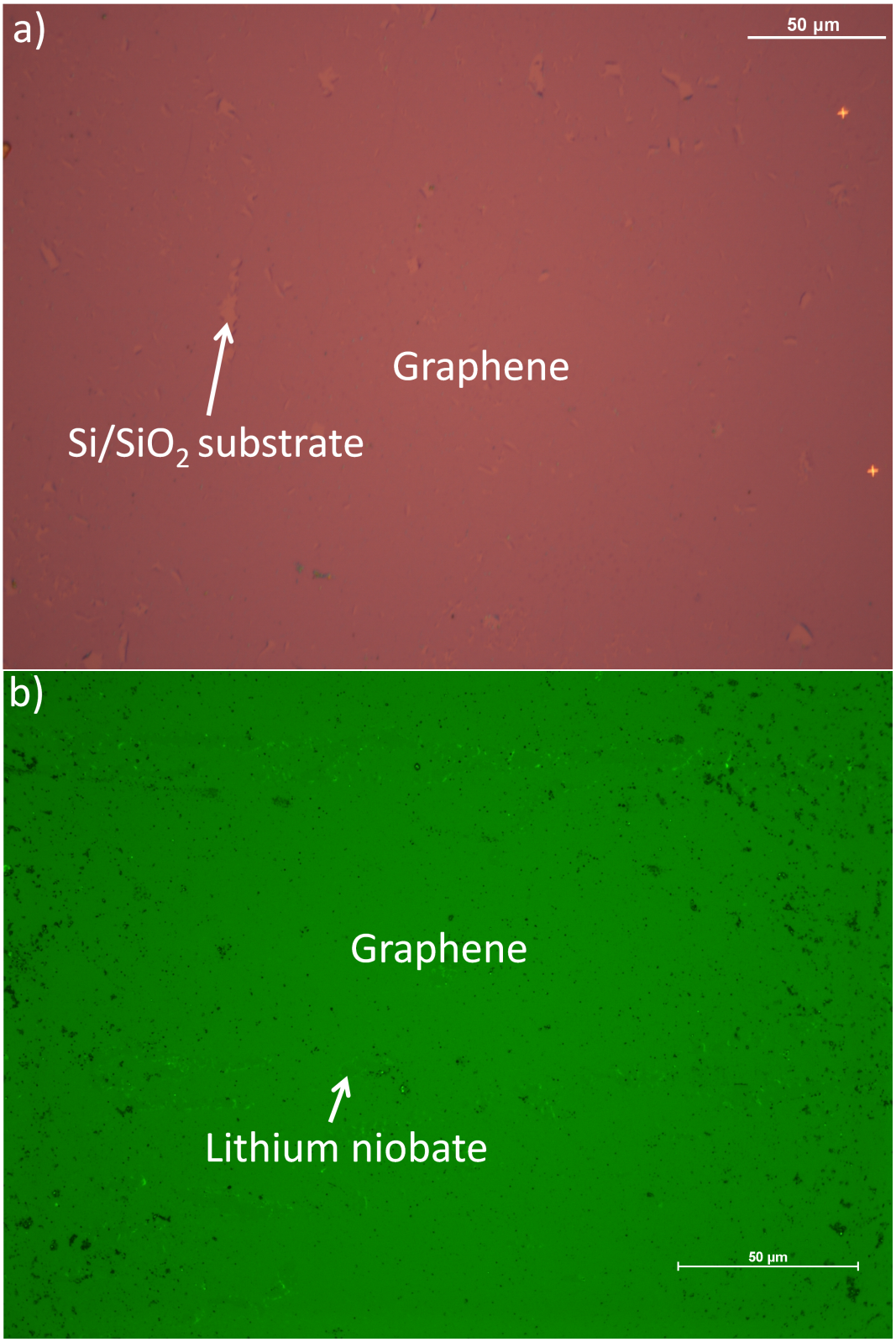


**Figure 4.2** Optical microscope images of the contrast difference given by transferred CVD graphene on a) $Si/SiO_2$ and b) lithium niobate substrate.

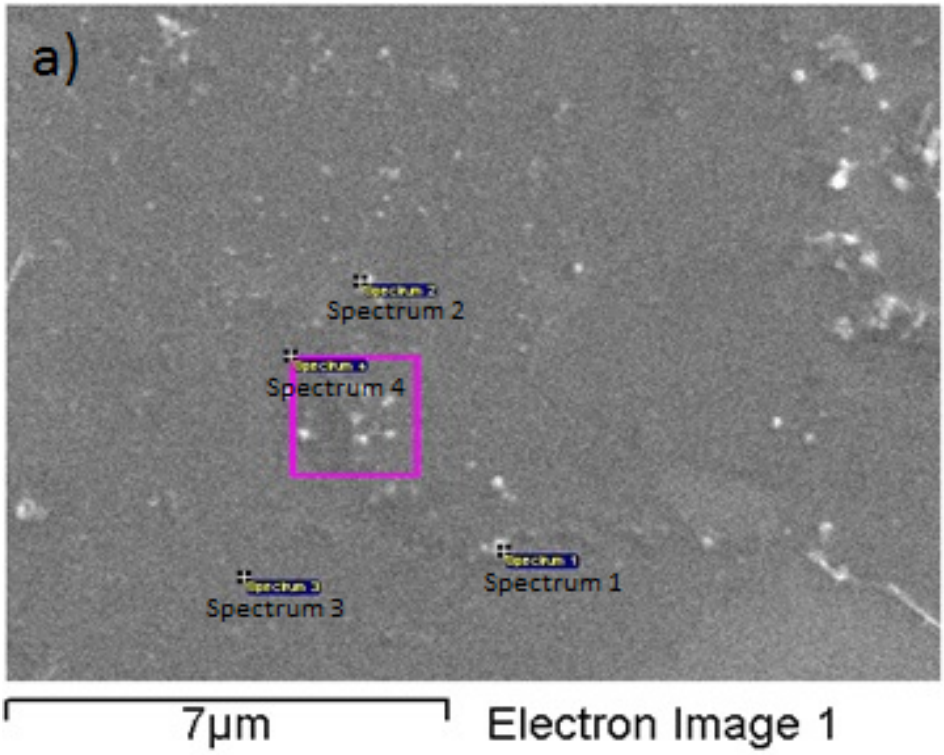


b)

Processing option : All elements analysed (Normalised)

| Spectrum | In stats. | C | O | Mg | Si | Cl | Cr | Fe | Cu | Sn |
|---|---|---|---|---|---|---|---|---|---|---|
| Spectrum 1 | Yes | 5.52 | 35.95 | 0.03 | 58.28 | 0 | 0.19 | 0.02 | -0.02 | 0.05 |
| Spectrum 2 | Yes | 6.71 | 33.32 | 0.02 | 59.9 | -0.01 | 0 | 0 | -0.01 | 0.07 |
| Spectrum 3 | Yes | 5.13 | 33.43 | 0 | 61.37 | 0.01 | 0.01 | 0.03 | -0.03 | 0.06 |
| Spectrum 4 | Yes | 0.9 | 34.28 | 0.01 | 64.78 | 0.02 | 0.02 | 0.02 | 0 | 0.06 |
| | | | | | | | | | | |
| Mean | | 4.56 | 34.24 | 0.01 | 61.08 | -0.01 | 0.05 | 0.02 | -0.02 | 0.06 |
| Std. deviation | | 2.54 | 1.21 | 0.01 | 2.77 | 0.02 | 0.09 | 0.01 | 0.01 | 0.01 |
| Max. | | 6.71 | 35.95 | 0.03 | 64.78 | 0.01 | 0.19 | 0.03 | 0 | 0.07 |
| Min. | | 0.9 | 33.32 | 0 | 58.28 | -0.05 | 0 | 0 | -0.03 | 0.05 |

**Figure 4.3** a) The SEM image of the EDS analysis of graphene transferred on $Si/SiO_2$ substrate. b) The elemental concentration of the residues in different regions.

tried as discussed in the previous section.

### 4.2.2 Raman Spectroscopy

Raman spectroscopy, described in section 3.4.2, is generally used as a non-destructive method for the identification of graphene layers. The Raman active nodes in pristine graphene can be found at a Raman shift of 1350 $cm^{-1}$ (D band), 1580 $cm^{-1}$ (G band) and 2700 $cm^{-1}$ (2D band). A Renishaw continuous wave (CW) 532 nm laser source is used to excite the sample and the emitted light is collected through a lens and sent through a spectrophotometer, where interference notch filters separates the weak Raman signal from the Rayleigh signal. The response is observed in the Raman-active region of graphene *i.e.* in the range 1200-3000 $cm^{-1}$ as shown in Figure 4.4.

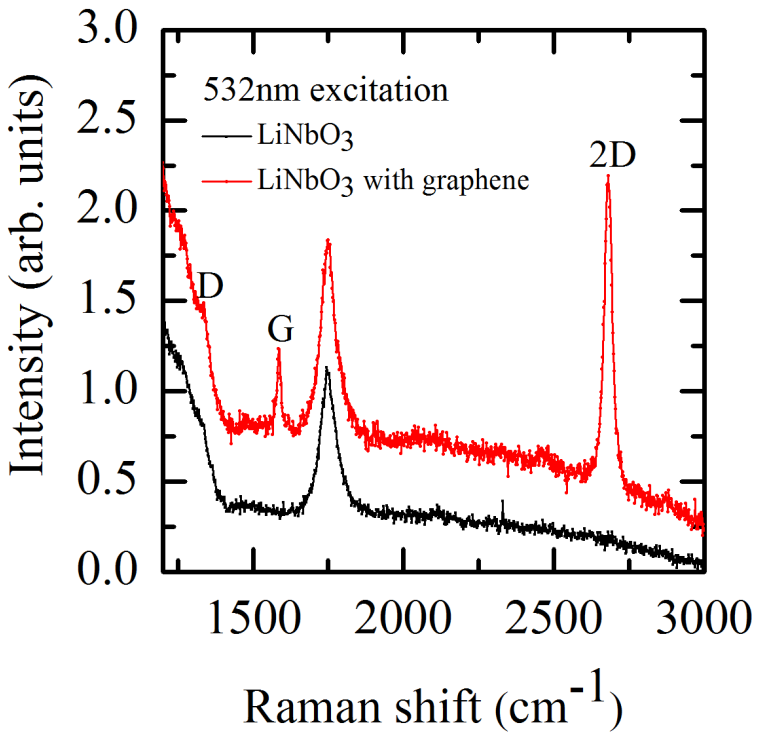


**Figure 4.4** Raman spectra of bare lithium niobate (black) and graphene transferred on it (red). The intensity axis is shifted to show the difference between the two spectra.

The Raman spectra of bare lithium niobate is obtained first and used as a control for further analysis. As graphene on lithium niobate is invisible even under the microscope, the Raman spectrum is measured at randomly distributed points on the sample. This is done on each sample for the characterisation of graphene. The average Raman spectra of

25 such random points on one of the samples is shown in Figure 4.4 and is compared to the bare lithium niobate substrate. The D, G, and 2D peaks are obtained at 1337 $cm^{-1}$, 1585 $cm^{-1}$, and 2680 $cm^{-1}$ respectively, with an average 2D/G peak ratio of 3.5. The peak observed at 1750 $cm^{-1}$ is a characteristic of lithium niobate as is evident from its comparison with the bare sample. The y-axis in Figure 4.4 represents the intensity of the emitted light, which is normalised to illustrate the ratio of Raman peaks. The slight shift in Raman peaks from the expected positions could be attributed to the unintentional doping introduced by the graphene transfer process. However, the measured 2D/G peak ratio is characteristic of single-layer graphene [7] and the comparatively small D peak also suggests that the transferred graphene is relatively uniform and defect-free.

## 4.3 Gold Contacts

### 4.3.1 Electron Beam Lithography

After the characterisation, the metallic contacts are defined on graphene using e-beam (electron-beam) lithography, which is a nano-lithographic process that can be used to create extremely small patterns (down to 50 nm) on a substrate. The principle of e-beam lithography is similar to optical lithography, where a thick layer of resist is deposited on the substrate and exposed to an electron beam instead of light. An exposure to the electron beam changes the chemical composition of the resist. When the resist in use is positive (negative), the exposed (unexposed) area of the substrate can be removed by immersing it in a 'developer' solution. A developer solution is specific to the type of resist used. This process leaves the desired pattern on the substrate in the form of trenches between the resist. A thin layer of metal is deposited in these trenches, which sticks to the substrate whereas the deposition on the resist can be removed in a lift-off process. The lift-off process refers to the dissolving of the resist in an aggressive solvent, therefore removing the metal deposited on it too. As a result, the desired pattern with metallic contacts is obtained on the substrate. The lithographic process used to fabricate metal contacts on devices described in this work are as follows: A 300 nm thick layer of PMMA

495K A6 is spun over the graphene transferred onto lithium niobate and baked at 180 °C for 8 minutes. In addition to the PMMA layer, which is suitable for e-beam lithography on $Si/SiO_2$, an extra layer of aluminum is required on lithium niobate. The insulating nature of lithium niobate causes charge build up on the surface when encountered by high-energy electrons of the e-beam, reflecting further the incoming electrons and making it difficult to focus on the substrate. To prevent this, the PMMA is covered with a 12 nm thick layer of Al to make the surface conducting. The sample is then loaded in the electron microscope using silver paint, taking care to run up to the sides to touch the top of the substrate with aluminum. This prevents any charge build up on the surface during the electron beam lithography. AutoCAD Design software is used to design four contacts, each 20 $\mu$m thick, separated by several hundred micrometers. A schematic of the device layout designed in AutoCAD is shown in Figure 4.5.

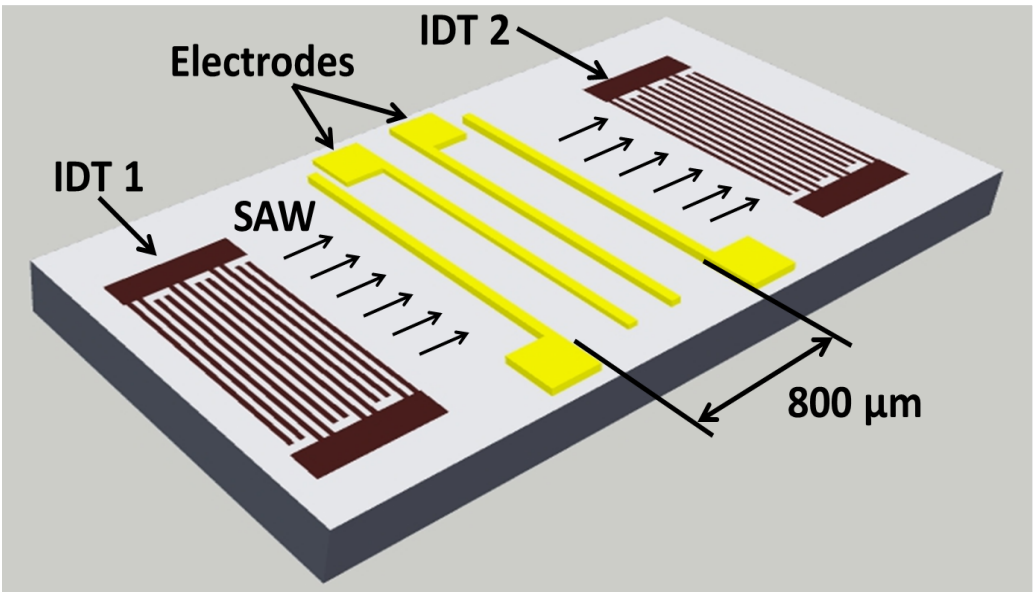


**Figure 4.5** A schematic of a bare lithium niobate device showing the transducers and electrodes, which were used to measure the amplitude and velocity of the SAW, and the generated acoustoelectric current, respectively.

This AutoCAD design is used to determine the electron beam dose (number of electrons emitted per unit square per sec) required for writing the pattern. The sample is exposed to a high energy beam of electrons at the desired regions on the substrate. After the e-beam exposure, the aluminum is removed by immersing in 5 ml metal ion free (MIF)

solution for 2 minutes, followed by thoroughly rinsing in distilled water, and drying. A developer solution is prepared by mixing 1 part of methyl ethyl ketone (MEK), 5 parts of methyl iso-butyl ketone (MIBK), and 15 parts of iso-propyl alcohol (IPA). The sample is immersed in the developer for 15 s, then rinsed in IPA, and dried. The developed pattern is checked under the optical microscope and loaded in the thermal evaporator for metal deposition. A schematic of the lithography process involved is shown in Figure 4.6.

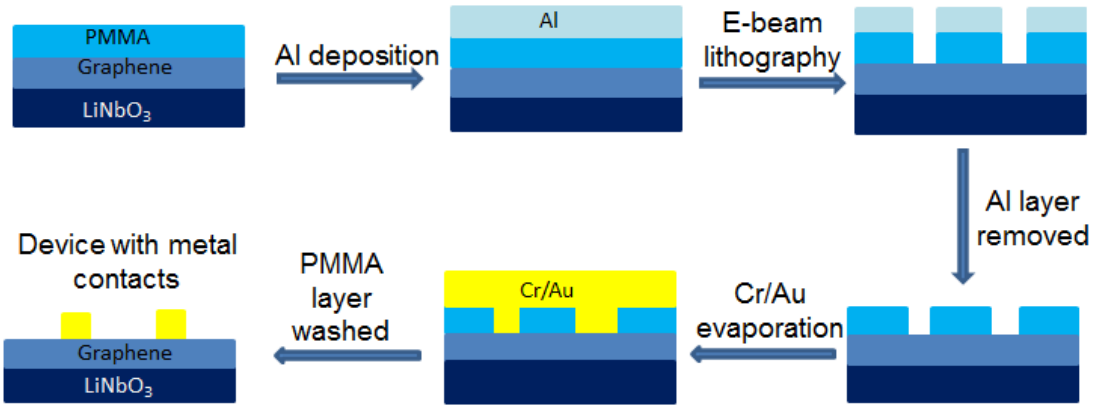


**Figure 4.6** An illustration of the steps involved in the e-beam lithography process for the fabrication of metal contacts on devices.

### 4.3.2 Metallisation

A thermal evaporator is used for depositing thin-films of aluminum (Al), chromium (Cr) and gold (Au) on the sample, each at different stages of the device fabrication process. The thermal evaporation is done in a vacuum chamber with pressure $\approx 1.5 \times 10^{-6}$ mbar, where the desired metal is heated in a carrier boat, made of tungsten or molybdenum. The metal is evaporated and the vapors get condensed on the substrate depositing a thin layer of metal on it. The rate of deposition can be controlled by the amount of current passing through the carrier boats. The rate of thin-film deposition is maintained close to 1 $Å s^{-1}$ for both Al and Cr/Au deposition. The metallic contacts used for Ohmic measurements are made by evaporating 7 nm of Cr, followed by 70 nm of Au. The evaporation of a small amount of Cr before Au acts as a binder to stick the Au to the substrate. The excess of Cr/Au deposited on the PMMA is removed by dissolving the PMMA in acetone. The sample is rinsed first in fresh acetone, and then in IPA before blow drying with nitrogen.

## 4.4 Sample Mounting

### 4.4.1 Mounting, Bonding and Gold Electroplating

In order to measure the acoustoelectric current in graphene, it is necessary to connect the metallic contacts fabricated on the sample to the printed circuit board (PCB). A PCB is specifically designed for this purpose, and is prepared using optical lithography. Sharp edges are minimised in the circuit design to mitigate RF losses. To make the wire-bonding possible on the PCB, its surface is electroplated with approximately 1 $\mu$m gold over small areas. A commercial gold electroplating kit, available at Intertronics, is used for this purpose. For the electroplating process, the cathode of a 100 mA current source is connected to the plating area, and the anode to the electroplating pen, respectively. When the electroplating pen touches the plating area, the circuit completes, and the metal ions from the solution deposits on the cathode. Prior to gold electroplating, the PCB is brushed clean, and masked with Kapton tape to expose only the areas to be electroplated. The plating area is further cleaned using a degreaser to remove any oil or grease and is thoroughly rinsed in distilled water. This is followed by gold deposition by connecting the gold electroplating pen to a 6 V power supply and gently rubbing over the area to be plated, until it turns from bright to dull-golden in colour. It is then rinsed in distilled water and dried, which is the final step before bonding to the metallic contacts fabricated on the sample. The sample is mounted on PCB using a silver epoxy (Circuitworks CW2400 epoxy), which is a mixture of two silver solutions, epoxy and hardener, both mixed in the ratio 1:1. After mounting the sample, the epoxy is hardened by heating at 110 °C for 10 minutes. This epoxy is found to be a stronger adhesive than silver colloidal solution, which is generally used as a conducting glue for sticking samples. This method of device fabrication and adhesion to a custom PCB negates the need for costly, multi-pin sample packages used for sticking and bonding to the sample. The metal contacts in graphene are connected to the PCB using a wire-bonding machine, which melts the gold wire with an ultrasonic pulse and bonds it to the sample. The sample was kept at 90 °C to keep the sample warm, which helps in wire-bonding. Making secure gold bonds to the metallic

contacts defined on graphene proved highly challenging. The graphene layer between the substrate and metal contacts prevents metal-substrate linkage, and the metal itself does not adhere well to graphene. Therefore, when pressed by the wedge-shaped tip of the bonding machine, it damages the contact. In subsequent samples, the contact pads are positioned outside the area of graphene to prevent this damage. An image of a typical device after mounting and bonding the sample on the PCB is shown in Figure 4.7.

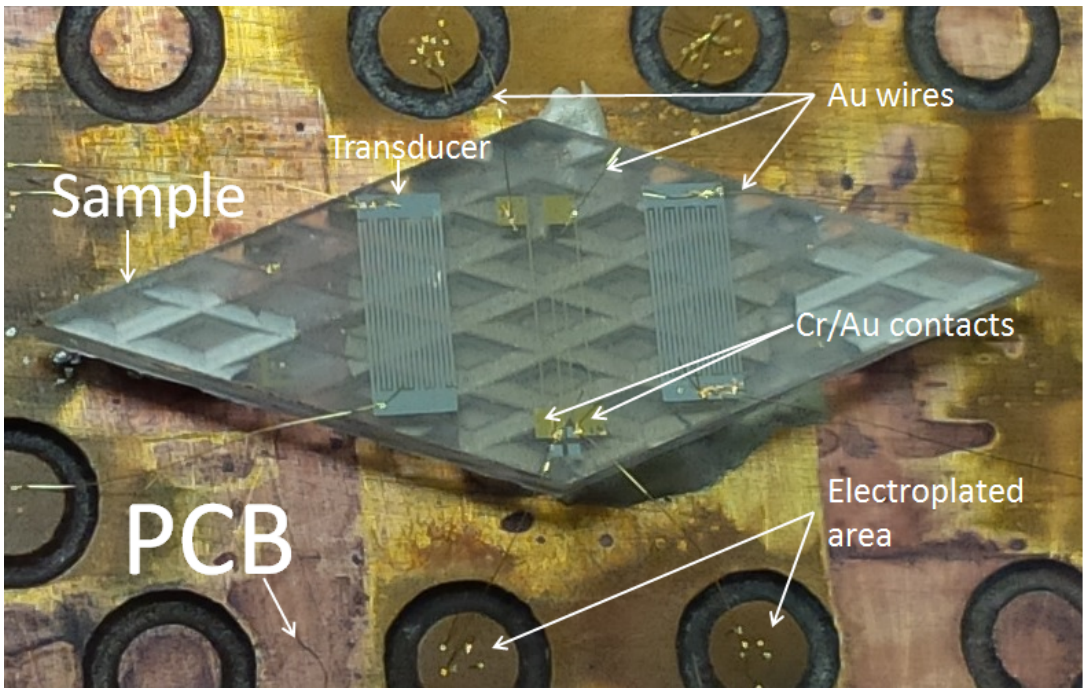


**Figure 4.7** An optical image of a typical device mounted on a PCB, where its metallic contacts are wire-bonded to the electroplated areas on the PCB.

## 4.5 Gate Fabrication

The resistance modulation in graphene is achieved by fabricating a top gate using an ion-gel as the dielectric. Any metal contact on the surface of the sample, which is disconnected from the graphene, source and drain contacts can be used as a gate in this configuration. The ion-gel is prepared by dissolving 8 parts of ploy ethyl oxide (PEO) with 1 part of lithium perchlorate in methanol *i.e.* 0.2 g of PEO and 0.024 g of lithium perchlorate dissolved in 10 ml of methanol [119]. The solution is put in ultra-sonication for about 5-10 minutes, followed by heating up at 80-90 °C for 5-10 minutes while stirring the sample to

thoroughly dissolve the suspension. This is followed by centrifuging the solution at 10,000 rpm for 5 minutes to sediment the heavy polymers, and the clear solution, which would form the gate dielectric, is extracted from the top. A small amount of this solution is carefully dropped over the metal contacts in graphene such that it covers the entire area to be gated. The final step in this process is to cure it at 110 °C for 5 minutes to evaporate any excess methanol, which leaves a gel-like dielectric.

## 4.6 Fabricated Devices

The devices used for the experimental work presented in this thesis are a result of a well-refined device fabrication process, developed by testing over several samples. However, all the experiments presented in this thesis were performed on devices given in Table 4.1.

## 4.7 Experimental Setup

### 4.7.1 Generation and Detection of SAWs

The sample prepared from the fabrication process is mounted in a small vacuum chamber and evacuated to a pressure of $3.6 \times 10^{-6}$ mbar for electrical measurements. A schematic of the experimental set up involved in the measurement of acoustoelectric current at room and low temperature is shown in Figure 4.8. A pulse of width 1 $\mu$s and amplitude 5 V, at a frequency of 1 kHz is obtained using a pulse signal generator. This pulse is used to modulate the output of an Agilent RF signal generator with a maximum amplitude of 20 dBm, where dBm is the power ratio, measured in decibels (dB), of the measured power with reference to 1 mW. A modulated pulse is used to determine the velocity and the propagation duration in the lithium niobate SAW delay lines whereas a continuous wave directly from the RF signal generator is used for acoustoelectric measurements. The RF signal is passed to the sample through the connectors soldered to the PCB and the inter-digital transducers on the sample converts it to generate a SAW at definite RF frequencies.

Table 4.1 : List of all the devices measured and described in this work.

| Sample | Substrate | Graphene | Electrodes | Purpose |
|---|---|---|---|---|
| Blank device | Lithium niobate | No | 800 $\mu$m | Used to measure the transducer response and velocity of the SAW. |
| Device1 | Lithium niobate | Yes | 200 $\mu$m 300 $\mu$m 500 $\mu$m | Sheet resistance $\approx$ 60 k$\Omega/\square$. Used for the acoustoelectric measurement at room and low temperature. |
| Device2 | Lithium niobate | Yes | 200 $\mu$m 300 $\mu$m 500 $\mu$m | Sheet resistance $\approx$ 275 k$\Omega/\square$. Used for the same purpose as Device1 |
| Device3 | Lithium niobate | Yes | 200 $\mu$m 300 $\mu$m 500 $\mu$m | Sheet resistances $\approx$ 8-10 M$\Omega/\square$. Used for the acoustoelectric measurement at room temperature. |
| DeviceG1 | Lithium niobate | Yes | 300 $\mu$m | Used to study acoustoelectric current as a function of gate voltage. |
| DeviceG2 | Lithium niobate | Yes | 300 $\mu$m | Used to study acoustoelectric current as a function of gate voltage. |
| DeviceG3 | Lithium niobate | Yes | 300 $\mu$m | Used to study acoustoelectric current as a function of gate voltage. |

**Table 4.1** List of all the devices measured and described in this work.

The emitted SAW travels on the surface of lithium niobate in both directions perpendicular to the transducer. The SAW traveling towards the output transducer interacts with the graphene transferred between them. The change in amplitude and velocity of the SAW due to this interaction is measured using a 2 GHz LeCroy oscilloscope connected to the output transducer.

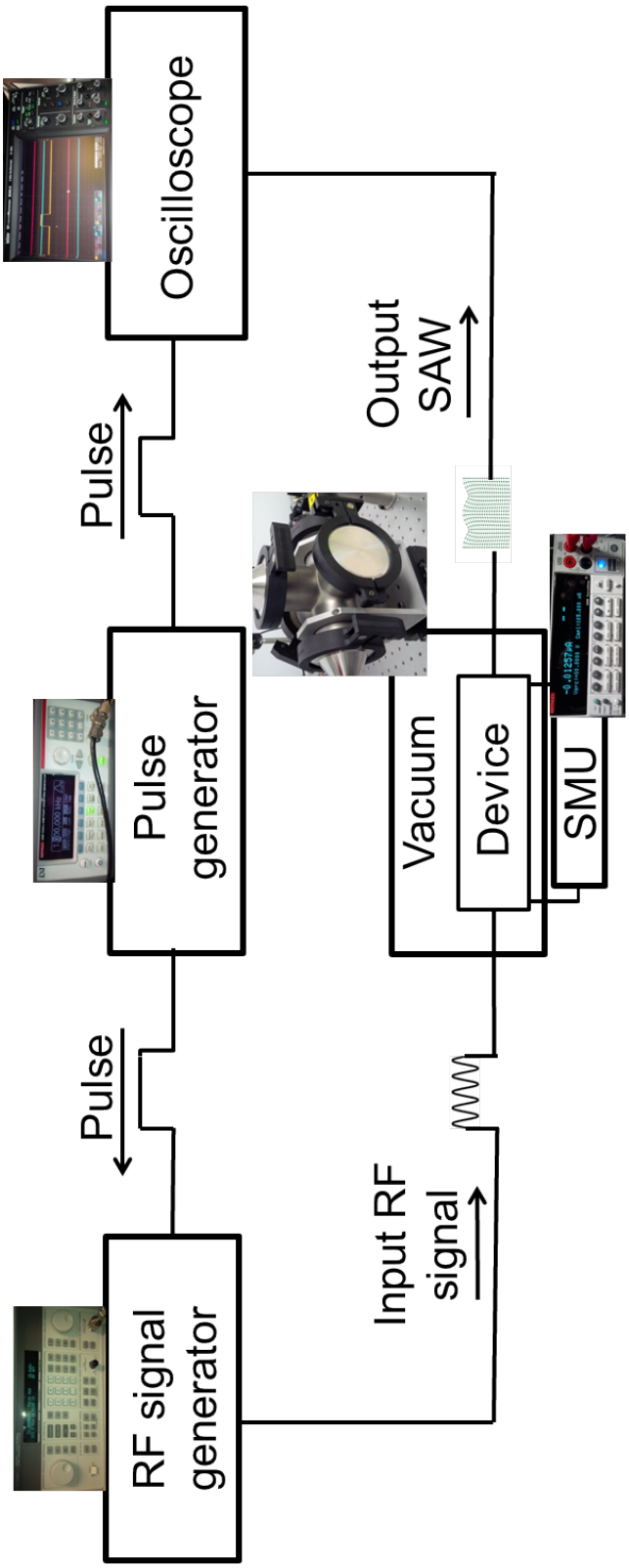


**Figure 4.8** A schematic of the experimental setup used during the measurements.

### 4.7.2 Estimation of SAW Intensity

The SAW amplitude measured by the oscilloscope is the resultant amplitude after transmission loss form the two input and output transducers and attenuation caused by the medium. The actual intensity of SAWs at the center of substrate was estimated based on the following assumptions:

1. The energy loss due to the attenuation of SAWs while traveling in the substrate is negligible compared to the transmission loss by the transducers.

2. Both the input and output transducers have same transmission factor $x$ such that for input Power $P_0$, the input transducer transmits SAWs equally in both the direction perpendicular to the transducer along the substrate surface with intensity equal to $xP_0/2$.

Hence, the intensity $I$ at the center of the substrate is given by

$$I = xP_0/2 \tag{4.1}$$

which undergoes further transmission loss at the output transducer. Using the same transmission factor $x$, the intensity measured at the output is given by

$$P_{out} = x.xP_0/2 \tag{4.2}$$

We know that

$$\frac{P_{out}}{P_0} = \left(\frac{V_{out}}{V_0}\right)^2 \tag{4.3}$$

From 4.2 and 4.3, the intensity encountered by graphene at the center of the substrate can be given by

$$I = \sqrt{2}\frac{V_{out}}{V_0}\frac{P_0}{2} \tag{4.4}$$

$V_{out}$ is the output peak to peak voltage measured for an input RF power of 20 dBm, which is equivalent to a peak to peak voltage of $V_0$=6.364 V. It was assumed that for any arbitrary input voltage, the ratio of the output measured and input voltage is the same as $V_{out}/V_0$. The measurements performed at 18 and 19 dBm RF power concurs with the assumption.

Hence, for any arbitrary input power $P_{in}$, the SAW intensity encountered by graphene is given by

$$I = \sqrt{2}\frac{V_{out}}{V_0}\frac{P_{in}}{2} \tag{4.5}$$

### 4.7.3 Measurement of Acoustoelectric Current

The metal contacts fabricated on graphene are used to measure the conductivity of graphene as well as the acoustoelectric current in it. A Keithley 2400 sourcemeter is used for this purpose. No bias is applied during the measurement of acoustoelectric current. The conductivity is measured through the current-voltage (I-V) characteristics obtained by sweeping the current from -30 $\mu A$ to 30 $\mu A$. The sourcing of higher current could potentially break the device, therefore it is avoided during the I-V measurements.

### 4.7.4 Close-cycle Cryostat

The low temperature measurements are performed in a Lakeshore compressed liquid helium close-cycle cryostat, with liquid helium as a refrigerant. The temperature of the cryostat is regulated using a temperature controller, where a minimum temperature of 10 K could be attained. The cryostat was modified to accommodate the device, along with the RF and Fischer connectors to perform the measurements. The actual temperature on the PCB is measured using a Si-diode sensor mounted on it, and owing to the poor thermal coupling between the PCB and the sample holder of the cryostat, a minimum of 48

K was attained. Therefore, the measurement of the acoustoelectric current as a function of temperature in the cryostat was possible only in the range 48-300 K.

## 4.8 Bare Lithium Niobate

The experiments conducted in this work has been performed on a commercially available (from MESL Microwave) piezoelectric substrate, 128° Y-X lithium niobate, which comes with two double finger inter-digital transducers (IDTs) fabricated on its surface. The separation between the two transducers of width 3.5 mm was measured to be 3.5 mm. A bare lithium niobate device, without any graphene on it, is fabricated to measure the amplitude and velocity of SAW at low pressure and in the presence of metallic contacts in its acoustic beam path. The metallic contacts of size 20 $\mu$m $\times$ 3.5 mm each, identical to the one in graphene-SAW devices, are fabricated to establish that the acoustoelectric effect observed in graphene-SAW devices is due to the interaction of graphene carriers with SAWs and not an inherent phenomenon in lithium niobate. SAWs are generated by exciting one of the transducers with the RF waves coming from the RF signal generator and measured using an oscilloscope at the other transducer. The SAW amplitude is measured at the same conditions of temperature and pressure that is used in the acoustoelectric measurement of graphene-SAW devices, including the low temperature measurement in the range (48-296 K). The velocity of the SAW is determined by measuring the time taken by the SAW in traversing the distance between the two transducers. Any acoustoelectric current carried by the SAWs on the piezoelectric substrate (lithium niobate) is measured through the gold contacts fabricated in the acoustic beam path.

### 4.8.1 SAW Amplitude

The amplitude of the SAWs generated in lithium niobate is measured in an oscilloscope and plotted as a function of frequency, in the range 1-500 MHz, at room temperature and atmospheric pressure, as shown in Figure 4.9(a). The double finger inter-digital

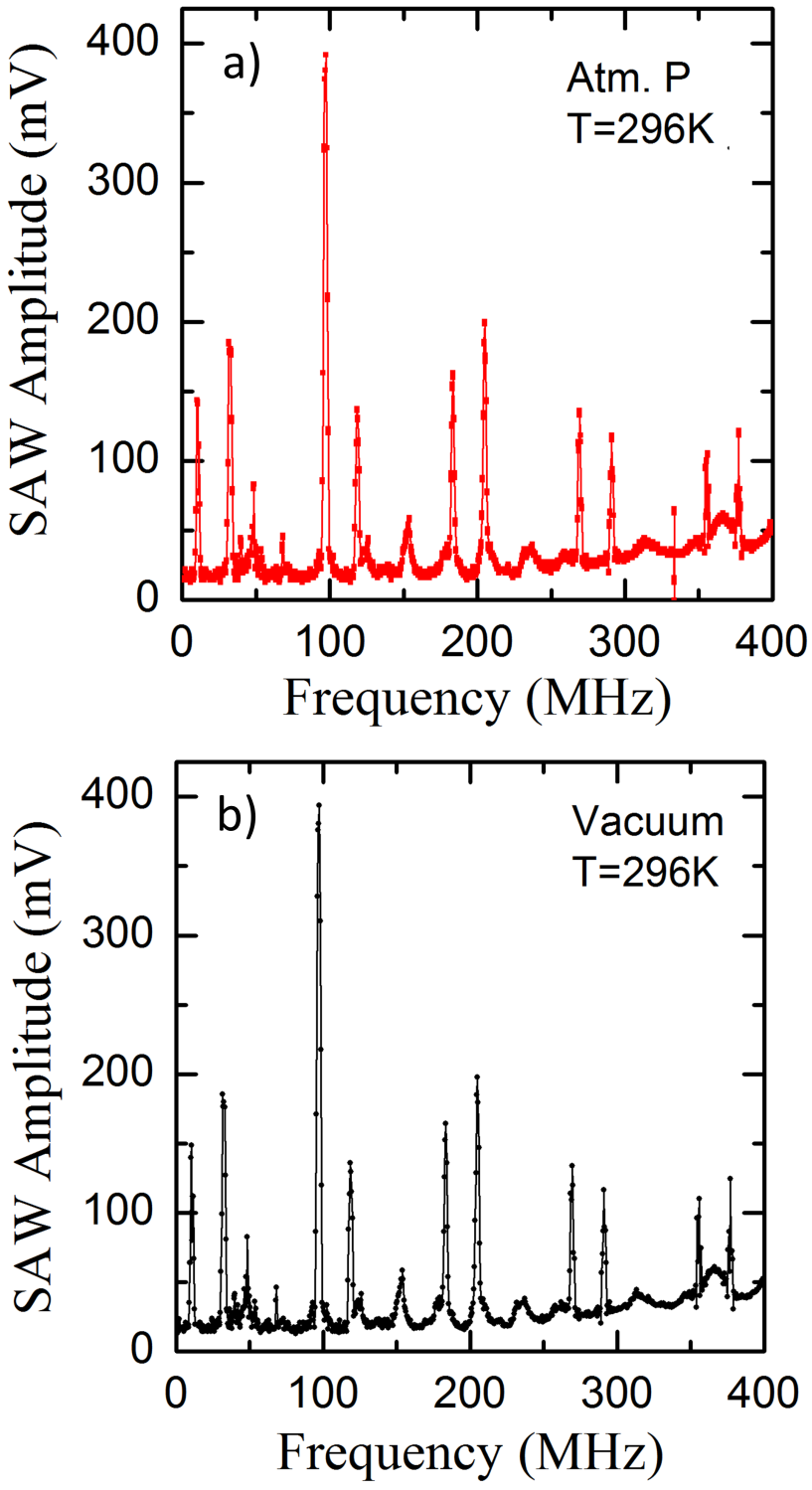


**Figure 4.9** The SAW amplitude plotted as a function of frequency at room temperature under a) atmospheric pressure b) vacuum.

transducers are excited by 20 dBm RF power, corresponding to an amplitude of 2.2 V. The SAWs are generated at different frequencies, out of which 11 MHz and 32 MHz are the fundamental resonant modes and others are their harmonics. The sharp peaks in Figure 4.9(a) correspond to the SAWs whereas the small blunt peaks are due to the leaky Rayleigh waves, which can be distinguished by their respective wave velocities, as discussed in the next section. One of the advantages of 128° Y-X orientation of lithium niobate is the low bulk wave generation, which causes attenuation as it carries some energy away from the surface. The insertion loss due to the conversion of electromagnetic fields into shear waves in the medium is estimated from this measurement. The total attenuation caused to the SAWs could also be due to the small water and gas molecules adsorbed on the surface. Generally molecules can be physically or chemically adsorbed on the surface depending on the type of intermolecular bonding. Chemical bonding permanently changes the molecule and are stronger as compared to the physical bonds where the weak Van der-Waals force holds the molecules in place. Chemical adsorption is less likely due to the un-reactive nature of lithium niobate, however physical adsorption can take place. To examine this, the bare lithium niobate SAW devices were mounted in a vacuum chamber to evacuate any physically adsorbed molecules and a fractional increase in the magnitude of SAWs is observed. The SAW amplitude measured at 296 K under a pressure of $3.6 \times 10^{-6}$ mbar is shown in Figure 4.9(b). The SAW at 11 MHz had the maximum increase of upto 4.5 % where as for most of the other SAW frequencies the change in amplitude is less than 1%. The higher harmonics at 355 and 377 MHz did experience a rise in amplitude of 3-5 % but because of their small amplitudes they are not preferred for measurements. More importantly, it becomes evident from Figure 4.9 that the attenuation caused by the physically adsorbed molecules on the surface of lithium niobate is negligible.

A temperature profile of the SAW amplitude is measured using a Lakeshore close-cycle liquid helium cryostat over a range of 48-296 K. The variation of SAW amplitudes at different temperatures is plotted as a function of frequency in Figure 4.10(a). An offset is introduced in Figure 4.10(a) for clear visibility. As the device is cooled down, a slight shift in the SAW frequency by 0.5 MHz is noticed. This is probably due to the difference in thermal expansion coefficients of the lithium niobate and metallic transducers, which

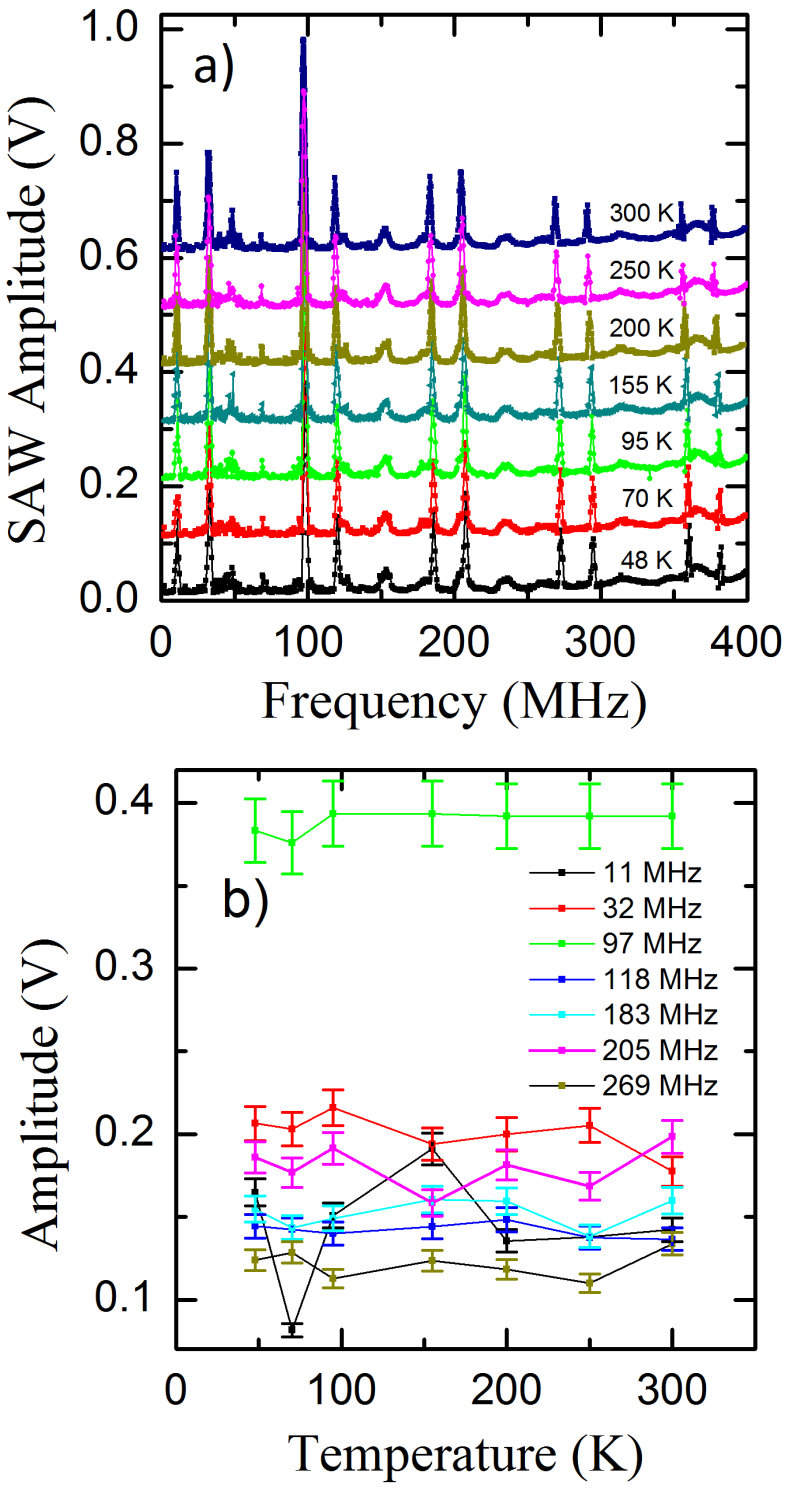


**Figure 4.10** a) The SAW amplitude plotted as a function of frequency at different temperatures. b) The SAW amplitude measured for a supply of 20 dBm RF power plotted as a function of temperature.

gets contracted as the sample is cooled down. Since this alters the pitch length of the transducers, the SAW wavelength changes by a small fraction resulting in the shifting of SAW frequency. The amplitudes at all SAW frequencies fluctuated between (1-15%) except for 97 MHz which remained constant throughout different temperatures. The SAW amplitude at maximum RF power supply of 20 dBm, is plotted as a function of temperature for different SAW frequencies in Figure 4.10(b). Out of all frequencies measured, the fundamental mode at 11 MHz fluctuated the most with temperature in a random manner. The non-monotonic random behaviour of SAW amplitude for different frequencies shows that it is not an implicit function of temperature. The behaviour of SAW amplitudes as a function of temperature was found to be device specific, which was measured for each device to estimate its SAW intensity at different temperatures.

### 4.8.2 SAW Velocity

The velocity of the SAWs is determined by measuring the time delay of the SAW signal that has an additional path length due to the propagation in lithium niobate. An RF splitter is used to divide the RF signal, coming from the signal generator in the form of a modulated pulse, into primary and reference signals. The primary signal that goes into the device carriers the maximum power where as the reference signal is a weak coupled signal that is used only as a reference in the oscilloscope. The length of wires from the splitter to the oscilloscope and the device is kept equal to minimise the delay caused via transmission in the wires. However, inside the cryostat extra wires, (which could not be avoided), might have led to some minor delay. Since the signal is traveling with the speed of light and the extra path length due to the electronics is of the order of half a meter, the delay caused would be some nanoseconds. This is a tiny fraction of the actual time delay experienced by the SAW while traveling through lithium niobate and is therefore ignored. The response of the device for a SAW and a leaky Rayleigh wave with respect to the reference signal is illustrated in Figure 4.11. The pulse generator generated a pulse of width 0.5 $\mu$s (see Figure 4.11(a)), which is modulated by the RF signal generator and passed through the RF splitter. It should be noted that this amplitude modulation was

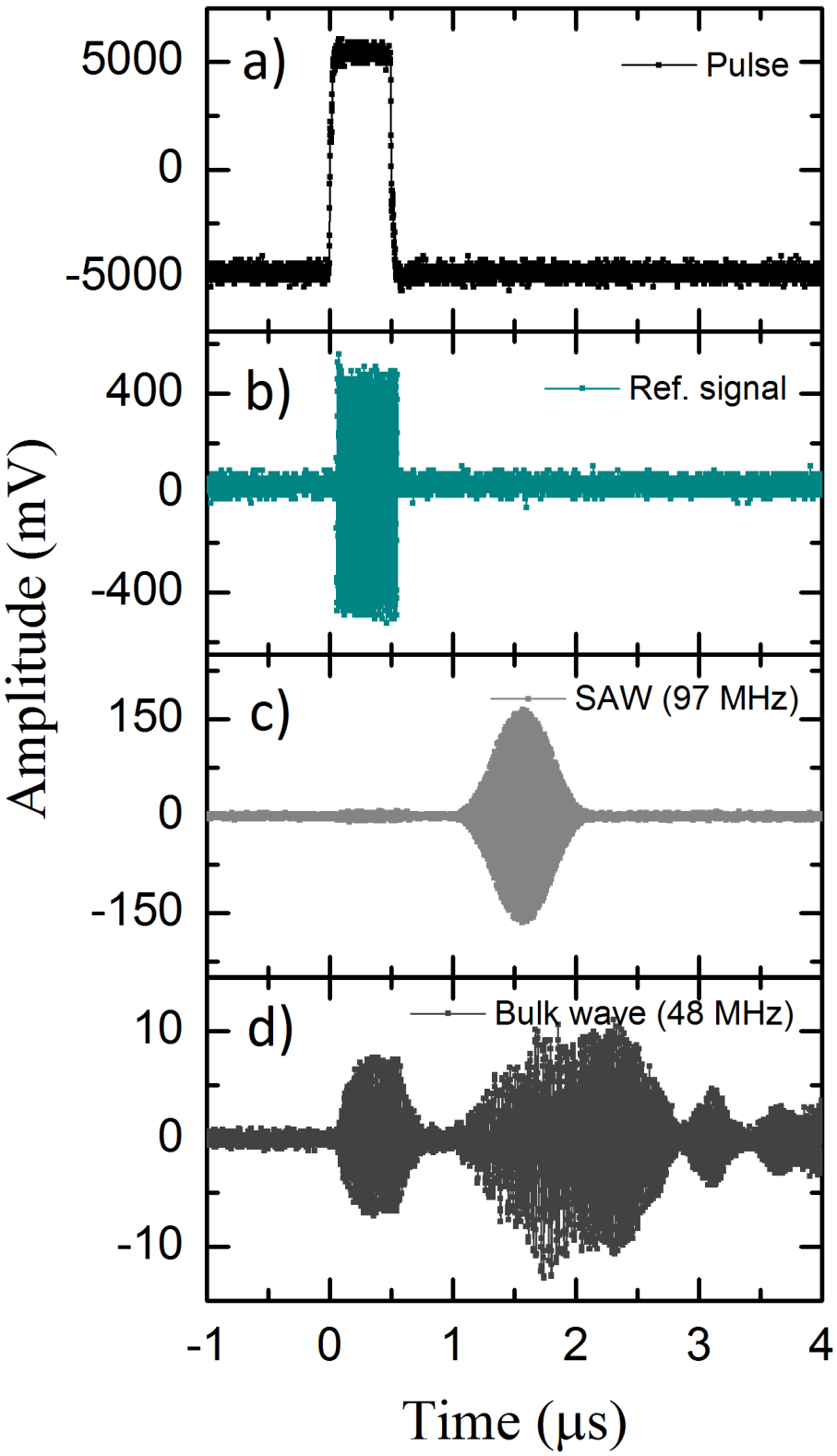


**Figure 4.11** The response of the transducers is plotted as a function of time to illustrate the difference between the bulk waves and SAWs. a) A pulse of 0.5 $\mu$s width, which is used for pulse modulation in the signal generator b) Reference signal coming from the RF splitter c) SAWs generated at 97 MHz d) Bulk waves generated at 48 MHz.

used only for measuring the SAW velocity, for all other measurements a continuous RF signal was used. The reference signal coming from the splitter is shown in Figure 4.11(b), a time delay of 1.3 $\mu$s is recorded for the SAW as shown in Figure 4.11(c). The unwanted bulk waves measured at certain frequencies, for instance at 45 MHz and 150 MHz (see Figure 4.9), can be clearly distinguished by their speed and the amplitude of the signal as shown in Figure 4.11(d). These leaky Rayleigh waves travel slower than the SAW with a speed of $\approx$ 2400 ms$^{-1}$. The signal measured in Figure 4.11(d) between 0-0.5 $\mu$s was due to the RF pick up from the input signal, which is common in SAW devices, but its weak strength means that it does not interfere with our measurements. The SAW velocity calculated from this measurement is $\approx 4000 ms^{-1}$, which is consistent with the free surface velocity of SAW in 128° Y-X lithium niobate that is 3977 ms$^{-1}$ [120].

### 4.8.3 Acoustoelectric Current

The gold contacts, identical to the ones used in the device for room and low temperature measurements, are fabricated in the acoustic beam path between the transducers and acoustoelectric current is measured. This is used to establish the absence of any acoustoelectric current in lithium niobate. The transducers are excited to produce SAWs and the acoustoelectric response of the device is measured through the gold contacts in the frequency range 1-500 MHz. There is no significant current measured at any of the SAW frequencies. A typical acoustoelectric measurement as a function of frequency is shown in Figure 4.12, where the peaks occur at random frequencies and their magnitude is more than a hundred times smaller than the acoustoelectric current measured in graphene (discussed in the following chapter).

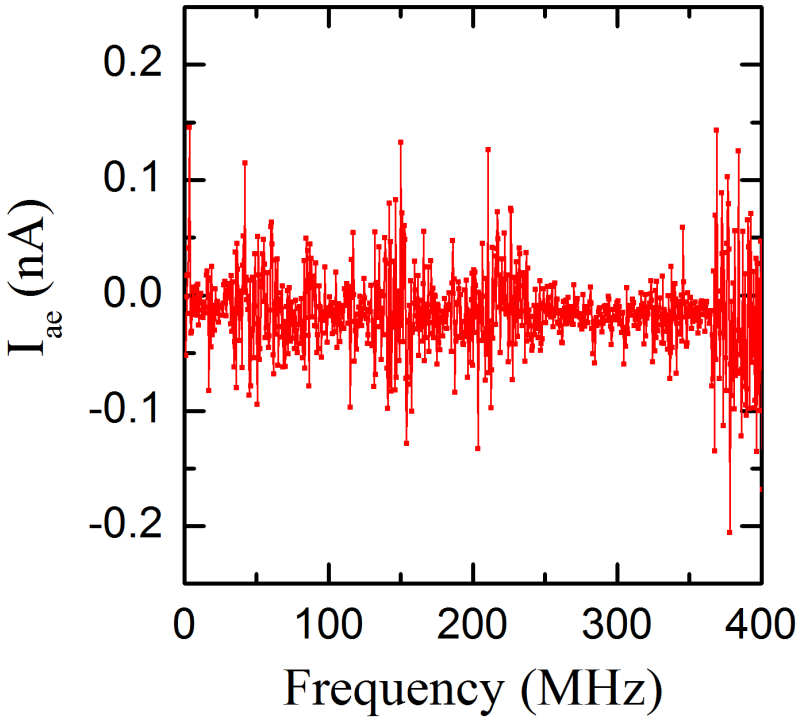


**Figure 4.12** The current measured between the electrodes is plotted as a function of frequency to illustrate the absence of acoustoeletric current in the bare lithium niobate device.

# 5 Room Temperature Acoustoelectric Transport

## 5.1 Introduction

The electric fields associated with a surface acoustic wave (SAW) propagating on a piezoelectric material have been extensively used over the last few decades as a contact-less probe of the electronic properties of a range of nanostructures including two dimensional electron and hole systems in both the integer [10][11] and fractional quantum Hall regimes [121], quantum wires [9] and quantum dots [8]. SAWs can also be used to trap and transport charge carriers, giving rise to a direct current along the direction of the wave propagation vector. This phenomenon, called the acoustoelectric effect, has been intensively studied to produce quantized current in 1-D channels [2], for light storage in quantum wells [12], and to induce charge pumping in nanotube quantum dots [14]. Over the last couple of years acoustically driven current flow in semiconductor nanostructures as a means of generating or controlling single electrons and photons [56][122] for metrology and quantum information processing, has attracted particular attention. Although graphene's large surface area and unique properties naturally lends itself to potential integration with SAW devices for potential applications in mass sensing, relatively little work has been reported so far. Acoustic charge transport has been demonstrated on graphene sheets transferred on lithium niobate [24] and epitaxial graphene on SiC [123], but a comprehensive study of the acoustoelectric current as a function of SAW intensity and frequency has been missing. We have addressed this problem in the work presented here.

In this chapter, the electrical characteristics of the graphene-SAW devices used in the experiments are discussed in section 5.2. The acoustoelectric current is monitored over several sweeps of SAW intensity to establish the constant conductivity of graphene throughout the measurement, as discussed in section 5.2.1. The transducer response of the devices is measured and compared with the manufacturer's data to estimate the intensity of the SAWs encountered by graphene at different SAW frequencies, as discussed in section 5.2.2. The experiments performed on the devices to study the acoustoelectric current as a function of SAW intensity and frequency are discussed in section 5.3. A relatively simple classical relaxation model, as discussed in section 2.4, is used to describe the observed interaction of SAWs with the carriers in graphene. A macroscopic acoustic charge transport over several hundred micrometers is demonstrated in these devices, which is an order of magnitude longer than previously reported by Miseikis *et al.* [24]. The summary of the chapter is given in section 5.4.

## 5.2 Electrical Characteristics

The schematic of a typical device used in the experiments described in this chapter is shown in Figure 5.1. Three such devices were made and their conductivity was measured between the different pairs of contacts. The difficulty in wire-bonding did not allow bonds to be made with all the fabricated contacts, therefore four-probe measurements could not be performed. The resistance was determined using a two-probe measurement technique, where a bias is applied across the contacts and the generated current is measured. Whilst this approach does not account for the contact resistance between the graphene and the metal, the large contacts (20 $\mu$m $\times$ 3 mm) ensures a small contact resistance [124]. The contacts BC, CD and BD (see Figure 5.1) used for the measurement are 200 $\mu$m, 300 $\mu$m and 500 $\mu$m apart respectively and the respective resistivity values measured between them for three different devices are shown in Table 5.1.

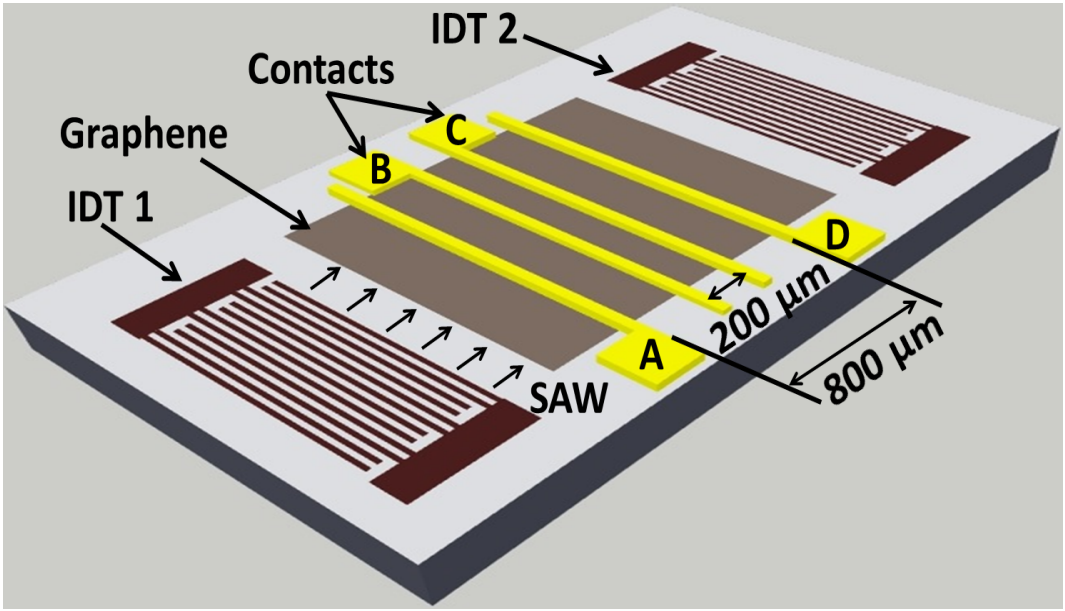


**Figure 5.1** The schematic of a typical device used in the room temperature measurement of the acoustoeelctric current.

| Contact separation ($\mu$m) | Device1 (k$\Omega/\square$) | Device2 (k$\Omega/\square$) | Device3 (M$\Omega/\square$) |
|---|---|---|---|
| 200 | 96 | 405 | 16 |
| 300 | 62 | 710 | 7 |
| 500 | 75 | 594 | 10 |

**Table 5.1** Resistance of graphene measured for different devices at different contact separations.

The resistivity values are higher than typically observed for CVD graphene transferred on $Si/SiO_2$ substrates. This could be attributed mainly to the lithium niobate substrate, along with the wrinkles, tears and unintentional doping arising from the graphene transfer process. Because of the large area transfer, it is also possible that the graphene is not uniform throughout, and patches of graphene are connected only by narrow channels. This inhomogeneity might be the reason behind the non-uniform resistance between different contacts. The results presented in this chapter are primarily from Device1, and similar results were obtained for Device2 and Device3. The devices were mounted in a vacuum chamber and evacuated to a pressure of $1.3 \times 10^{-6}$ mbar, the resistance was monitored during evacuation. The resistance in both the devices increased slowly as the pressure

decreased, most likely due to the removal of water molecules adsorbed on the surface, which are known to act as dopants [125]. The doping effect is brought on by the local electrostatic field associated with the dipole moment of the adsorbed water molecules, which can shift the defect states of the substrate with respect to the electrons in graphene. When these water molecules are removed, the Fermi level shifts towards the charge neutrality point, which results in the increase in resistance [125]. The resistance value was also found to fluctuate slightly as a function of time, which may be attributed to the substrate-induced structural distortion, local charge disorder, adsorbates and charge transfer from/to the trap sites in the dielectric substrate, which play an important role in determining the transport properties of graphene. Such trap states [126], adsorbates in the form of residues from the lithography process, and substrate induced distortion [127] have been reported for graphene on $Si/SiO_2$, however no such study is available for graphene on lithium niobate.

### 5.2.1 Reproducibility

The resistance of the devices were constantly increasing as the vacuum chamber was evacuated. Therefore, all the measurements were carried out when the rate of increase in this resistance was very slow (up to 1 k$\Omega$/h). To verify that the acoustoelectric current does not change by a huge amount over the course of measurement, it was measured as a function of SAW intensity. The sweeping of applied RF power in each measurement would take ten minutes and were repeated several times in the span of one hour. The results obtained for the acoustoelectric current at 11 MHz are plotted in Figure 5.2, where the SAW intensity was calculated from the measured amplitude. No change in the acoustoelectric current shows that the conductivity of graphene remains constant throughout the measurement (see Equations 2.42 and 2.46). In general, hysteresis is observed in the conductance characteristics of graphene on $Si/SiO_2$ while sweeping the gate voltage [126], which could be a result of charge transfer from the adsorbed molecules (like water) or charge injection to/from the trap sites in the dielectric. Since, the acoustoelectric transport involves the dragging of carriers in graphene, the charge transfer to/form the adsorbates is possible but the results (see Figure 5.2) suggest that such charge transfer, if any, are negligible at

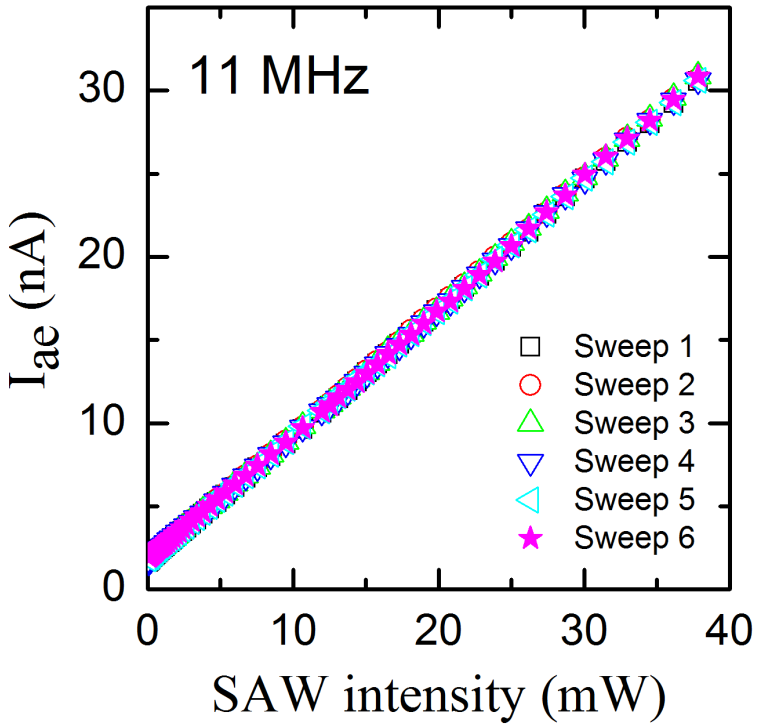


**Figure 5.2** The plot of acoustoelectric current as a function of SAW intensity measured over several sweeps to show its reproducibility.

room temperature during the measurements. Similar results were obtained for other SAW frequencies as well.

### 5.2.2 Transducer Response

The transducer response of Device1 was measured in the frequency range 1-500 MHz. One of the transducers was excited using signal generator, which generates radio frequency (RF) waves of amplitude $V_0$=6.335 V (peak to peak voltage) for maximum input power. The transducer response of a typical device without any graphene and metallic contacts on it, as supplied by the manufacturer is shown in Figure 5.3. The first peak in Figure 5.3 correspond to fundamental frequency at 11 MHz, whereas the rest of the peaks are its higher harmonics. Because of the double-electrode transducers used only the odd multiples of the fundamental frequency are observed in the harmonics.

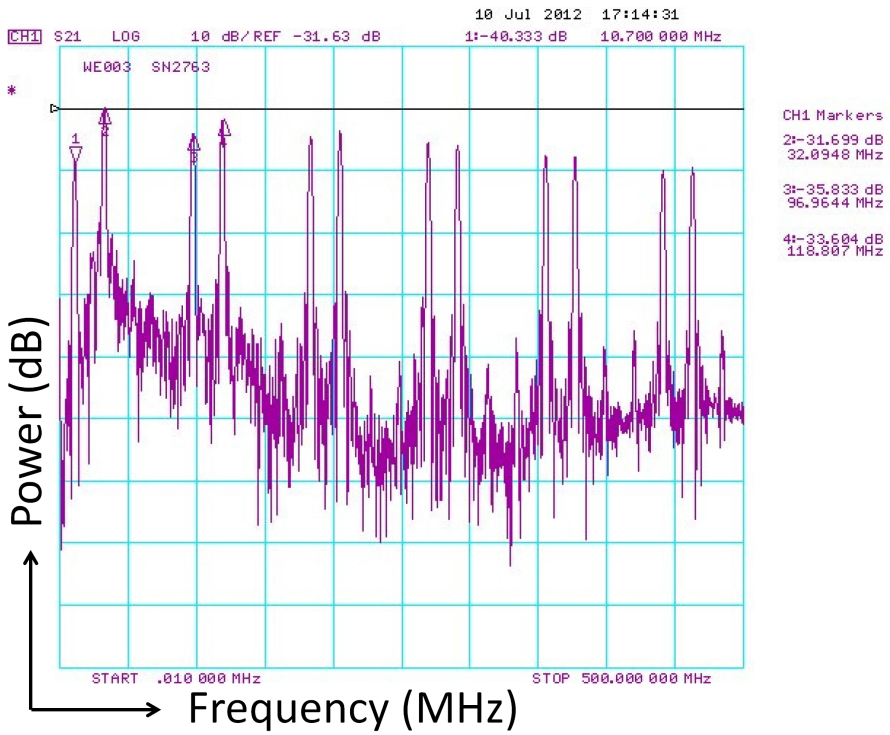


**Figure 5.3** Relative amplitude plotted as a function of frequency for bare lithium niobate device (obtained from the manufacturer).

The SAW amplitude for the graphene-SAW devices were measured in the vicinity of these SAW frequencies, for instance the relative SAW amplitude plotted as a function of frequency for Device1 is shown in Figure 5.4. The ratio of the input and output voltages, $V/V_0$ was expressed in decibel (dB) to make a comparison with the manufacturer's data. Each data point in Figure 5.4 is a mean of 100 observations. The relative amplitude at 11 MHz and 32 MHz was measured to be -28.7 dB and -32.5 dB respectively (see Figure 5.4) as compared to -40.3 dB and -31.7 dB (see Figure 5.3) for the same frequencies in a bare device. The discrepancy between the measured transducer response and the manufacturer's data could be attributed to different reasons. For example; the graphene-SAW devices undergoes a complex fabrication process, which means that the surface may not be as smooth as the fresh bare device, which might affect the amplitude of the SAW; the experimental conditions including the temperature, pressure and measurement setup may affect the SAW amplitude; and most importantly the graphene deposited on the surface may be interacting differently with SAWs of different wavelength, resulting in more

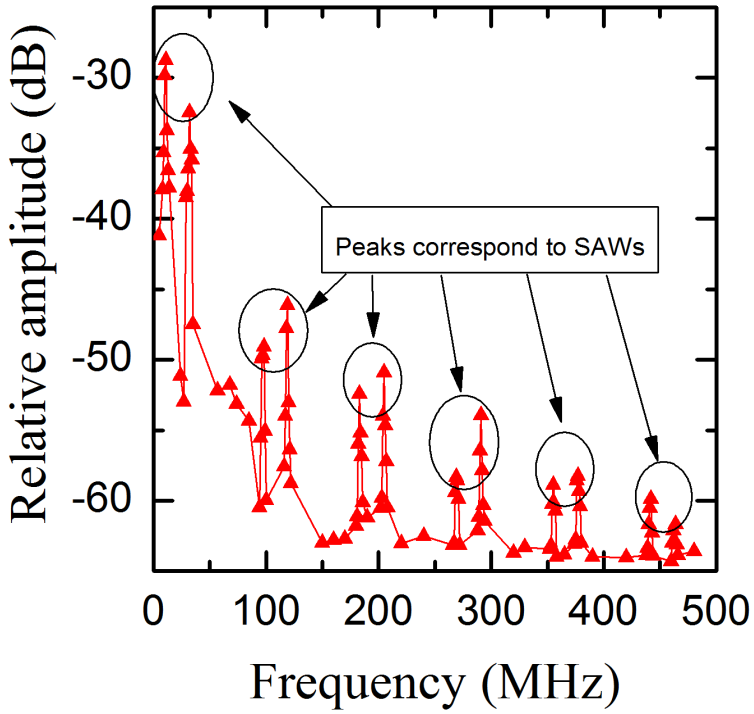


**Figure 5.4** The relative amplitude measured from the oscilloscope is plotted as a function of frequency for graphene-SAW device (Device1).

suppression of the weak high frequency signals, which is discussed in detail in the next chapter.

## 5.3 Acoustoelectric Current

### 5.3.1 SAW Frequency and Intensity Dependence

The acoustoelectric current generated in graphene due to the interaction of SAWs was measured using a Keithley 2400 sourcemeter. No bias was applied while measuring the acoustoelectric current, which for Device1 is plotted as a function of frequency in Figure 5.5. Qualitatively similar results were obtained for Device2 and Device3, but the acoustoelectric current was much smaller owing to their low conductivity. In Figure 5.5, the sharp peaks in current observed at all SAW frequencies proves the acoustoelectric origin of current. A positive acoustoelectric current as high as 80 nA is measured along the direction

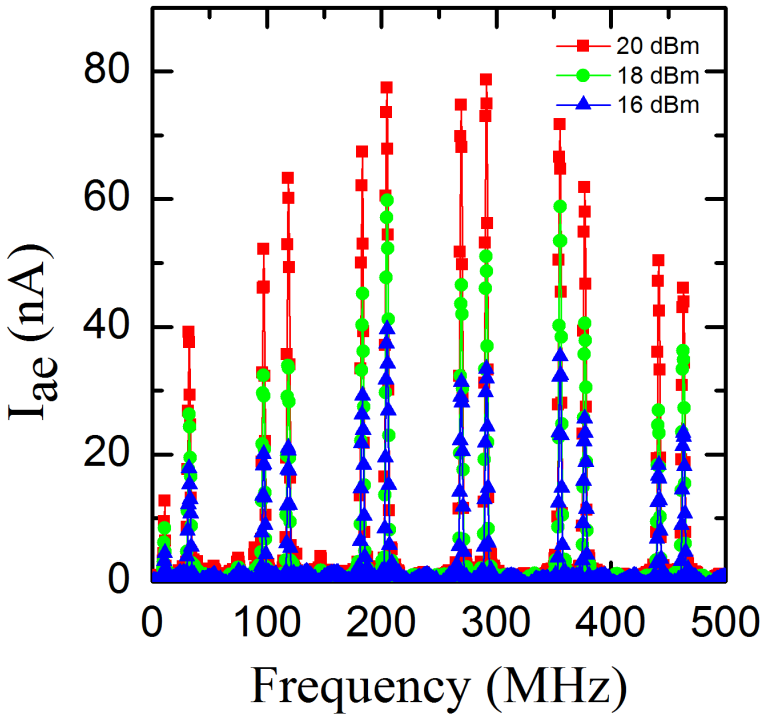


**Figure 5.5** Measured acoustoelectric current plotted as a function of frequency for different SAW intensities.

of SAW propagation. This indicates the transport of holes with SAWs, which is consistent with the fact that CVD graphene is thought to be p-doped [128] by PMMA and etchant salt residues. Similar results were obtained by Miseikis *et al.* on much smaller devices [24], where the contacts were only 20 $\mu$m apart. The magnitude of the acoustoelectric current decreases with SAW intensity, as shown in Figure 5.5. To establish it qualitatively, the acoustoelectric current was measured as a function of SAW intensity. The estimation of the SAW intensity at different SAW frequencies was based on the assumption that the energy loss due to the attenuation of SAWs while traveling in the substrate is negligible compared to the transmission loss by the transducers, and that both the input and output transducers are identical and exhibit the same transduction loss. Using these assumptions and the knowledge that the output signal has undergone the transduction process twice, we can write an expression for the SAW intensity as it propagates along the device. The relative amplitude $V$ (power $P$) measured for an input voltage $V_0$ (power $P_0$) was used to calculate the power loss in $dB$:

$$dB = 20 \log \frac{V}{V_0} = 10 \log \frac{P}{P_0} \tag{5.1}$$

The graphene at the center of the substrate encounters a SAW that has suffered a transduction loss only due to the input transducer *i.e.* $dB/2$, which is often termed 'insertion loss'. The SAW intensity flux $F$, defined as the ratio of the SAW intensity encountered by graphene and the aperture (width) $p$ of the transducer, is given by

$$F = \frac{P_0 10^{\frac{dB}{20}}}{p} \tag{5.2}$$

The measured acoustoelectric current is plotted as a function of the estimated SAW intensity flux in Figure 5.6. The lines in Figure 5.6 represent the simulations based on a simple classical relaxation model, which is discussed in the next section.

The intensity flux is extended only up to 0.3 $\mathrm{Wm}^{-1}$ in Figure 5.6 to make the higher frequencies clearly visible. The SAW frequencies used in the measurement is well distributed in the range 1-400 MHz, and it is evident from Figure 5.6 that the acoustoelectric current is directly proportional to the SAW intensity.

### 5.3.2 Simple Classical Relaxation Model

A simple classical relaxation model was used to explain the acoustoelectric current dependence on SAW intensity and frequency. This model, discussed earlier in Chapter 2, describes the piezoelectric interaction of graphene with the SAWs that leads to the attenuation $\Gamma$ of the SAW, which is given by

$$\Gamma = K^2 \frac{\pi}{\lambda} \left[ \frac{\sigma_{2D}/\sigma_M}{1 + (\sigma_{2D}/\sigma_M)^2} \right] \tag{5.3}$$

where $K^2 = 0.056$ [129] is the effective piezoelectric coupling coefficient, $\lambda$ is the SAW wavelength and $v$ is the SAW velocity when the surface is metallised (approximately 4000 $\mathrm{ms}^{-1}$ in lithium niobate), $\sigma_{2D}$ is the sheet conductivity of graphene and $\sigma_M$ is the characteristic conductivity of lithium niobate. For a hybrid system based on lithium

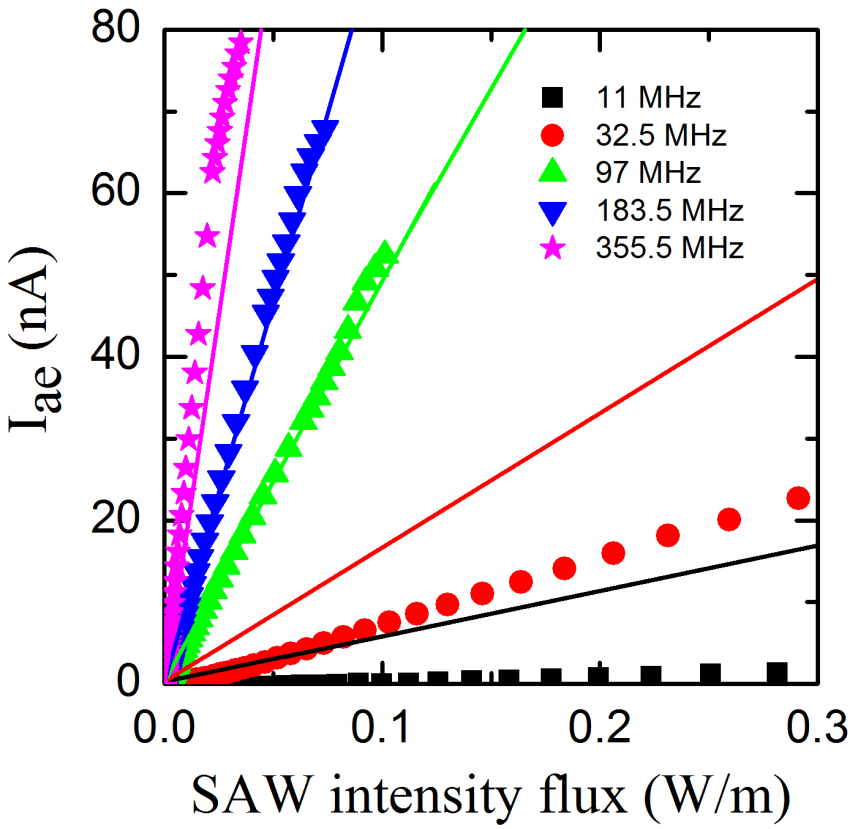


**Figure 5.6** The acoustoelectric current plotted as a function of SAW intensity flux (symbols). Lines represent the simulations based on the simple classical relaxation model.

niobate, the characteristic conductivity $\sigma_M$ is approximately given by [129] :

$$\sigma_M \approx v\epsilon_0 \left( \sqrt{\epsilon_{xx}^S \epsilon_{zz}^S} + 1 \right) \tag{5.4}$$

where $\epsilon_0$ is the permittivity of free space and $\epsilon_{xx}^S$ and $\epsilon_{zz}^S$ are the dielectric constants of lithium niobate at constant stress, which gives $\sigma_M = 1.25 \times 10^{-6}\ \square\Omega^{-1}$. The attenuation causes a loss of energy from the SAW leading to a proportional loss of momentum [129], which acts as a force on the carrier system and is the mechanism behind the acoustoelectric effect.

In a closed circuit and in the absence of a magnetic field the acoustoelectric current density

$j$, as described by Rotter *et al.* [129] and Fal'ko *et al.* [130], reduces to

$$j = -\frac{\mu \Gamma F}{v} \tag{5.5}$$

where $\mu$ is the mobility of the charge carriers. Equation (5.5) gives a linear dependence of acoustoelectric current on SAW intensity flux $F$ and attenuation coefficient $\Gamma$. This model applies only when there is a negligible modulation of the carrier concentration by the SAW, which is guaranteed in the low power experiments presented here. The acoustoelectric effect, as described in Section 2.3, is a result of the net force exerted by the SAW on the charge carriers. This force depends on a number of factors including the acoustic charge, relaxation time of the carriers, acoustic power density, wavelength of the SAW, and temperature. It should be noted that the length of the sample (or the separation between the electrodes) does not directly affect the force exerted on the carriers. However, in case of a non-homogeneous sample a change in its length may alter its conductivity by variable amount, which can indirectly affect the acoustic charge and relaxation time of the carriers, and therefore the acoustoelectric effect produced. In a simplified manner, the inhomogeneous sample can be described as an infinite network of variable resistances. According to the percolation model proposed by Levy *et al.* [131], the macroscopic resistance measured for such a network is the response of the sample to a direct current potential *i.e.* an alternating current of infinite wavelength. An alternating current of finite wavelength on the other hand selects a section of the sample and measures its local sheet resistance. The size (length) of these sections are $\lambda/2\pi$ [131], where $\lambda$ is the SAW wavelength. Therefore, the local sheet resistances measured by the SAWs of different wavelengths differs, which changes the attenuation of the wave, and therefore the acoustoelectric current. It should be pointed out that the length (58 $\mu$m) of graphene probed by the largest SAW wavelength (364 $\mu$m) is well within the separation of electrodes (300 $\mu$m) used in the experiments presented here.

Simulations based on the simple classical relaxation model were performed to aid interpretation of the experimental results, which are plotted as lines in Figure 5.6. To obtain the best qualitative agreement with the measured data, a mobility value of 8 $\mathrm{cm^2V^{-1}s^{-1}}$ is

used. Here, the mobility is used as a free fitting parameter in Equation (5.5) because $j$, $F$ and $v$ were measured, and $\Gamma$ was calculated using Equation (5.3), where $\sigma_{2D}$ was measured and all other quantities were constant at any given SAW wavelength. It should be noted that lack of gate electrodes on the device means that the mobility could not be measured directly. The value of the mobility assumed for fitting the experimental data is much smaller than typical room temperature mobilities obtained for CVD graphene on $Si/SiO_2$ substrates. However the corresponding hole density, approximately $5 \times 10^{12}$ cm$^{-2}$, was consistent with values typically obtained from graphene on $Si/SiO_2$. The contrasting difference with the typical mobilities reported could be attributed to the different properties of lithium niobate substrate, and also to the fact that the simple classical relaxation model does not take any non-uniformity in graphene into account. The acoustoelectric current is dependent on the average mobility across the device but is also likely to be limited by the lowest mobility the SAW encounters along its propagation path. For example, the large number of grain boundaries in the polycrystalline CVD graphene (due to the small size of the single crystal grains, which are typically a few hundred nanometers across [132]) could dramatically affect the average mobility. The measured acoustoelectric current might, therefore, be a useful probe of the uniformity of large graphene devices. It is also possible that the difference between the simulated and measured values of the current at long SAW wavelengths is also somehow linked to the non-uniformity of graphene. To illustrate this argument, the mobility extracted at each SAW frequency from the slope of the linear fit to the measured data are plotted as a function of frequency in Figure 5.7, which clearly shows that the SAWs with large wavelength experiences lower mobility of the charge carriers in graphene. However, for better understanding of the effect of the wavelength of SAW on the mobility of graphene carriers, further investigation is required.

The acoustoelectric current at a SAW intensity flux of 0.03 Wm$^{-1}$ for different SAW frequencies was obtained from Figure 5.6. It is plotted as a function of frequency in Figure 5.8 showing the linear dependency of acoustoelectric current on SAW frequency, which is consistent with the attenuation of the SAWs being described by the simple classical relaxation model. The attenuation $\Gamma$ attains a maximum at $\sigma_{2D} = \sigma_M$ (from Equation (5.3)), and a linear dependence on the acoustoelectric current density means that the acousto-

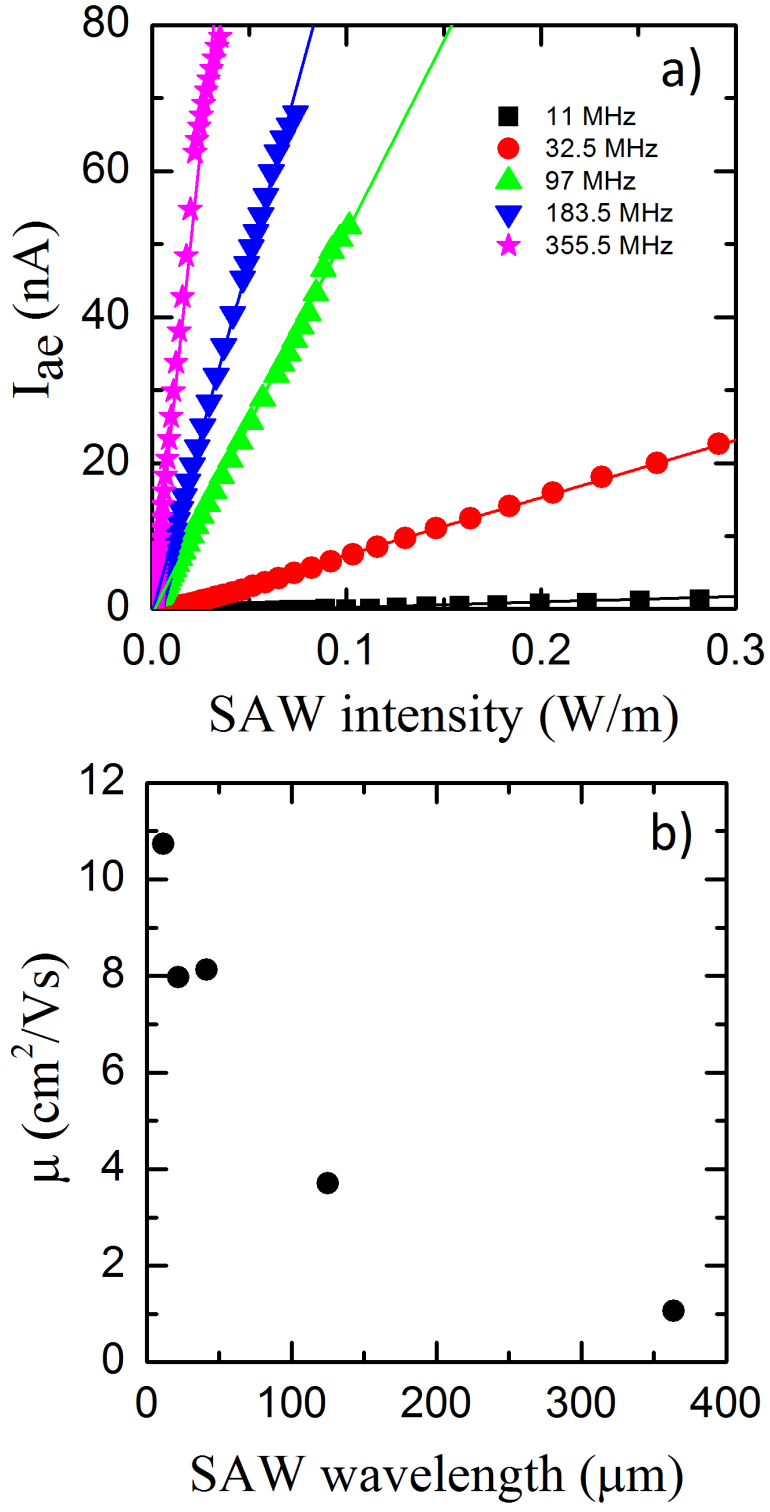


**Figure 5.7** a) Measured acoustoelectric current plotted as a function of SAW intensity flux for different SAW frequencies. b) The mobility extracted from the slope of Figure 5.6 plotted as a function of SAW wavelength.

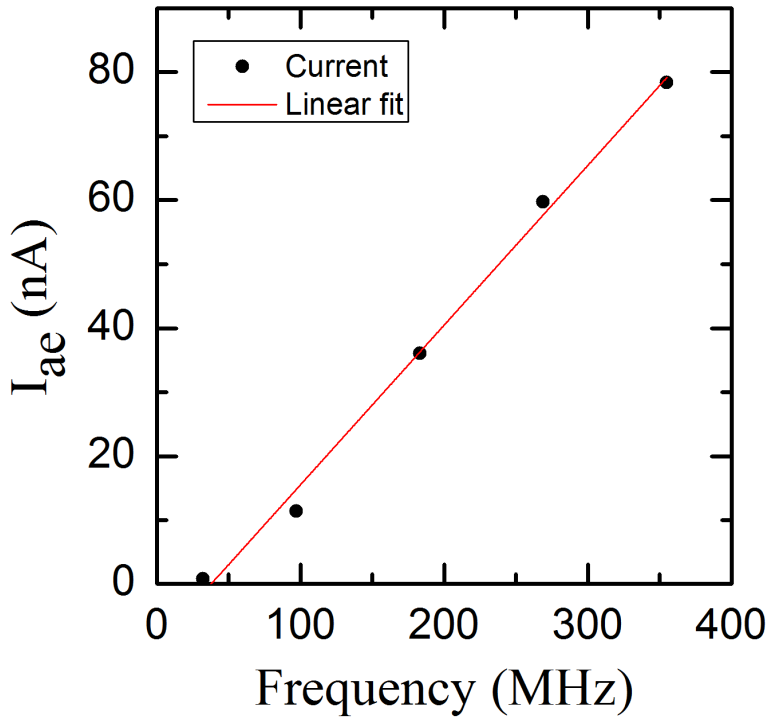


**Figure 5.8** Measured acoustoelectric current at a SAW intensity flux of 0.03 $Wm^{-1}$ is plotted as a function of SAW frequency.

electric current also attains maximum at this conductivity for a given SAW intensity and mobility.

The Device1 and Device3 were measured in atmospheric pressure and vacuum, and the change in acoustoelectric current measured is shown in Table 5.2, which was in complete agreement with the simple classical relaxation model. The evacuation of the chamber resulted in the removal of water molecules from the surface of graphene that were acting as p-dopants. As a result, the conductivity of both the devices, Device1 and Device3, decreased respectively from $1.19 \times 10^{-5}$ $\Omega^{-1}$ in air to $6.49 \times 10^{-6}$ $\Omega^{-1}$ in vacuum, and $1.06 \times 10^{-6}$ $\Omega^{-1}$ in air to $8.66 \times 10^{-7}$ $\Omega^{-1}$ in vacuum. But in this evacuation process, the magnitude of the acoustoelectric current on average approximately doubled (for the same SAW frequency and intensity) in Device1, whereas in Device3 it fell by approximately 15 % on average. This behaviour could be understood from the attenuation curve given by Equation (5.3). Since, the acoustoelectric current is directly proportional to $\Gamma$, a change in $\Gamma$ through the change in conductivity of the sample $\sigma_{2D}$ directly affects the

| | Device1 | | | Device3 | | |
|---|---|---|---|---|---|---|
| Frequency | $I_{ae}$ (nA) | | | $I_{ae}$ (nA) | | |
| (MHz) | vac. | atm. | Δ% | vac. | atm. | Δ% |
| 11 | 25.2 | 20.5 | 23.2 | 11.5 | 12.8 | -10.6 |
| 32 | 137 | 65.5 | 109 | 53.4 | 56.1 | -4.87 |
| 97 | 135 | 64.4 | 110 | 24.8 | 36.3 | -31.8 |
| 183 | 160 | 79.9 | 101 | 16.6 | 19.1 | -13.1 |
| 269 | 173 | 90.5 | 91.4 | 12.0 | 14.6 | -18.1 |
| 355 | 171 | 90.4 | 89.4 | 7.76 | 9.02 | -14.3 |

**Table 5.2** Change in acoustoelectric current (Δ%) for Device1 and Device3 as the pressure was reduced from atmosphere (atm.) to vacuum (vac.).

acoustoelectric current. A schematic representation of the change in attenuation for both the devices is given in Figure 5.9. In the case of Device1, $\sigma_{2D}$ was much higher than the characteristic conductivity $\sigma_M$, and a decrease in conductivity pushes the attenuation of the SAW towards the peak of the attenuation curve (see Figure 5.9).

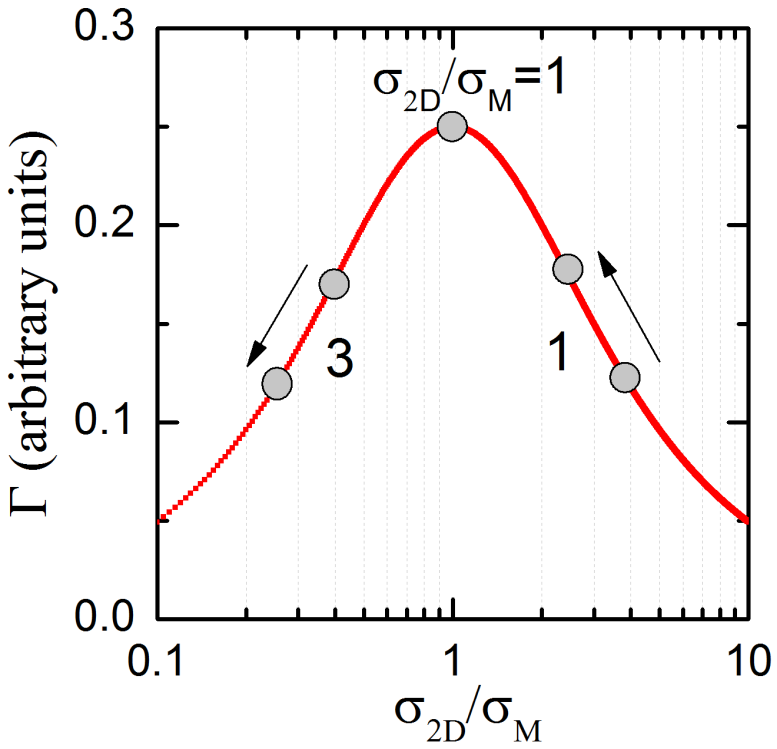


**Figure 5.9** The attenuation, calculated from the simulations based on the simple classical relaxation model, is plotted as a function of $\sigma_{2D}/\sigma_M$. The arrow schematically represents the positions of Device1 and Device3 before and after the evacuation of the containment chamber, which determines the relative rise or fall in acoustoelectric current.

Therefore, the rise in Γ causes rise in acoustoelectric current. On the other hand, the

$\sigma_{2D}$ of Device3 in atmosphere was much lower than $\sigma_M$, and evacuation decreases the conductivity even further, which reduces $\Gamma$ and consequently a decrease in acoustoelectric current was observed.

## 5.4 Summary

In summary, the acoustoelectric current was studied as a function of SAW intensity and frequency in a hybrid system of graphene/lithium niobate, and a relatively simple classical relaxation model was used to describe the interaction between SAWs and the graphene carriers. The mobility of holes obtained is comparatively much lower than the typical values in $Si/SiO_2$ substrates which could be attributed to the different properties of lithium niobate and the limitation of simple classical relaxation model in not accounting for the inhomogeneity of graphene. However, more importantly a macroscopic acoustoelectric charge transport over several hundred micrometers was demonstrated, which opens up the feasibility of large-area graphene-based SAW devices for a wide range of applications.

# 6 Temperature Dependence

## 6.1 Introduction

The integration of graphene with lithium niobate could be very useful in the control and transport of charge carriers in SAW devices. Constant efforts are being made to make use of the special properties of graphene [4], including the large surface area, ambi polar charge carriers and high mobility. A carrier mobility as high as 200,000 $cm^2V^{-1}s^{-1}$ has been reported in suspended graphene at low temperatures (below 10 K) [18]. For technological applications though, a suspended geometry is not always plausible as it limits the device architecture, therefore, it is important to study the prospective of graphene on substrates. The substrate strongly influences the charge carrier mobility and the thermal conductivity in graphene, which were found to be an order of magnitude higher in suspended graphene as compared to the graphene on substrates [133]. This difference can be observed through the temperature dependence of the conductivity of graphene, which is primarily determined by the scattering of charge carriers by phonons in graphene and surface phonons of the substrate. This temperature dependence of the conductivity has been observed and well-understood in graphene on substrates like $SiO_2$, SiC and hBN [101, 134], but relatively little work has been reported on lithium niobate. It can be investigated by the study of acoustoelectric current in graphene, which implicitly depends on its conductivity. At room temperature, this study reveals a linear dependence on both the SAW intensity and frequency [135], where the attenuation of the SAW can be described by a simple classical relaxation model, as discussed in the previous chapter. Here, the acoustoelectric current has been investigated as a function of temperature, SAW intensity, and frequency. It was

observed that at high SAW frequencies, the measured acoustoelectric current decreases with decreasing temperature, but remains positive, which corresponds to the transport of holes, over the whole temperature range (48-300 K) studied. The current also exhibits a linear dependence on the SAW intensity, consistent with the interaction between the carriers and SAWs being described by the classical relaxation model. At low temperatures and SAW frequencies, the measured acoustoelectric current no longer exhibits a simple linear dependence on the SAW intensity, and the direction of the acoustoelectric current is also observed to reverse under certain experimental conditions.

In this chapter, the experiments performed on the graphene-SAW devices are discussed in Section 6.2, where the electrical characteristics of the devices measured at room temperature and their resistance as a function of temperature are discussed in section 6.2.1. Section 6.2.2 discusses the change in SAW amplitude as a function of temperature, which was used to calculate the actual SAW intensity encountered by graphene for different SAW frequencies at different temperatures. In section 6.2.3, the acoustoelectric current measured for different SAW frequencies is discussed as a function of temperature and the theory is extended to accommodate the anomalies observed during experiments, followed by the summary of the chapter in section 6.3.

## 6.2 Graphene-SAW Devices

### 6.2.1 Electrical Characteristics

The same graphene-SAW devices used in the previous chapter for room temperature measurements that had a sheet of single-layer graphene transferred on the surface of lithium niobate, were investigated to study the interaction of SAWs with graphene at different temperatures. The current-voltage (I-V) characteristics of the devices are measured at room temperature and atmospheric pressure by using the two probe measurement technique. The current sweep was done cautiously only in a small range (-30 to +30 $\mu$A) to avoid breakdown of the device. The electrodes used for measurement were 200 $\mu$m, 300

$\mu$m and 500 $\mu$m apart. High resistances of the order of tens of k$\Omega$ were measured between all the possible contact pairs for both the devices (Device1 and Device2). Typically, the resistance of graphene decreases with temperature due to its semi-metallic nature, as observed for graphene on $SiO_2$, SiC, and hBN [134]. However, we observed a non-monotonic behaviour for both the devices as the temperature decreased from 300 K to 48 K. Both the devices showed a similar behaviour up to 200 K, following a decrease in resistance with decreasing temperature. Below 200 K, the resistance of both the devices behaved differently, where in Device1, the resistance started increasing with further decrease in temperature as compared to Device2, where it initially increased and then started decreasing below 95 K, as shown in Figure 6.1. It should be noted that the results presented here were measured between contacts that were 300 $\mu$m apart in both the devices, but similar behaviour was observed between other pairs of contacts as well. The difference in the behaviour of resistances, at low temperature, between the two devices could be due to their charge puddles and impurity sites, which varies for different devices. The disorder induced by the charge puddles and impurity sites may exhibit different transport mechanism at different temperature resulting in the temperature dependence of resistance [103]. The change in temperature may also build up pyroelectric voltage on the surface of lithium niobate that might induce extra charge carriers in graphene leading to a change in conductivity.

### 6.2.2 SAW Amplitude

The devices were mounted on the cold finger of a close-cycle cryostat and cooled from room temperature to 48 K in variable steps and heated back to the room temperature. The SAW amplitude at different temperatures was measured as a function of the RF power supplied from the signal generator, which was relatively consistent with their respective room temperature behaviour. However, below 50 K the SAW propagation was suppressed for low frequency (below 100 MHz) SAWs and enhanced for high frequency (above 100 MHz) SAWs. The relative amplitude obtained for Device1 at 11 MHz and 269 MHz is plotted as a function of temperature in Figure 6.2. The peculiar behaviour observed below 50 K is not completely understood but one of the reason could be the wavelength

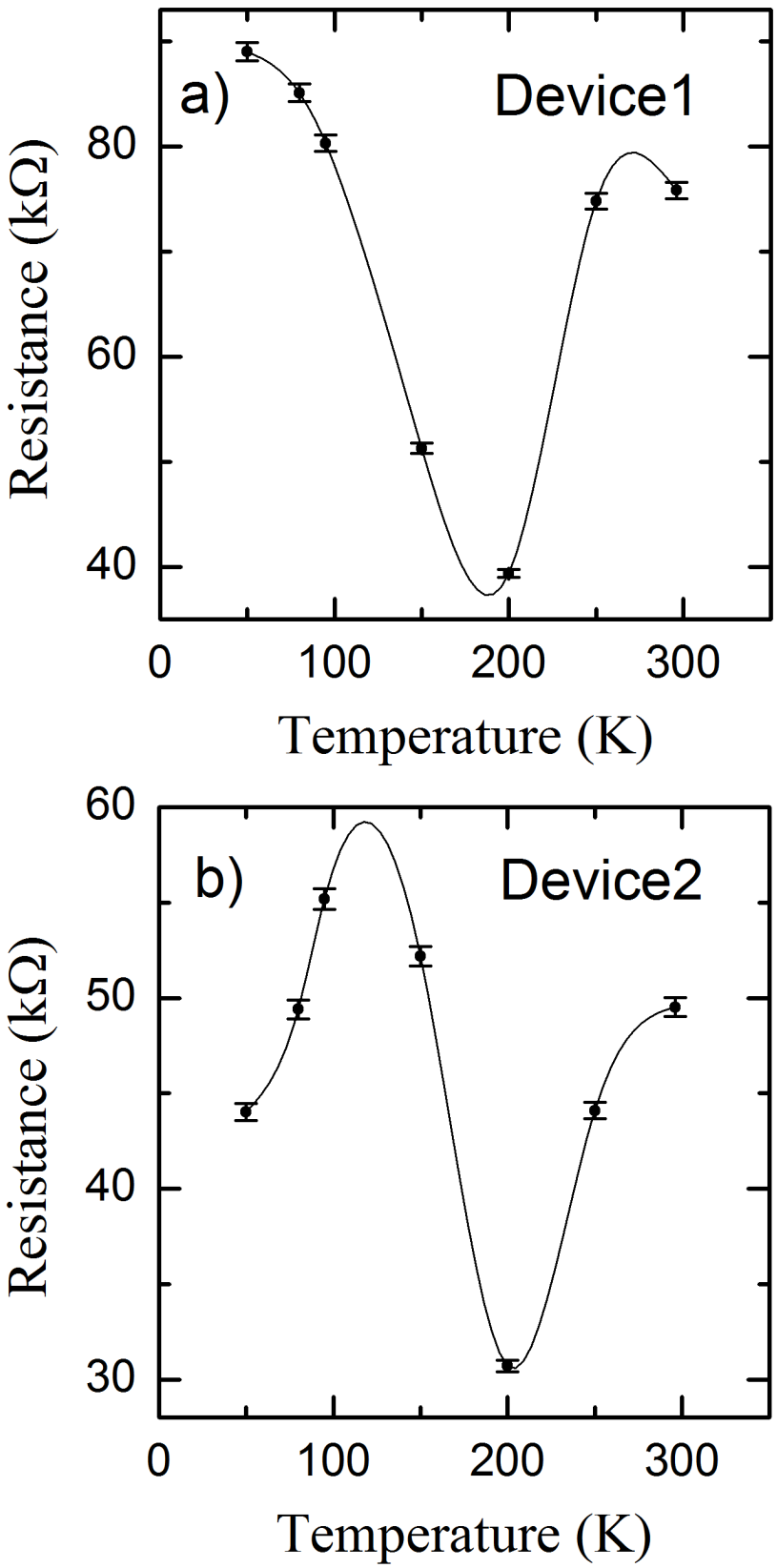


**Figure 6.1** The resistance of a) Device1 and b) Device2 plotted as a function of temperature, where the scatters are connected by spline.

dependent interaction of the SAW with the carriers in graphene, which becomes strongly affected by the spatial charge inhomogeneity at low temperatures as discussed in the following section. The SAW amplitude measured for a power supply of 20 dBm was obtained for all SAW frequencies at different temperatures and the relative amplitude was calculated by normalising with their respective room temperature values. These values were used to determine the actual SAW intensity encountered by graphene at different temperatures (see Section 4.7.2). The high frequency SAW, for example SAW at 269 MHz correspond to a wavelength of 15 $\mu$m, which is comparable to the average grain size in graphene, therefore it probes the graphene at much smaller scale compared to the low frequency SAWs. In the following measurements, we have primarily used the SAW at 269 MHz to describe the temperature dependence of the acoustoelectric current in graphene.

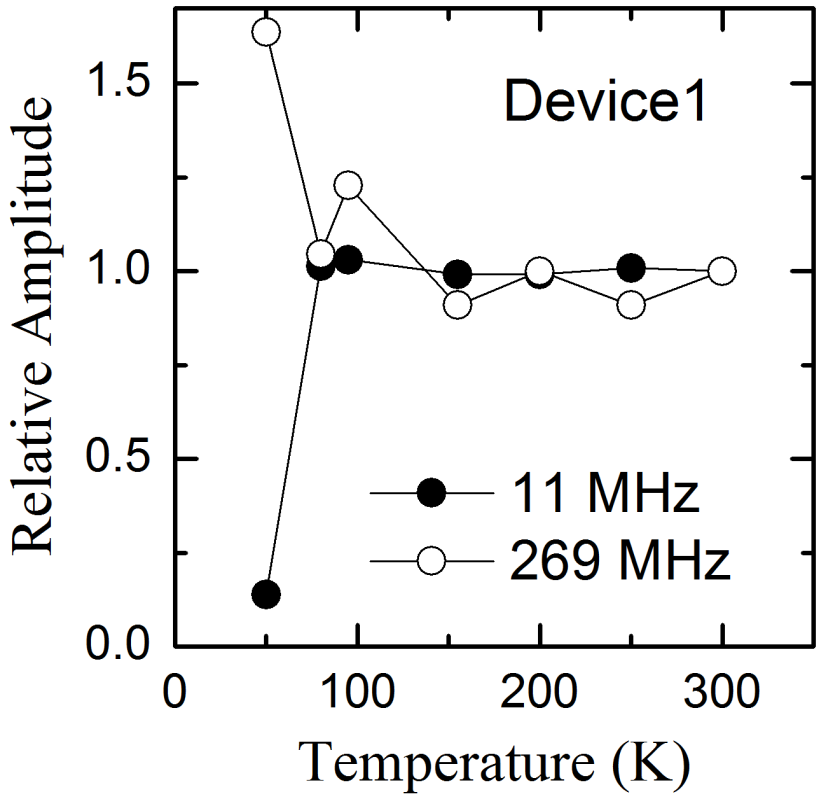


**Figure 6.2** The relative SAW amplitude plotted as a function of temperature for the SAW at 269 MHz.

### 6.2.3 Temperature Dependence

The acoustoelectric current in graphene is measured as a function of temperature, SAW intensity, and frequency (see Figure 6.3), which can be broadly classified into measurements done for low (below 100 MHz) and high (above 100 MHz) frequency SAWs.

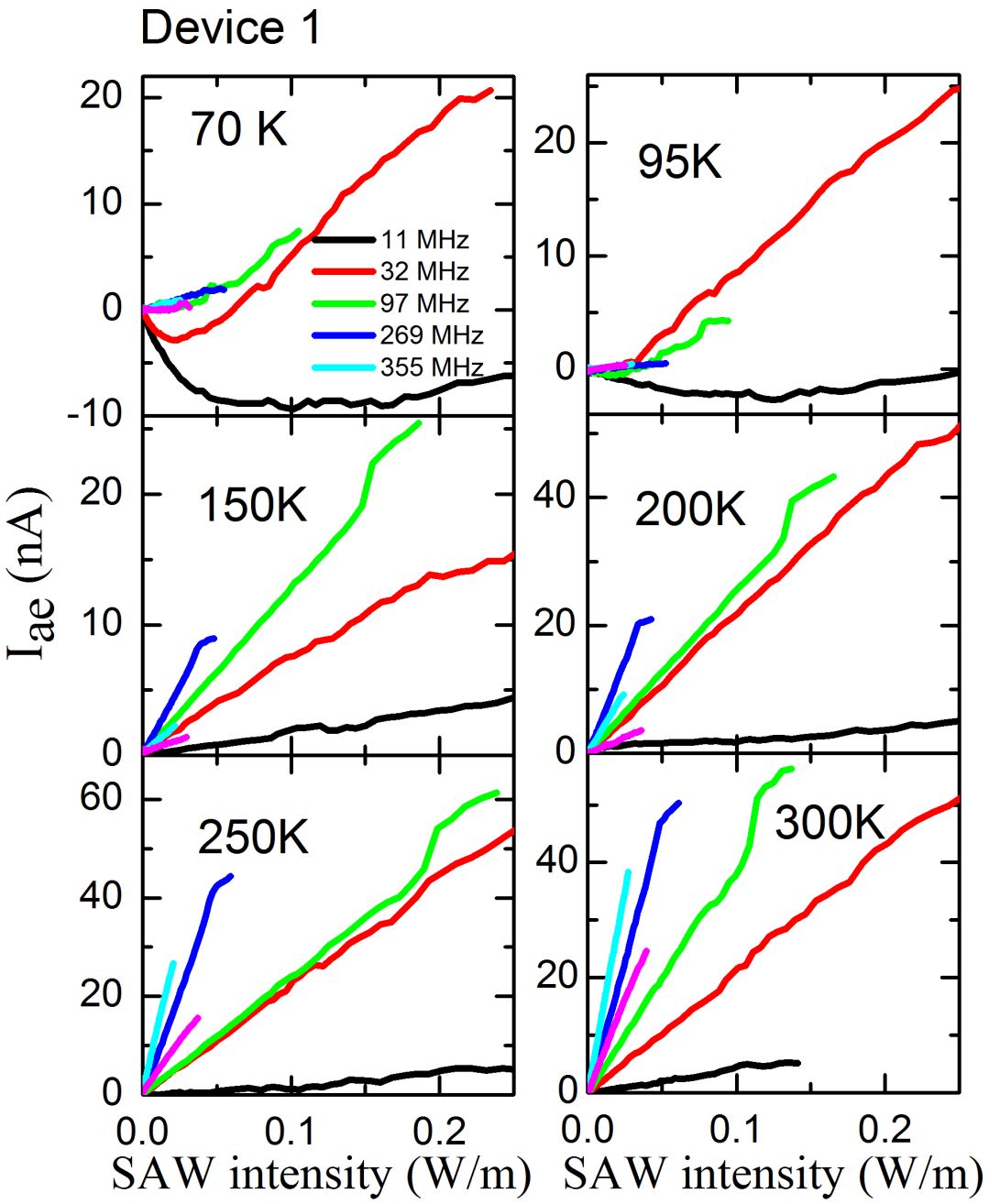


**Figure 6.3** The acoustoelectric current plotted as a function of SAW intensity at different temperatures.

It was observed that at high SAW frequencies, the measured acoustoelectric current decreases with decreasing temperature, but remains positive, which corresponds to the transport of holes. The current was also found to be directly proportional to the SAW intensity, which is in agreement with the interaction between the SAWs and carriers in graphene being described by the classical relaxation model (see Section 5.3.2). However, the measured acoustoelectric current does not depend linearly on the SAW intensity at low temperatures and SAW frequencies, and the direction of the acoustoelectric current is also observed to reverse under certain experimental conditions. For example, a negative acoustoelectric current was measured for the SAW at 11 MHz below 100 K, throughout the whole intensity range. As mentioned earlier, the SAW intensity measured for lower SAW frequencies was considerably low below 50 K. However, the peculiar behaviour observed for the 11 MHz and 32 MHz SAW at 70 K was also evident for 11 MHz below 50 K, as shown in Figure 6.4. In both the cases, a negative acoustoelectric current against the direction of propagation of SAWs was observed contrary to that measured for the other harmonics of SAWs.

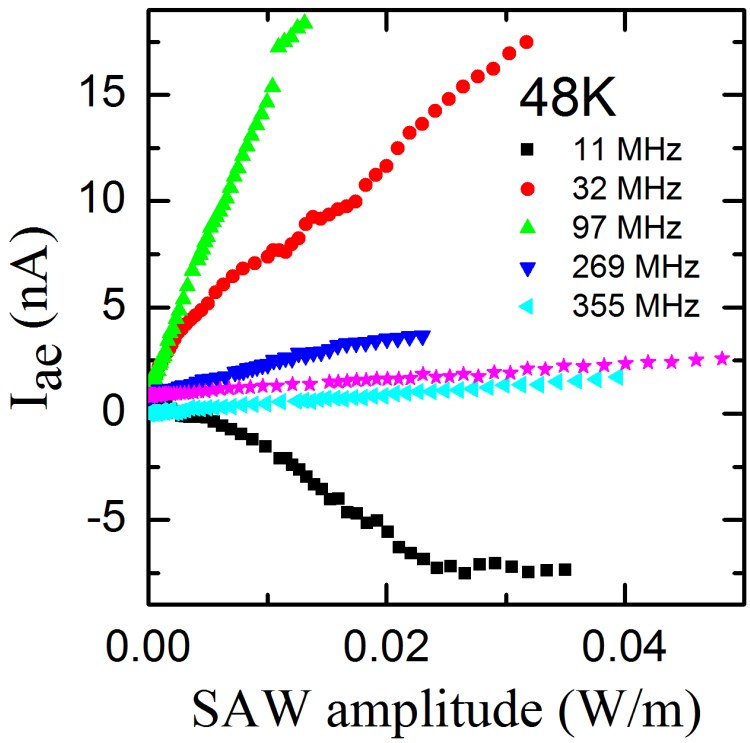


**Figure 6.4** The acoustoelectric current plotted as a function of SAW intensity at 48 K for Device1.

Let us first consider the behaviour of higher SAW frequencies at lower temperatures, as shown in Figure 6.3. The acoustoelectric current varies linearly as a function of SAW intensity, which shows that the simple classical relaxation model used to describe the room temperature behaviour for all SAW frequencies is valid for higher frequencies even at lower temperatures. For example, the plot of acoustoelectric current measured as a function of SAW intensity and temperature at 269 MHz, as shown in Figure 6.5, shows the similarity with its room temperature behaviour (at 300 K).

Although the acoustoelectric current measured in Device1 is much greater as compared to Device2, both the devices show a linear dependence on the SAW intensity. The poor performance of Device2 could be attributed to the lower attenuation coefficients, which is discussed later in this section. Nevertheless, in both the devices a positive acoustoelectric current was observed in the direction of SAW at all temperatures, although the size of the measured acoustoelectric current decreases with decreasing temperature (note that at temperatures below 95 K, the measured acoustoelectric current begins to increase slightly with decreasing temperature. However, at a SAW intensity of 0.02 $\mathrm{Wm}^{-1}$, for example in Device1, the measured current at 48 K is still approximately 35 times smaller than that measured at 300 K). The straight lines shown in Figure 6.5 are least square linear fits to the measured data, where we have taken the acoustoelectric current density $j$ (Refs. [130] and [129]) to be given by

$$j = -\frac{\mu F \Gamma}{v} \tag{6.1}$$

where $\mu$ is the carrier mobility, $F$ is the SAW intensity flux, $\Gamma$ is the attenuation coefficient, and $v$ is the velocity of the wave (approximately 4000 $\mathrm{ms}^{-1}$). In this model, the acoustoelectric current depends linearly upon the SAW intensity, as observed in the measured data, and the linear fitting was carried out using the mobility as the fitting parameter. The attenuation coefficients at each temperature were calculated using the measured values of the conductivity, and by assuming that the piezoelectric interaction between the SAWs and charge carriers is described by a simple classical relaxation model, such that

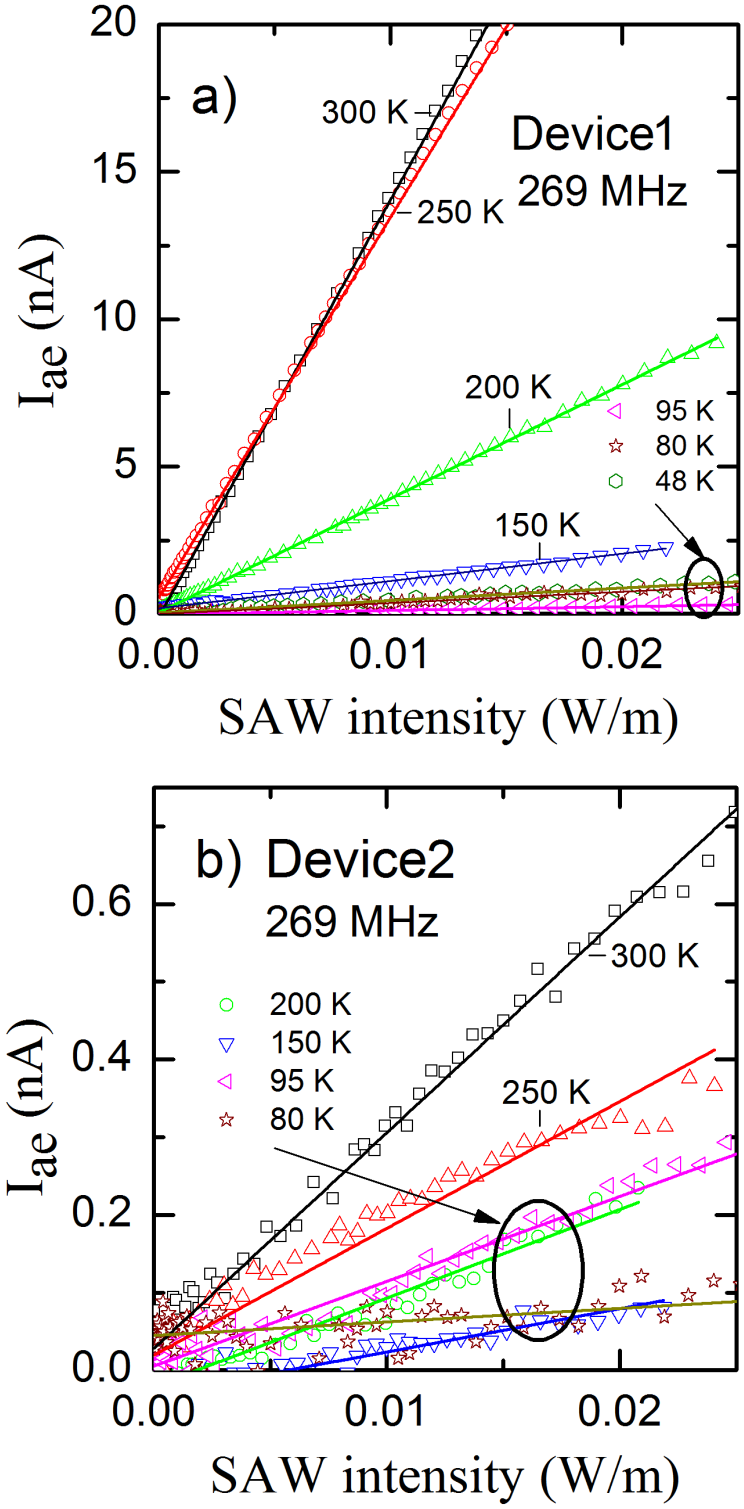


**Figure 6.5** The acoustoelectric current plotted as a function of SAW intensity at different temperatures for the SAW at 269 MHz. a) Device1 b) Device2.

the attenuation per unit length $\Gamma$ is a non-monotonic function of $\sigma_{2D}$, given by

$$\Gamma = K^2 \frac{\pi}{\lambda} \left[ \frac{\sigma_{2D}/\sigma_M}{1 + (\sigma_{2D}/\sigma_M)^2} \right] \tag{6.2}$$

where $\lambda$ is the SAW wavelength, and $K^2$ is the piezoelectric coupling coefficient (0.056 for lithium niobate [129]). The attenuation coefficient undergoes a maximum when $\sigma_{2D}$ is equal to the characteristic conductivity $\sigma_M$. The attenuation coefficient decreases rapidly as $\sigma_{2D}$ increases beyond $\sigma_M$. The measured conductivity, and calculated attenuation coefficient are plotted as a function of temperature in Figure 6.6(a) and 6.7(a) for Device1 and Device2 respectively.

The high conductivity of Device2 results in lower attenuation coefficients, *i.e.* less momentum was transferred to carriers in graphene, which results in low acoustoelectric current as observed in comparison to Device1. This demonstrates that the highly conductive samples are not necessarily good for acoustoelectric transport. The values of mobility obtained from the linear fitting of the measured data is plotted in Figure 6.6(b) and 6.7(b) for Device1 and Device2 respectively. The mobility obtained at room temperature is much smaller than the typical room temperature values ($\approx 1000$ cm$^2$V$^{-1}$s$^{-1}$) we have extracted from field effect characteristics measured on similar 3 mm $\times$ 3 mm devices [136], where CVD graphene was transferred into Si/$SiO_2$ substrates. However, as no other values of mobility in CVD graphene transferred onto lithium niobate have been reported, the difference in the mobilities could be due to the different properties of the substrate. In addition, although the measured linear dependence of the acoustoelectric current on SAW intensity and frequency [135], for high SAW frequencies or at high temperatures, suggests that the relatively simple model of the acoustoelectric transport described above can be used to describe the low temperature measurements for high frequency SAWs, it should be noted that the attenuation of the SAW by the charge carriers in the graphene is determined by the conductivity of the graphene on the scale of approximately one half of the SAW wavelength [131]. If the conduction path is inhomogeneous, the values of mobility obtained from this model will therefore depend on the SAW frequency used and may be different

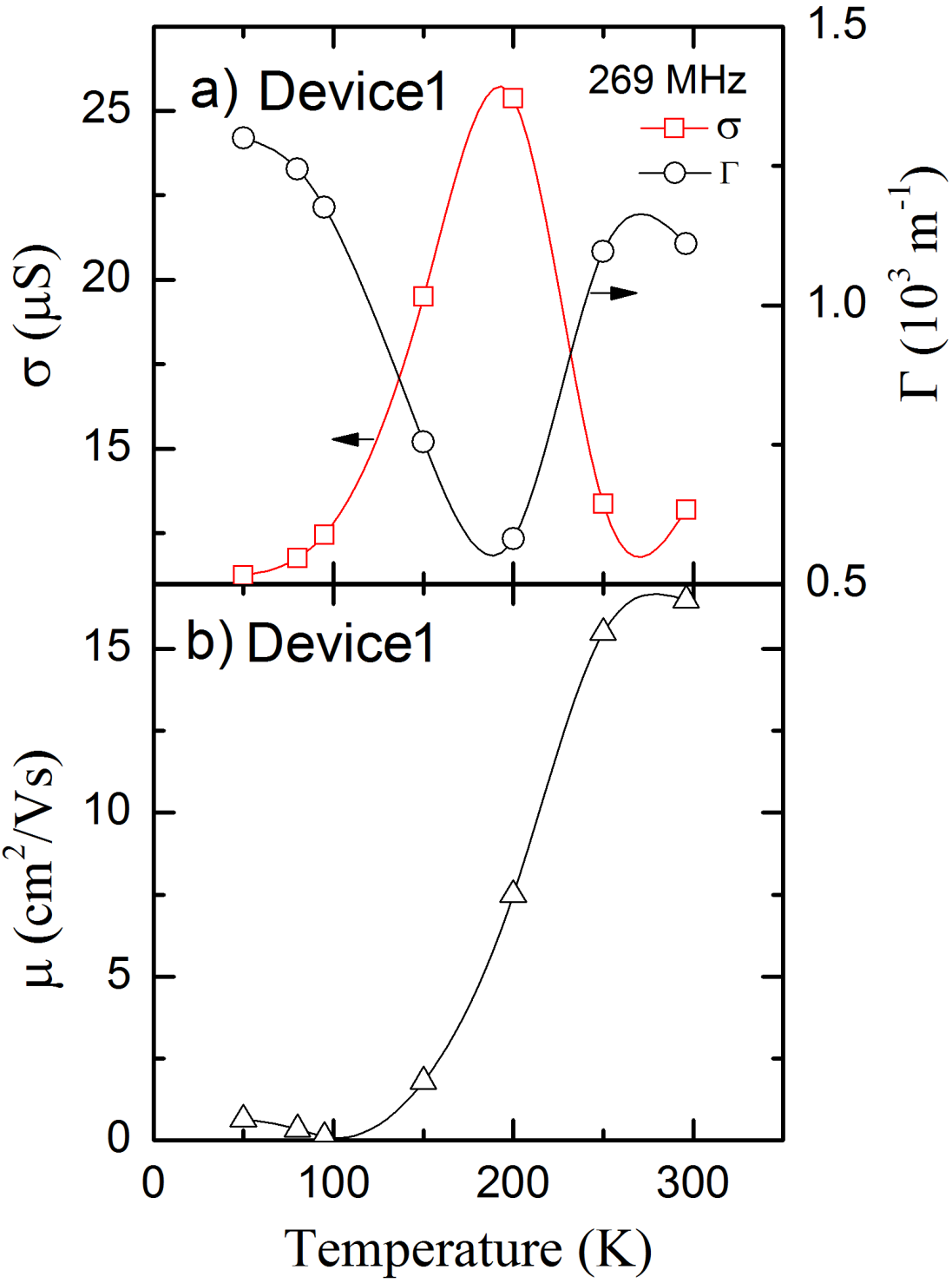


**Figure 6.6** (a) Measured conductivity of Device1 and the calculated values of attenuation coefficient plotted as a function of temperature. (b) Mobility, calculated from the linear fitting of Figure 6.5(a) plotted as a function of temperature.

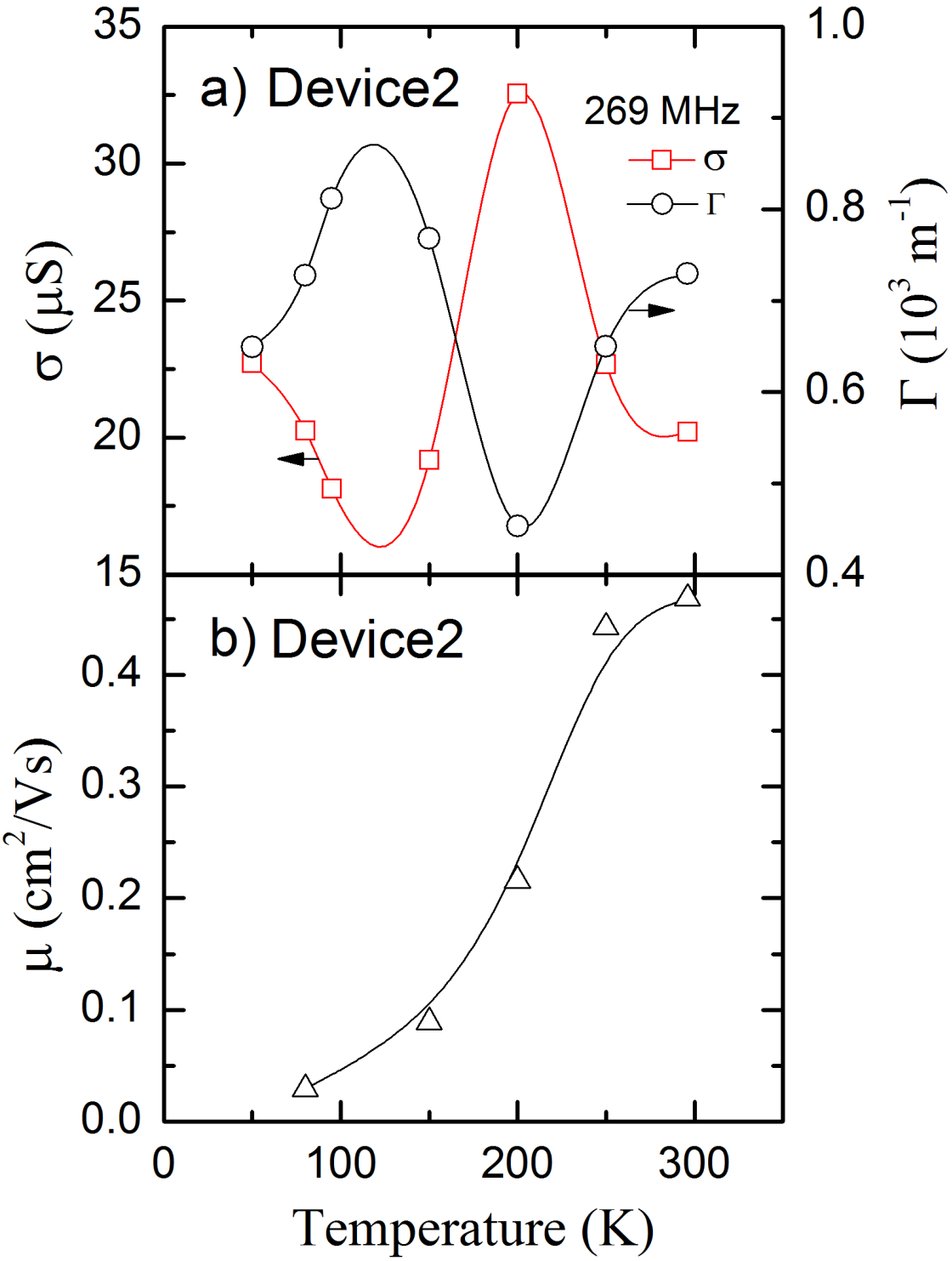


**Figure 6.7** (a) Measured conductivity of Device2 and the calculated values of attenuation coefficient plotted as a function of temperature. (b) Mobility, calculated from the linear fitting of Figure 6.5(b), plotted as a function of temperature.

to those obtained, for example, from a field effect measurement.

On initial cooling (at temperatures above 200 K), the results suggest that the mobility decreases, whereas the carrier concentration increases. One possible mechanism for this increase in the carrier concentration is the condensation of water, which is a known dopant [125], onto the surface of the sample as it is initially cooled in the relatively poor vacuum of the cold-finger cryostat. In addition, the conductivity of large-area CVD graphene is known to arise from many competing mechanisms [103][102]. Even at room temperature the conductivity of transferred CVD graphene is known to be spatially inhomogeneous, due to grain boundaries (as the graphene is polycrystalline), tears, wrinkles, and non-homogenous impurities [137][138] and the potential barriers associated with grain boundaries can lead to thermally activated conductivity [138, 139] and mobility [140]. At low temperature, this causes the graphene to tend towards insulating, as observed in Device1 (see Figure 6.6).

An Arrhenius plot of the extracted mobility values is plotted in Figure 6.8, where the dotted line is a linear fit to the values in the range of 100-300 K. The mobility can therefore be fitted well by an Arrhenius relation, with the mobility $\mu \propto \exp(-E_a/kT)$, where $E_a$ is the activation energy and $k$ is the Boltzmann constant, and an activation energy of 63 meV and 46 meV was obtained from the linear fit shown in Figure 6.8 for Device1 and Device2 respectively. Yazyev and Louie [139] calculated that the potential barriers associated with grain boundaries lie in the range of 0.3-1.4 eV, depending on the structure of the boundary. Song *et al.* [138] and Kumari *et al.* [140] obtained activation energies of 10 meV and 16.2 meV for the measured conductivity of CVD graphene, respectively, which they assigned to the effect of grain boundaries. Kumari *et al.* [140] also obtained a slightly higher value of activation energy, 18.8 meV, from the temperature dependence of the measured mobility. The value of activation energy obtained here is therefore consistent with the conductivity of the CVD graphene, on lithium niobate, also being strongly affected by the presence of grain boundaries.

At high temperatures, the acoustoelectric current measured at lower SAW frequencies also

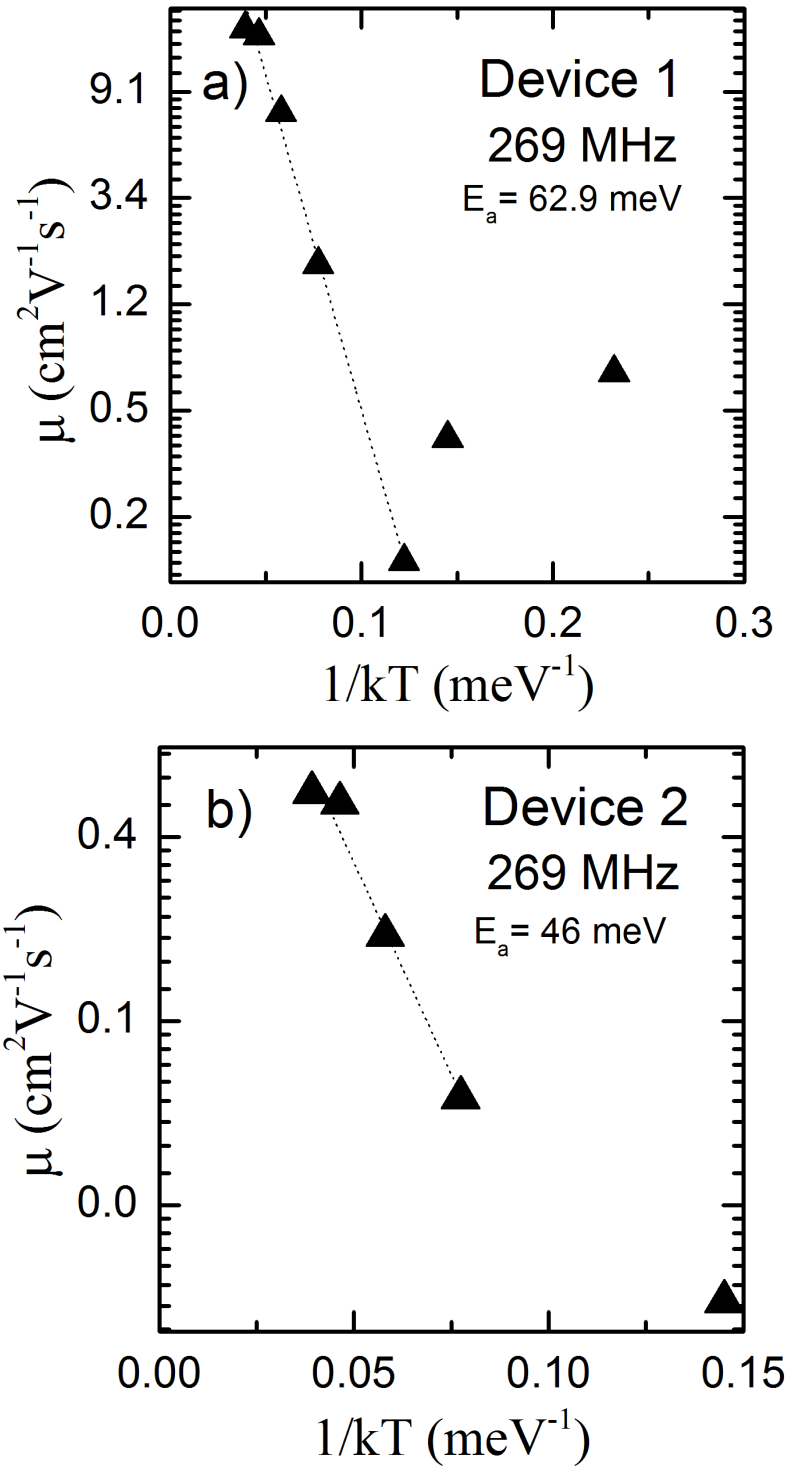


**Figure 6.8** The Arrhenius plots of the mobility calculated at different temperatures for the SAW at 269 MHz. a) Device1 b) Device2.

has a linear dependence on the SAW intensity, as shown for SAW frequencies of 32 MHz and 11 MHz in Figure 6.3, and a positive acoustoelectric current is also observed in the direction of the SAW propagation (note that to allow the results at different frequencies to be compared, we have corrected the SAW intensity using the measured response of the transducer at each temperature at each frequency). In this case, smaller values of mobility (6 $cm^2V^{-1}s^{-1}$ for 11 MHz at room temperature) have to be used to get good agreement between the calculated and measured values of acoustoelectric current.

However, the length ($\approx$2 $\mu$m) at which the 269 MHz SAW probes graphene is much smaller as compared to that probed by 11 MHz ($\approx$58 $\mu$m) SAW. At 269 MHz, the probed length scales are comparable to the size of a typical grain size in CVD graphene, which means that it encounters lesser grain boundaries than SAW at 11 MHz. The grain boundaries are known to be a strong limiting factor in the mobility of carriers in graphene [138], therefore the mobility extracted by low frequency SAWs (for example, 11 MHz) is lower in comparison. This sensitivity of the SAWs of different wavelengths to the effect of grain boundaries can be used to probe the conductivity of the graphene over different length scales.

At low temperatures, the measured intensity dependence of the acoustoelectric current at low SAW frequencies is markedly different from that obtained at high frequencies. For SAW frequencies of 32 MHz and 11 MHz, the measured acoustoelectric current no longer shows the simple linear dependence on the SAW intensity as observed at higher temperatures and higher SAW frequencies. Furthermore, at 32 MHz, below 80 K and for SAW intensities below approximately 0.065 $Wm^{-1}$, the current reverses direction, indicating that overall the SAW is now transporting more electrons than holes. At 11 MHz, this effect is much more pronounced and for all temperatures below 100 K a negative current is observed at low values of SAW intensity. At low carrier densities and temperatures, the conductivity of the graphene becomes strongly affected by the formation of a large number of electron-hole charge puddles, and an important component of the conductivity will be the percolation of thermally excited "activated" carriers over potential fluctuations in disorder sites (charge puddles or grain boundaries) [103]. The low frequency SAW is again

likely to be much more sensitive to this due to the relative large length scales over which it probes the conductivity. Moreover, in this regime the SAW itself could influence the conductivity of the graphene, through the transfer of momentum to the carriers leading to the observed non-linear dependence of the current on the SAW intensity. One scenario in which a reversal of the current direction could occur is when the doping of the graphene is due to relatively widely spaced, but high density, puddles of holes superimposed on a relatively low density, but more uniform, density of electrons. Recently, intrinsic spontaneous polarization of hexagonal SiC has been proposed as a possible mechanism of the doping of quasi free-standing graphene on the surface of SiC [141]. Lithium niobate is highly pyroelectric and on cooling it is possible that induced surface charge could cause n-type doping [142]. However, much more work is required to understand this, and also how the use of a different substrate influences the doping of the graphene caused by water.

## 6.3 Summary

The temperature dependence of acoustoelectric charge transport in large-area CVD graphene was investigated. It was observed that at high SAW frequencies, the measured acoustoelectric current decreases with decreasing temperature, but remains positive, which corresponds to the transport of holes. The measured current is also proportional to the SAW intensity over the temperature range studied (48-300 K), consistent with the attenuation of the SAW by the carriers in the graphene being described using a simple classical relaxation model. The measured acoustoelectric current at low SAW frequencies at high temperatures is also directly proportional to the SAW intensity, but in this case much lower values of mobility have to be used to give good qualitative agreement between the measured and calculated values of the acoustoelectric current. This suggests that the use of different frequency SAWs with associated different wavelengths allows the conductivity of the graphene to be probed over different length scales. At low temperatures and SAW frequencies, the measured acoustoelectric current no longer exhibits a simple linear dependence on the SAW intensity, and the direction of the acoustoelectric current is observed to reverse under certain experimental conditions. This might be due to the interaction be-

tween the SAW and the complex conductivity landscape of the graphene in a percolation regime. However, much more work is required to understand this fully.

# 7 Voltage-controlled Modulation

## 7.1 Introduction

The novel properties of graphene, including ambi polar charge transport and linear energy dispersion, can be realised on a substrate with the help of a gate bias, which has led to an intensive research in the field of graphene field effect transistor structures in the last decade [15][71][81][143]. The controlled transport of charge carriers has been predicted to be of utmost importance in various applications, for example, in metrology, quantum computation, and quantum cryptography [144]. Talyanski *et al.* [3] have observed the transport of single electron delivering quantized acoustoelectric current through a GaAs/AlGaAs one-dimensional channel, which demonstrates the possibility of defining accurate current standards. Foden *et al.* [145] have proposed an alternative method for the generation of single-photon states, required for secure optical communications using quantum cryptography techniques, in a quasi one-dimensional system defined on 2DEG with the help of SAWs. Such devices demand immense control on the type and movement of charge carriers. The electrostatic modulation possible in graphene with the help of a gate bias, combined with the piezoelectric fields associated with the SAWs, could be an ideal system to realise such control and manipulation of charge carriers. The field-effect study of graphene on lithium niobate, along with the acoustoelectric current dependence on the SAW variables becomes very important in this regard. In addition, the wide range of applications of SAW devices in the communication systems could hugely benefit from the modulation of acoustic velocity achievable by tuning the conductivity of graphene. SAW delay lines with a tunable wave velocity may have useful applications such as adaptable

sensors and phase shifters.

Unlike $Si/SiO_2$, the voltage controlled conductance modulation in graphene is not possible through a back gate in lithium niobate. An alternate way to achieve this is by using a top gate configuration with an ion-gel as a dielectric. The devices described in this chapter were fabricated in this manner, where the dielectric was prepared by dissolving 0.024 g of lithium perchlorate and 0.2 g of poly ethyl oxide (PEO) in 10 ml methanol (for details see section 4.5). It was carefully drop-cast on graphene and the metal contacts (source, drain and gate). It was noticed that the lithium perchlorate acts as an etchant for aluminum transducers. Moreover, the varying RF voltage in the transducers may also induce carriers in graphene. Therefore, any contact between the ion-gel and transducers was avoided. The schematic of typical gated devices discussed in this chapter is shown in Figure 7.1.

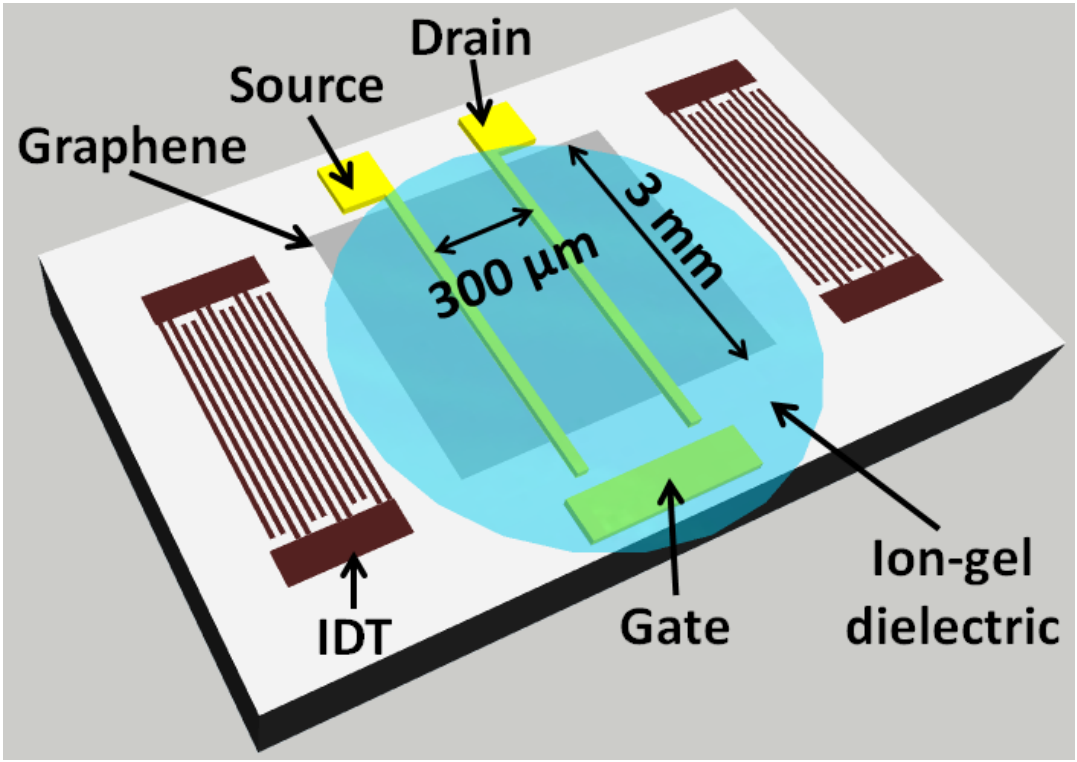


**Figure 7.1** The schematic of a typical gated device showing the drop-cast ion-gel on graphene and metal contacts. The source drain contacts are 300 $\mu$m apart.

This chapter describes the electric field effect of graphene transferred onto lithium niobate. The transfer characteristics of three gated devices, DeviceG1, DeviceG2 and DeviceG3

(see Table 4.1), studied in this chapter are given in section 7.2. Section 7.3 describes the change in acoustoelectric current measured as a function of SAW intensity at different gate voltages, which exhibits a linear dependence consistent with the simple classical relaxation model. A change in the direction of acoustoelectric current as a function of gate bias demonstrates the dragging of both electrons and holes along with the SAWs. The acoustoelectric current measured at different SAW frequencies indicates that the conductivity of graphene can be probed at different length scales by SAWs of different wavelengths. Section 7.4 describes the voltage-controlled modulation of the velocity and amplitude of the SAW, achieved by tuning the conductivity of graphene through the top gate, which is reported for the first time in graphene/lithium niobate hybrid system. The summary of the chapter is given in section 7.6.

## 7.2 Electrical Characteristics

### 7.2.1 DeviceG1

The field-effect characteristics of DeviceG1 are shown in Figure 7.2, where each data point is an average of a hundred observations. The source-drain contacts are 300 $\mu$m apart and the measurements were done at room temperature in an evacuated chamber ($3.6\times10^{-6}$ mbar). A source-drain current $I_{SD}$=10 nA was applied during the field-effect measurement, where a small leakage current of the order of 10 pA was noticed between the source and gate. The inset of Figure 7.2 shows the I-V characteristic of the device measured at zero gate bias. The $I_{SD}$ current was found to increase non-linearly with the increasing source-drain voltage $V_{SD}$, which could be due to the charge transfer between the adsorbed water molecules and graphene. The conductivity of graphene was modulated through the gate voltage, which was varied in a small range (-3 to 2 V) to prevent the breakdown of the ion-gel due to any possible electrochemical reactions [146]. The high capacitance of the ion-gel enabled the resistance modulation in graphene even in the small range of gate voltage used. The maximum in the resistance, which corresponds to the charge neutrality point (CNP) was observed at $V_g$=-1 V. The lack of a sharp peak in

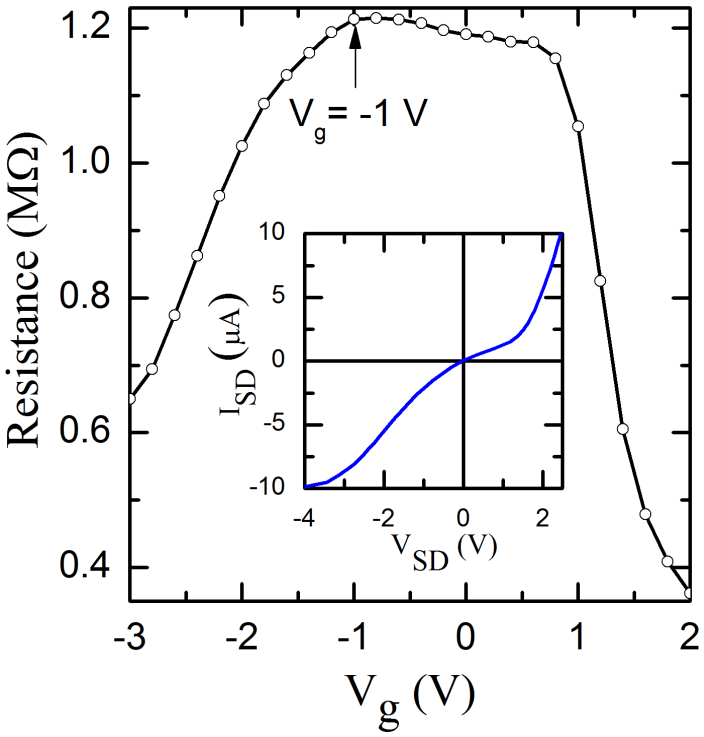


**Figure 7.2** The electric field effect characteristics of DeviceG1 at $I_{SD}$=10 nA, with the charge neutrality point observed at $V_g$=-1 V. The inset shows the I-V characteristics of the device at zero gate bias.

the resistance curve could be attributed to the electrostatic inhomogeneity introduced by the charge puddles [147], which is common in large-area CVD graphene. The field effect mobility $\mu$ for the electrons and holes induced, was obtained using

$$\mu = \frac{1}{C}\frac{\Delta\sigma}{\Delta V_g} \tag{7.1}$$

where $\sigma$ is the sheet conductivity of graphene, and $C$ is the gate capacitance. The capacitance of the dielectric, as calculated by Chakraborty *et al.* for a similar configuration, is assumed to be of the order of $\approx$1 $\mu$Fcm$^{-2}$ [148]. The electron and hole mobility thus calculated are 2 cm$^2$V$^{-1}$s$^{-1}$ and 0.6 cm$^2$V$^{-1}$s$^{-1}$ respectively. The mobility values are low compared to the typical values obtained for Si/$SiO_2$ substrate, which could be attributed to the different properties of lithium niobate. However, more importantly we observe the Dirac peak and show the transition of graphene from n-doped to p-doped by applying a small gate voltage, which is sufficient to determine the carrier type transported by the SAW at different gate bias.

### 7.2.2 DeviceG2

The field effect characteristics of DeviceG2 are shown in Figure 7.3. The CNP in this device was observed at $V_g$=1.8 V, which corresponds to the p-doped nature of graphene at zero gate bias contrary to DeviceG1. It may be due to the different ambient conditions at the point of fabrication of these two devices. The ambient humidity, for example, has been reported to have a significant contribution in changing the conductivity of graphene-oxide films [149]. The inset in Figure 7.3 shows the I-V characteristics of the device as a function of gate bias, which tends to Ohmic behaviour for positive gate biases. A hole mobility of 1.2 $cm^2V^{-1}s^{-1}$ is obtained in this device.

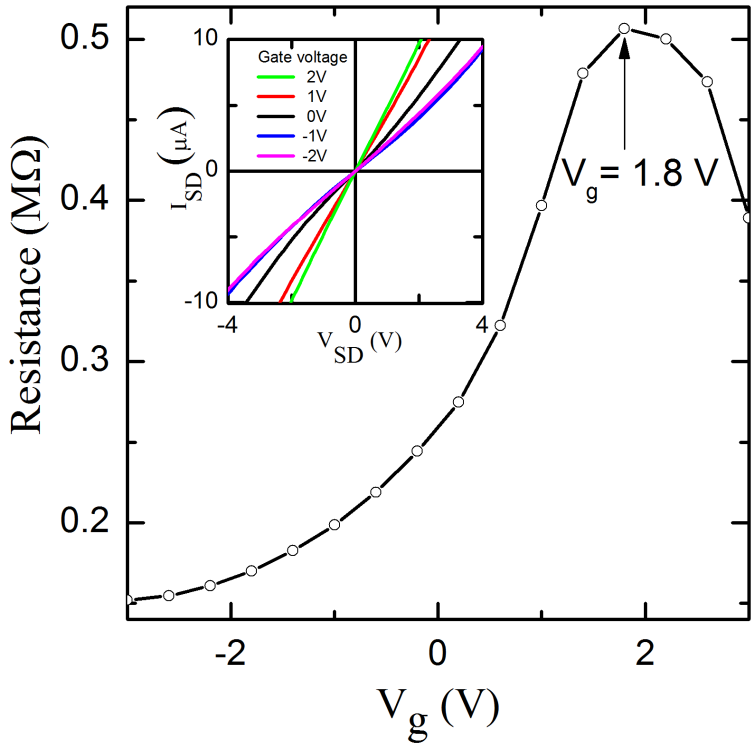


**Figure 7.3** The electric field effect characteristic of DeviceG2 at $I_{SD}$=10 nA, with the CNP observed at $V_g$=1.8 V. The inset shows the I-V characteristic of the device as a function of gate bias.

### 7.2.3 DeviceG3

The field effect characteristics characteristics of DeviceG3 are shown in Figure 7.4. The gate bias was increased in small intervals (0.05 V) to accurately trace the position of the CNP, which was observed at $V_g$=0.75 V. The maximum resistance measured in this device (1.15 MΩ) is twice that in DeviceG2 (0.50 MΩ), and a relatively sharp peak was observed at the Dirac point. The asymmetric nature of the curve on either side of the Dirac point is observed in DeviceG1 and DeviceG2 as well, but is most apparent in this device (see Figure 7.4). This asymmetry could be attributed to the electrostatic inhomogeneity (in the form of residues and charge puddles) in graphene. The electron and hole mobility calculated from the slope of the curve are 7.3 $cm^2V^{-1}s^{-1}$ and 5.3 $cm^2V^{-1}s^{-1}$ respectively, which is consistent with the hole mobility obtained from the fitting of simple classical relaxation model to the experimental observations at room temperature (see section 5.3.2).

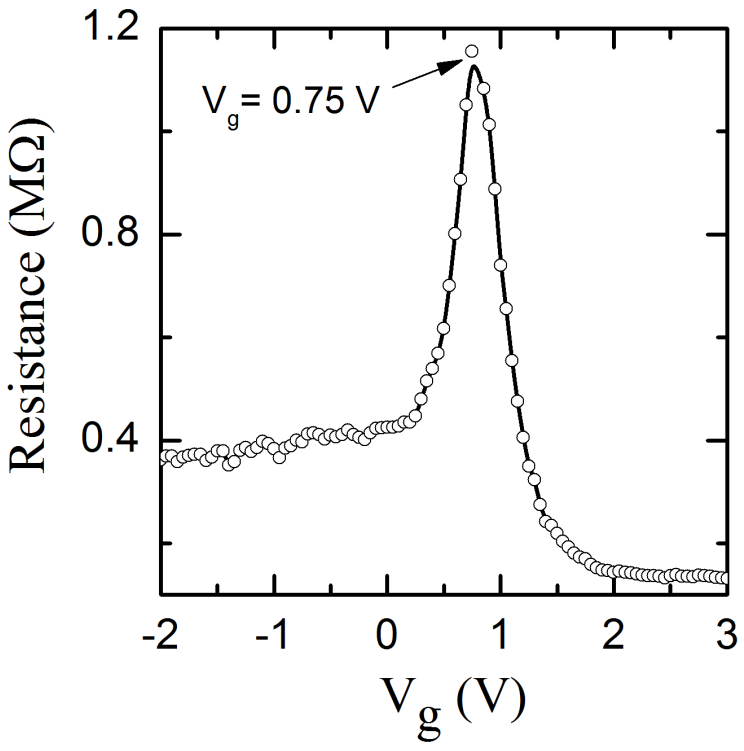


**Figure 7.4** The electric field effect characteristic of DeviceG3 at $I_{SD}$=10 nA, where the CNP is observed at $V_g$=0.75 V.

## 7.3 Acoustoelectric Current Modulation

In DeviceG1, the acoustoelectric current is measured for the SAW at 32 MHz as a function of time, as shown in Figure 7.5, which demonstrates the switch in its direction at different gate biases.

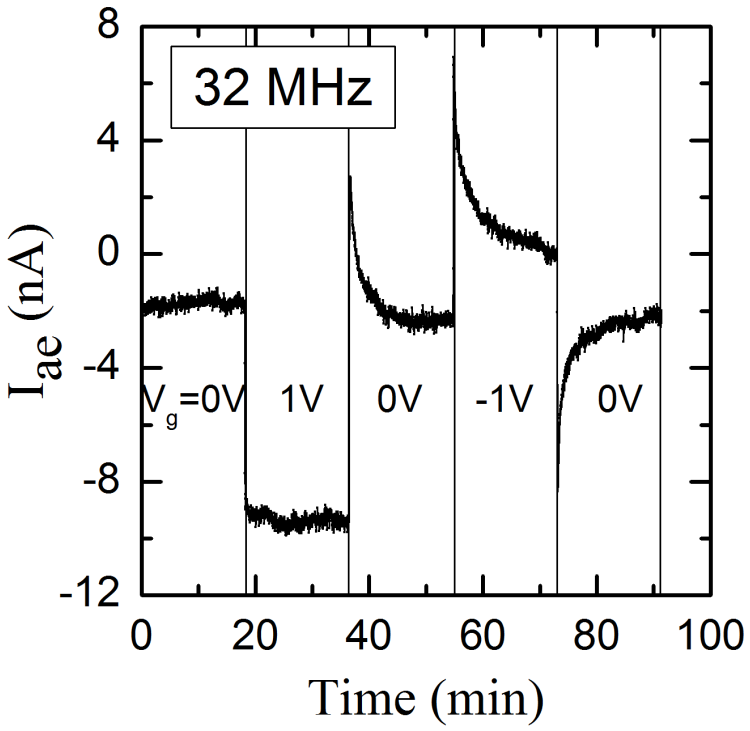


**Figure 7.5** The acoustoelectric current measured in DeviceG1, at 32 MHz for an applied RF power of 20 dBm, is plotted as a function of time at different gate biases.

The negative acoustoelectric current measured at $V_g$=0 V indicates the transport of electrons with the SAW, which is consistent with the n-doped nature of graphene as observed from the field effect characteristics (see Figure 7.2). The acoustoelectric current becomes more negative with the introduction of further electrons through a positive gate bias ($V_g$=1 V). Similarly, a negative gate bias implies the introduction of holes in graphene, which gives rise to a positive acoustoelectric current. As the bias becomes more negative, the CNP is realised at $V_g$=-1 V, where the carrier density of electrons and holes are equal. Therefore, the acoustoelectric current due to the transport of electrons and holes should cancel each other. In Figure 7.5, it is shown that the measured acoustoelectric current

approaches zero slowly at $V_g$=-1 V, the decay observed could be attributed to the slow response of the dielectric. The time constant for the charging and discharging of the capacitor, which takes place through the diffusion process, is measured to be approximately 300 s and 200 s respectively. This time required for the charge stabilisation in the dielectric was taken into account while sweeping the gate voltage.

Figure 7.6(a) shows the acoustoelectric current plotted as a function of SAW intensity at different gate biases for the 32 MHz SAW. The linear dependence of the acoustoelectric current shows that the simple classical relaxation model can be used to describe the interaction of SAWs with the modulated carries in graphene. An acoustoelectric current as high as 12 nA was measured at positive and negative gate biases. A positive gate bias induces electrons in graphene, therefore the negative acoustoelectric current measured at $V_g$=1 V along the propagation of SAW is definitely due to the transport of electrons along the SAW. A large negative bias would similarly ensure the transport of only holes in graphene along the SAW, as observed for $V_g$=-1.5 V and -2 V. The absence of acoustoelectric current measured at $V_g$=-1 V (see Figure 7.6(a)) illustrates the transport of equal density of electrons and holes, which is realised at the CNP.

The same acoustoelectric measurements performed for the SAW at 355 MHz in the same device are plotted in Figure 7.6(b). The small current observed at this frequency is due to the relatively low SAW intensity measured at higher frequencies. The acoustoelectric current measured at 355 MHz is two orders of magnitude smaller than that at 32 MHz. In Figure 7.6(b), the measured current was negative for higher negative biases, contrary to that at 32 MHz. The wavelength corresponding to the 355 MHz SAW ($\approx$11 $\mu$m) is an order of magnitude smaller than at 32 MHz ($\approx$ 125 $\mu$m), therefore it is probing graphene at a different length scale. The inhomogeneity of the sample means that local high density electron puddles in an otherwise uniform distribution of holes induced by the gate bias are possible. The long wavelength SAWs may not be able to detect such electron puddles, but the small wavelength SAWs are more sensitive to it. It should be noted that the electrostatic inhomogeneity due to the charge puddles means that the carriers induced is not directly proportional to the gate voltage applied. Therefore, the mobility of charge

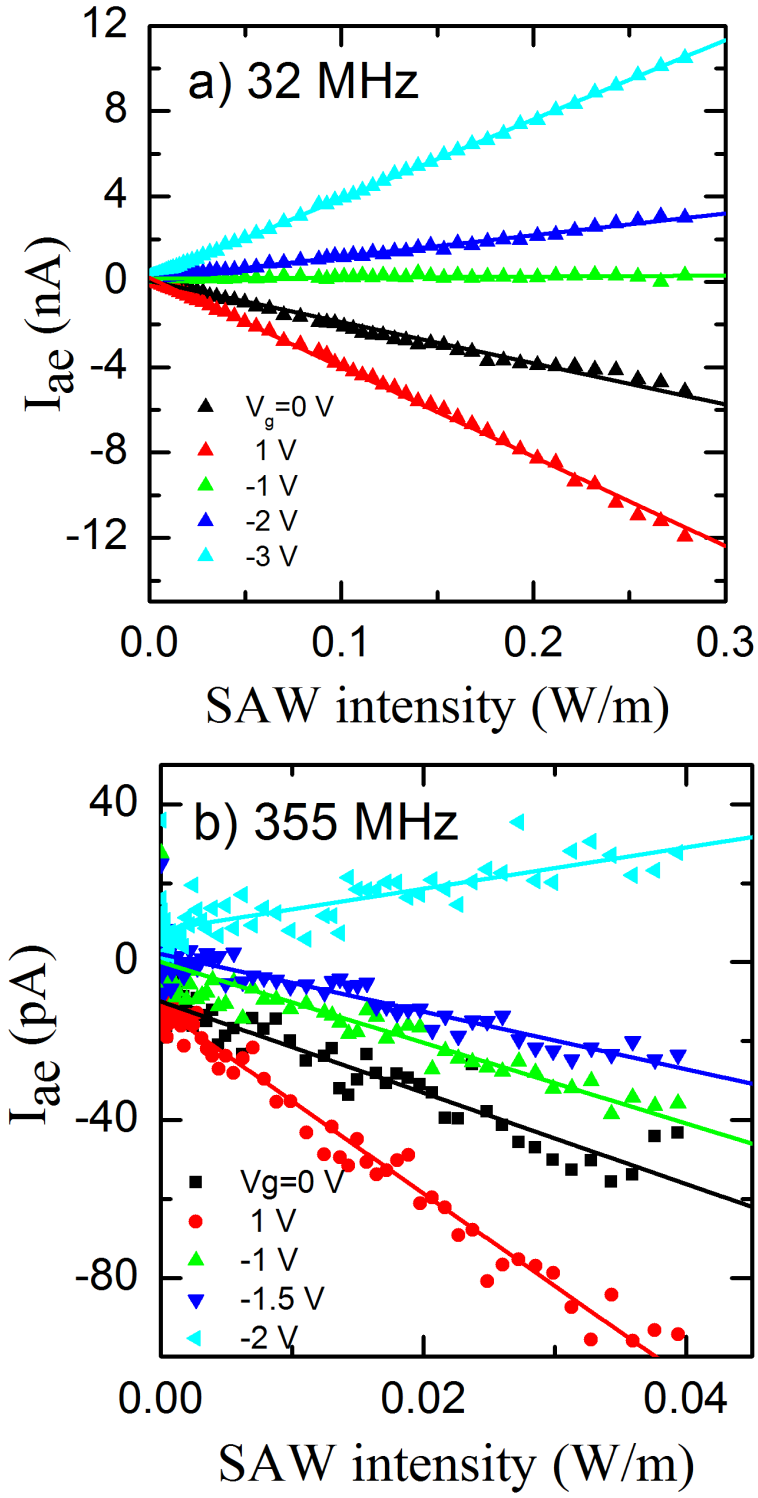


**Figure 7.6** The acoustoelectric current measured in DeviceG1 is plotted as a function of SAW intensity and gate bias for a SAW frequency of (a) 32 MHz and (b) 355 MHz. The straight lines correspond to the linear fit of the measured data.

carriers is expected to be a function of gate voltage. The mobility values obtained from the linear fit of the measured data in Figure 7.6 are plotted as a function of gate voltage in Figure 7.7, where the negative (positive) values refers to the mobility of holes (electrons).

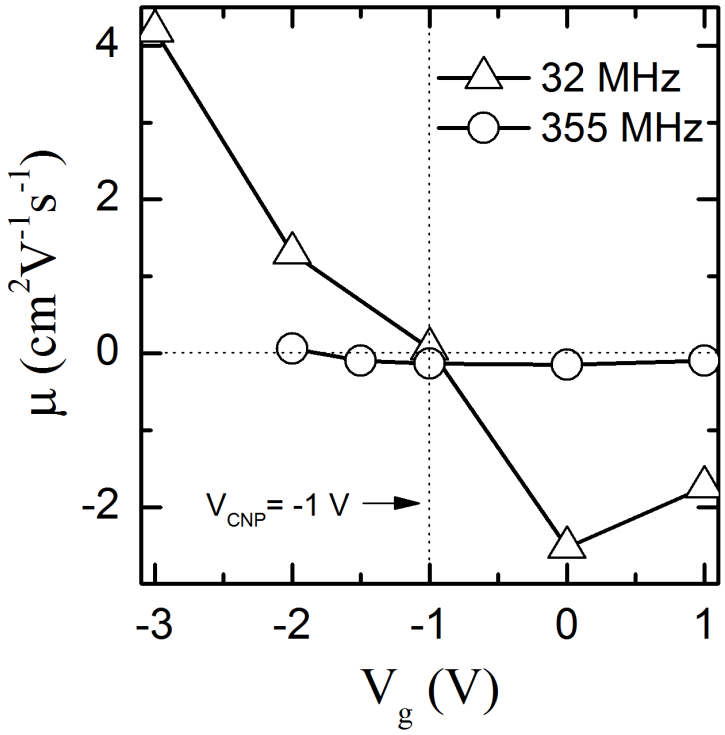


**Figure 7.7** Mobility extracted from the acoustoelectric measurements at 32 MHz and 355 MHz is plotted as a function of gate bias for DeviceG1.

Similar behaviour was observed in DeviceG3. A relatively small acoustoelectric current was observed in DeviceG2, which was of the order of the leakage current between the source and gate electrodes (10 pA) measured in it. Therefore, it was not used for acoustoelectric measurements. It should be noted that in case of DeviceG1 no leakage current was measured for the voltages used in the measurement.

## 7.4 Amplitude and Velocity Modulation

The acoustoelectric interaction of the SAWs with graphene carriers can be used to modulate the amplitude and velocity of the SAW by tuning the conductivity of graphene. The

amplitude and velocity of the SAW at 11 MHz is measured as a function of gate voltage in DeviceG2 and DeviceG3. The transducers on the lithium niobate define an acoustic path length of 5.2 mm, where the SAW interacts with graphene such that the attenuation $\Gamma$ and velocity shift $\Delta v/v$ of the SAW can be given by

$$\Gamma = K^2 \frac{\pi}{\lambda} \left[ \frac{\sigma_{2D}/\sigma_M}{1 + (\sigma_{2D}/\sigma_M)^2} \right] \tag{7.2}$$

$$\frac{\Delta v}{v} = \frac{K^2}{2} \left[ \frac{1}{1 + (\sigma_{2D}/\sigma_M)^2} \right] \tag{7.3}$$

where $K^2$ is the piezoelectric coupling coefficient, $\lambda$ is the SAW wavelength, $v$ is the SAW velocity, $\sigma_{2D}$ is the sheet conductivity of 2DEG and $\sigma_M$ is the characteristic conductivity of lithium niobate, which is discussed in section 2.3.2. The amplitude and velocity modulation achieved in DeviceG2 by tuning the conductivity of graphene as a function of gate bias, is shown in Figure 7.8. The amplitude of the SAW increases on either side of the CNP, observed at $V_g$=1.8 V. This is consistent with the simple classical relaxation model, where the attenuation attains a maximum at $\sigma_{2D} = \sigma_M$ (see Figure 2.8). The minimum sheet conductivity of graphene $\sigma_{2D}$=1.98 M$\Omega^{-1}$ measured at the CNP is still larger than the characteristic conductivity $\sigma_M$=1.25 M$\Omega^{-1}$ of lithium niobate, which means that the peak in attenuation is not reached in this device. However, this implies that as the conductivity decreases the attenuation should increase monotonously. More attenuation means smaller SAW amplitude, which attains a minimum at CNP, as observed in Figure 7.8. The phase difference $\Delta\phi$ measured between the phase of the SAW and the reference signal can be converted to the time delay $\Delta t$ as

$$\Delta\phi = \omega \Delta t \tag{7.4}$$

where $\omega$ is the frequency of the SAW. The velocity shift $\Delta v/v$ can be obtained from the following relation:

$$\frac{\Delta v}{v} = \frac{\Delta t}{t - \Delta t} \approx \frac{\Delta t}{t} \qquad\qquad t >> \Delta t \tag{7.5}$$

From Equation (7.3), the velocity shift due to the interaction with the carriers in graphene should increase with decreasing conductivity. The velocity shift measured at 11 MHz

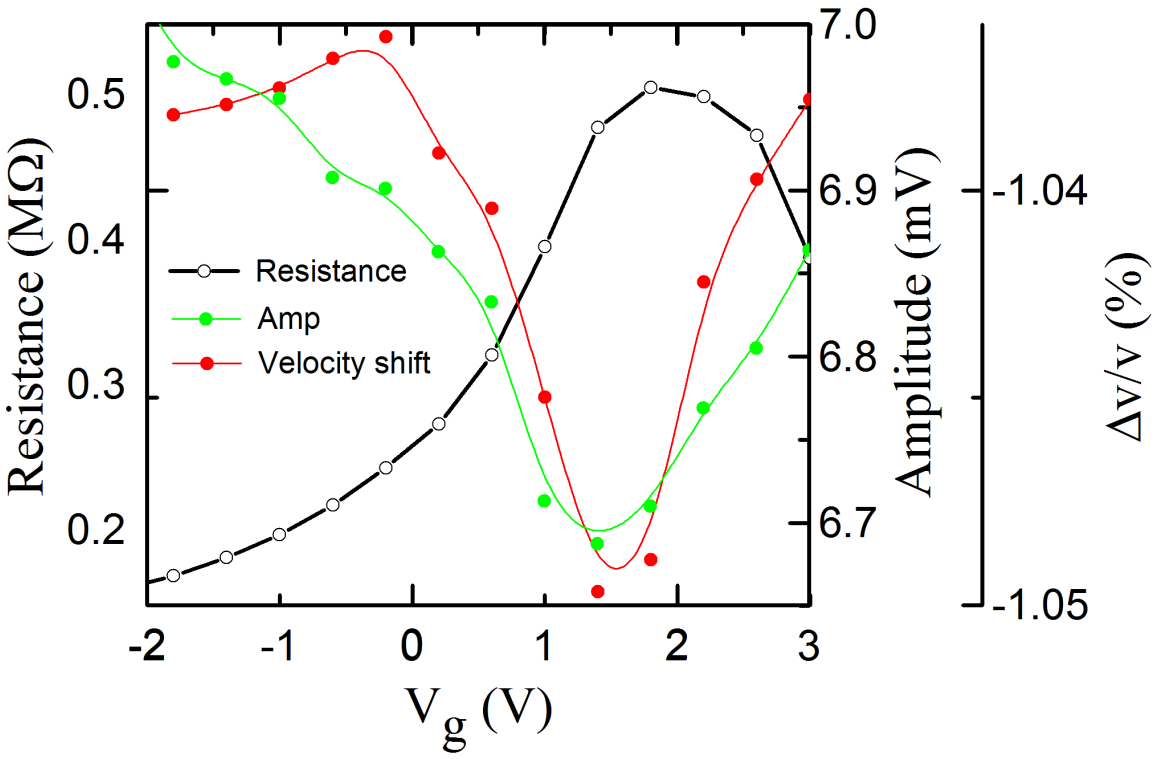


**Figure 7.8** The resistance of graphene, SAW amplitude and velocity shift plotted as a function of gate bias for DeviceG2.

is plotted as a function of gate bias in Figure 7.8, which is consistent with the simple classical relaxation model. A maximum velocity shift of 0.015% is obtained in this device (DeviceG1), which is an order of magnitude smaller than the voltage tunable phase shifters demonstrated by Zhu *et al.* [150] on a hybrid system with a semiconducting/piezoelectric dual layer of zinc oxide (ZnO) deposited on r-plane sapphire substrate. However, a distinct advantage of the voltage-controlled phase shifter demonstrated here is the operation at much lower voltages as compared to other phase shifters based on lithium niobate, which operates at very high voltages (≈6 kV) to achieve a velocity shift of 1% [151].

The resistance, amplitude and velocity shift measured as a function of gate voltage in DeviceG3 is shown in Figure 7.9. Measurements similar to DeviceG2 performed on DeviceG3, resulted in a maximum velocity shift of 0.5%. It is more than an order of magnitude (≈30 times) improvement in the velocity shift achieved in DeviceG2, on the other hand the SAW amplitude modulation was similar to DeviceG2. It should be noted that both the attenuation and velocity shift changes slowly when the conductivity of graphene is either

too small or too large compared to the characteristic conductivity of lithium niobate (see Figure 2.8), which means that a huge improvement ($\approx$ 25 times) in the performance of the these voltage-controlled phase shifters could be expected for graphene, where the sheet conductivity $\sigma_{2D}$ can be engineered to be closer to $\sigma_M$ and ten times resistance modulation is plausible.

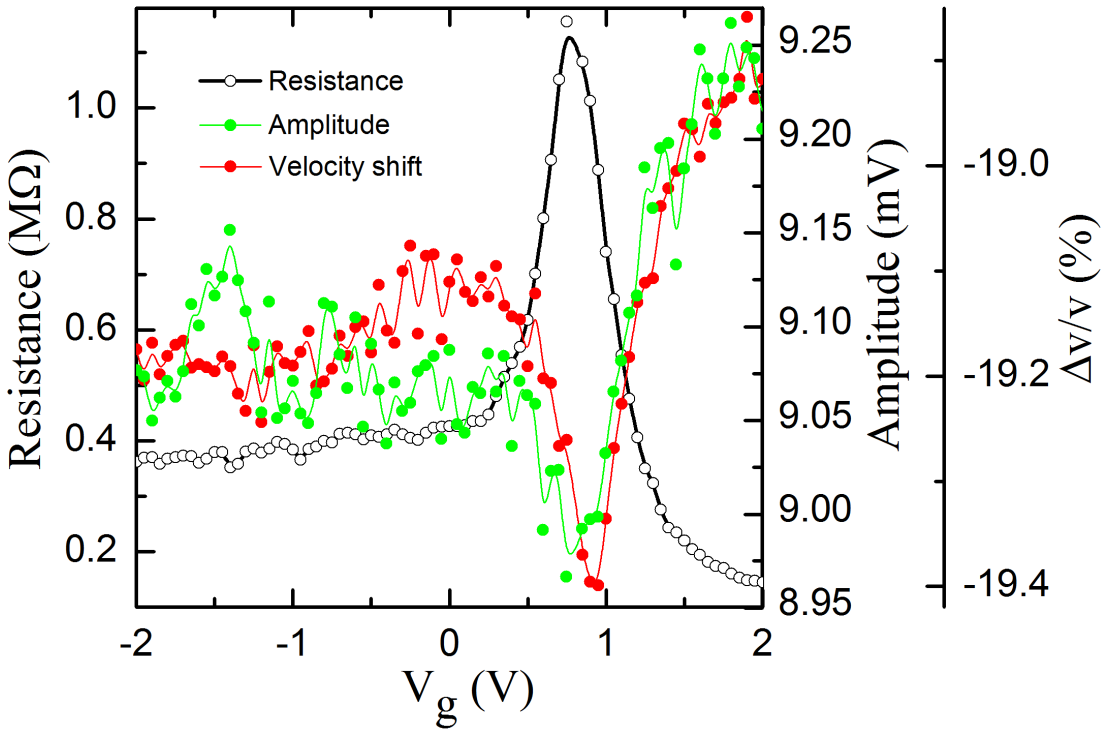


**Figure 7.9** The resistance of graphene, SAW amplitude and velocity shift plotted as a function of gate bias for DeviceG3.

## 7.5 Simultaneous Measurement of Acoustoelectric Current, SAW Amplitude and Velocity Modulation

It was noticed that the position of the Dirac peak in all the devices was continuously shifting with the evacuation of the measurement chamber. Therefore, the chamber was evacuated to $3.6\times10^{-6}$ mbar and isolated from the vacuum pump to steady the position of Dirac peak, which allowed a detailed measurement in the vicinity of Dirac peak. The simultaneous measurements of acoustoelectric current, SAW amplitude and velocity mod-

ulation were done in DeviceG3. The acoustoelectric current for the SAW at 11 MHz and 32 MHz was measured as a function of gate voltage, as shown in Figure 7.10.

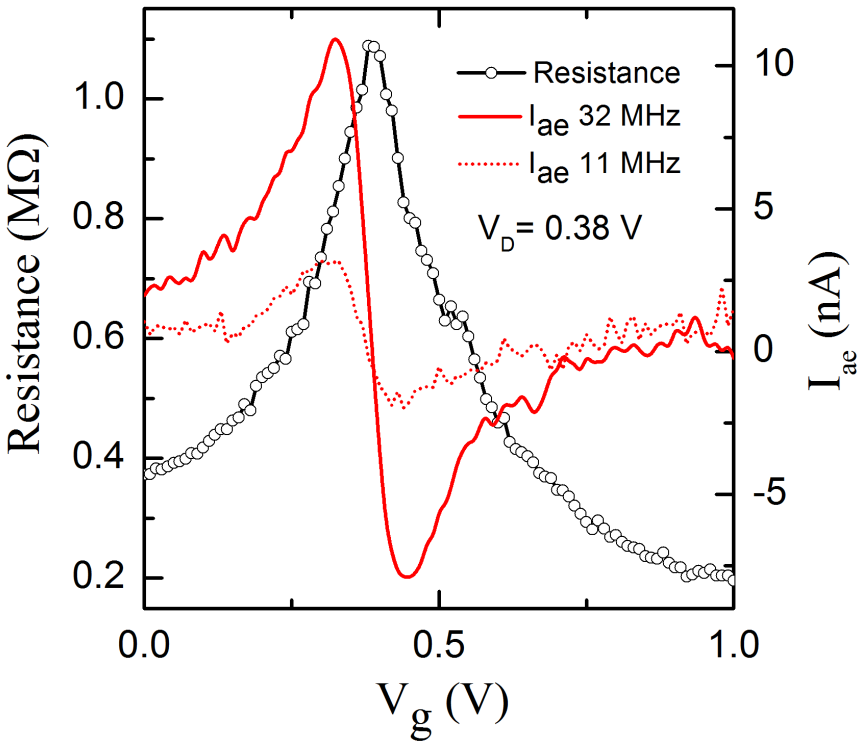


**Figure 7.10** The resistance of graphene, and the acoustoelectric current measured at 11 MHz and 32 MHz plotted as a function of gate bias for DeviceG3.

The resistance modulation obtained before this measurement is also given in Figure 7.10 as a reference. A positive acoustoelectric current consistent with the transport of holes is measured for 32 MHz SAW at zero gate bias, which initially increases with the increase in conductivity controlled by the gate voltage. As the conductivity approaches the CNP, the density of states available for carriers (electrons and holes) becomes fewer and fewer before eventually going to zero. As a consequence, the acoustoelectric current starts decreasing and eventually vanishes at the CNP. An increase in gate voltage beyond the CNP induces electrons in graphene, which results in a negative acoustoelectric current as illustrated in Figure 7.10. Similar behaviour is observed for the SAW at 11 MHz with relatively small acoustoelectric current.

The SAW amplitude and velocity shift measured simultaneously with the acoustoelectric

current at 11 MHz is shown in Figure 7.11. The observations are in accordance with the simple classical relaxation model, as explained in the previous section.

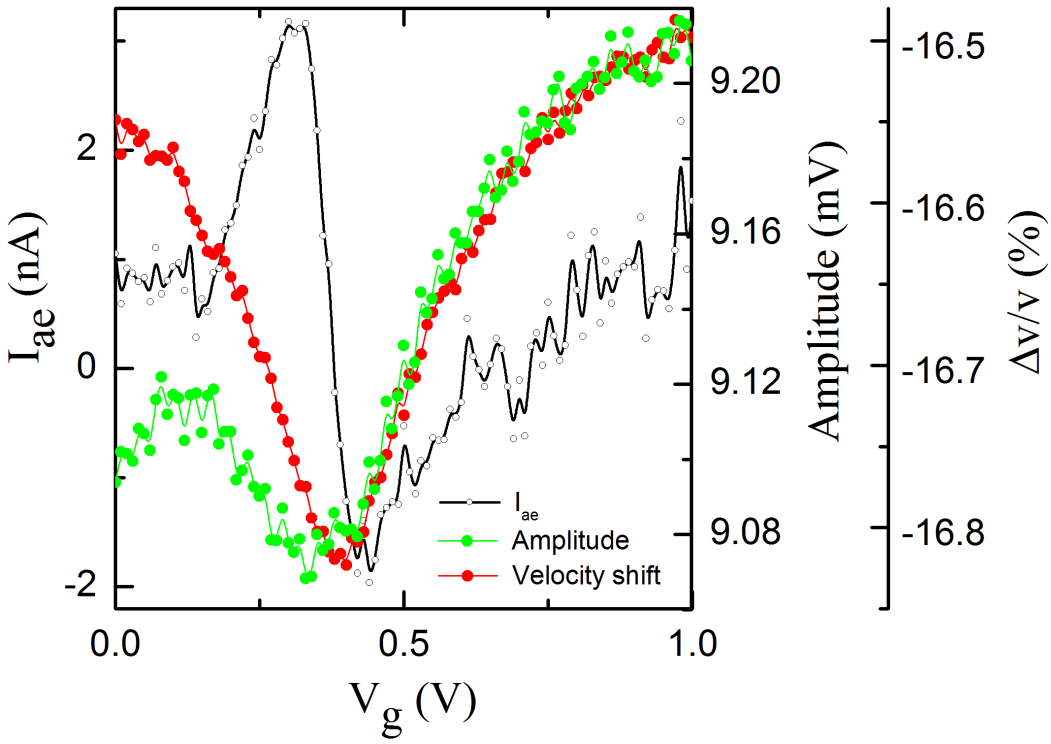


**Figure 7.11** The acoustoelectric current, SAW amplitude and velocity shift measured simultaneously at 11 MHz is plotted as a function of gate bias for DeviceG3.

The SAW amplitude measured for 32 MHz SAW was an order of magnitude smaller than that at 11 MHz and due to the large fluctuations observed, the data was not reproducible. It should be noted that the acoustoelectric current measured for 32 MHz was greater than 11 MHz and was consistent. It is possible that the high acoustoelectric current is due to the large attenuation of the wave, which results in small SAW amplitude. It would require further investigation to comment on it. However, the simultaneous measurements of the SAW variables and the acoustoelectric current demonstrates the feasibility of devices with multi-purpose applications such as voltage-controlled phase shifters with gas sensing abilities.

## 7.6 Summary

In conclusion, we have studied the electric field effect characteristics of graphene transferred onto lithium niobate, observing the CNP for the first time in such hybrid systems. The use of ion-gel dielectric as the top-gate proves very effective in inducing a large carrier density in graphene at small gate voltages, although the slow response time of the devices is a drawback. The absence of the acoustoelectric current at the CNP is observed, indicating the transport of an equal number of electrons and holes with the SAW at this point. The linear dependence of the acoustoelectric current measured as a function of SAW intensity shows that the interaction of graphene carriers and SAW can be described using a simple classical relaxation model. The positive (negative) acoustoelectric current corresponding to the transport of holes (electrons) also suggests that the acoustoelectric measurements are sufficient to determine the type of doping in graphene. The different type of doping observed for the same gate bias at 32 MHz and 355 MHz SAW is indicative of the different length scales at which the SAW probes graphene, where the large wavelengths probes the uniform average carrier density and small wavelengths are more sensitive to the local high density charge puddles. Also, the amplitude and velocity modulation is achieved by modulating the conductivity of graphene. A voltage-controlled SAW phase (velocity) shifter is demonstrated with a maximum velocity shift of 0.5 %, which is comparable to other phase shifters but works at much smaller voltage biases. A significant improvement in the performance of these phase shifters can be expected if the conductivity of graphene can be engineered to be closer to the characteristic conductivity of lithium niobate.

# 8 Conclusions and Future Prospects

The work presented in this thesis is focused on the interaction of large-area graphene with SAWs. SAWs have previously been used as a contact-less probing method for low-dimensional systems, for example, quantum dots, nanowires and 2DEGs. Graphene is one such 2DEG system, which has invoked a lot of interest owing to its special properties like ambi polar transport, large surface area, *etc.* To date relatively little work has been reported on the SAW interaction with large-area graphene, which has been addressed in this work. The devices described here, which are more than an order of magnitude bigger than previously been studied, were fabricated using e-beam lithography in a clean-room environment and measured using a Keithley sourcemeter and LeCroy oscilloscope. A macroscopic acoustoelectric current has been demonstrated for the first time in such a large-area graphene device. The measurement of acoustoelectric current at room and low temperatures revealed some interesting properties about the transport of electrons and holes with SAWs, and low-temperature measurements highlighted the important role played by charge inhomogeneity in defining the direction of acoustoelectric current in large-are graphene. The behaviour of the acoustoelectric current at different SAW frequencies also shows that the conductivity of graphene can be probed at different length scales by SAWs of different wavelengths. Devices with top gates were fabricated to study the electric field-effect of graphene on lithium niobate. The mobility of carriers in graphene on lithium niobate has been reported for the first time here. The modulation of the conductivity of graphene was used to demonstrate a tunable voltage-controlled phase shifter that is operational even at low voltages, which is first of its kind in the system studied.

This chapter summarises the results obtained from all the experiments conducted in this

thesis and proposes some suggestions for future work. The acoustoelectric current measured as a function of SAW intensity for different frequencies at room temperature is summarised in section 8.1. The conclusion of the measurement of acoustoelectric current as a function of temperature is given in section 8.2. The field-effect study of graphene on lithium niobate along with the tunable phase-shifter, demonstrated in the previous chapter, is briefly summarised in section 8.3.

## 8.1 Macroscopic Acoustoelectric Transport

The acoustoelectric current was measured as a function of SAW intensity and frequency for a hybrid system of large-area CVD graphene transferred onto lithium niobate. The SAWs were used to transport holes over long distances ($\approx 0.8$ mm), giving rise to a positive macroscopic acoustoelectric current. A simplified Weinreich relation, given for a special case of 2DEG with a shorted geometry in the absence of a magnetic field, was used to describe the acoustoelectric current, which was measured to be directly proportional to the SAW intensity and frequency. The frequency dependence comes from the attenuation, which is a linear function of frequency at a given sheet conductivity of the 2DEG. A loss in momentum of the SAWs due to the interaction with the carriers in graphene leads to the attenuation and velocity shift of the wave, which is explained by a relatively simple classical relaxation model. The model predicts a peak in the attenuation at a certain sheet conductivity of graphene, which is noticed by measuring the change in acoustoelectric current at different conductivities in two devices. A mobility of 8 $\mathrm{cm^2V^{-1}s^{-1}}$ was obtained for the hole transport from fitting the model to the experimental observations, which is reported for the first time for graphene on lithium niobate. The key point of this work is the demonstration of the acoustoelectric current flowing over macroscopic distances, which opens the gate for a wide range of applications in graphene-based SAW devices.

## 8.2 Temperature Dependence

The acoustoelectric charge transport was measured as a function of temperature and SAW intensity at different frequencies for the same set of devices used for room temperature measurements. The acoustoelectric current for high SAW frequencies was measured to be positive over the whole temperature range (50-300 K) studied, which is consistent with the transport of holes on p-doped graphene. A linear dependence of the acoustoelectric current on SAW intensity was observed, as predicted by the simple classical relaxation model. For lower SAW frequencies, the acoustoelectric current was positive at higher temperatures, but relatively much lower values of mobility had to be used to get good agreement between the measured and calculated values. The difference in mobilities obtained at different SAW frequencies suggests that the conductivity of the graphene can be probed over different length scales by using SAWs of different wavelengths. The activation energy of 60 meV was obtained from the Arrhenius plot, which is consistent with the conductivity of CVD-graphene being strongly affected by the grain boundaries. The interaction of the SAW with the complex conductivity landscape of graphene in a percolation regime is evident from the switch in the direction of acoustoelectric current observed for lower SAW frequencies, at low SAW intensities and temperatures.

## 8.3 Voltage Control

Devices with a top-gate were fabricated to study the field-effect of graphene on lithium niobate. The high capacitance of the dielectric used made it possible to observe the charge neutrality point at low voltages, which is reported for the first time in such a hybrid system. The equal density of electrons and holes at the charge neutrality point was illustrated in the measurement of acoustoelectric current, where the transport of equal number of electrons and holes with the SAW led to net zero current. The simple classical relaxation model was valid throughout the resistance modulation in graphene. The positive (negative) acoustoelectric current measured at negative (positive) gate bias

corresponds to the transport of holes (electrons). This suggests that the measurement of acoustoelectric current is sufficient to determine the type of doping in graphene. By tuning the conductivity of graphene, a voltage-controlled SAW phase-shifter was demonstrated with a velocity shift of approximately 0.5 %, operational at much lower voltages compared to other phase-shifters. These tunable phase-shifters are reported for the first time in a graphene/lithium niobate hybrid system. The velocity shift and attenuation measured in all the devices were consistent with the predictions of the simple classical relaxation model.

## 8.4 Suggestions for Future Work

The work presented in this thesis highlights the possibility of probing graphene at different length scales using SAWs of different wavelengths, in addition to the demonstration of large-area graphene-based SAW devices and voltage-controlled phase-shifters. One of the limitations of the devices studied here is the lack of four probes to determine the actual conductivity of graphene. It is difficult to estimate the sheet conductivity of large-area CVD graphene because of the inhomogeneity due to grain boundaries, cracks, wrinkles, and impurities in the form of residues and charge puddles. The simple classical relaxation model does not take the inhomogeneity of graphene into account. Therefore, further work is required to extend the model to qualitatively estimate the effect of impurities on SAW propagation.

The graphene-based SAW devices demonstrated here may be exposed to different gases, chemicals, enzymes, *etc.* to study the effect of mass loading and its efficiency as a chemical and biological sensor. Similar investigation for graphene-quartz devices by our group is reported in *Applied Physics Letters*, **103**, 063110 (2013), where the mass loading of argon and water vapour was studied. The mass sensitivity of SAWs, along with the electrical properties of graphene including its selective absorption, could be developed for sensitive mass and chemical detection. A theoretical study of the interaction of the surface phonons of lithium niobate with the graphene carriers could be useful in this regard.

The ability of graphene to absorb light from the ultra-violet to terahertz range can be used to generate excited carriers. The acoustoelectric current being sensitive to the carriers in graphene can detect it, therefore can be developed as a photodetector. Initial attempts by our group to measure the photo-response in graphene, when excited by blue and red light emitting diodes (LEDs), through the acoustoelectric current is published in *Applied Physics Letters*, **106**, 133107 (2015). Further investigation is required to develop it as a wide band-width photodetector. In addition, the operating band-width of traditional photodetectors are limited by the lifetime of the photogenerated carriers. The ability of SAWs to separate the carriers by trapping them in its potential minima and maxima could be used to dilate the recombination time of photo-excited carriers, resulting in photodetectors with wider operating band-width.

The voltage-controlled phase-shifter demonstrated here may experience a huge improvement (at least 25 %) in velocity shift achieved if the sheet conductivity of graphene can be engineered to be closer to the characteristic conductivity of lithium niobate, and a ten times modulation in its conductivity can be attained. A smaller, well-defined uniform area of relatively clean graphene may be used for this purpose. Moreover, the electrical properties of graphene such as mobility, are strongly affected by lithium niobate. One way to minimise this is to study a hybrid system where graphene sandwiched between two single-layer boron nitride sheets, is transferred on lithium niobate.

It may also be interesting to study the charge trapped in the potential landscape of a standing SAW, which would create an oscillating charge perpendicular to the direction of propagation of SAWs. SAWs of large wavelengths with efficient reflectors can be employed to create standing waves, a custom design of reflectors might be needed for it. The exotic properties of graphene especially the Klein tunneling may be observed in such devices. Further theoretical work would be required to develop a model to explain the oscillating carriers with SAWs.

# Bibliography


[1] D. Morgan. Surface acoustic wave filter. *Academic Press, San Diego*, 1985.

[2] J. M. Shilton and D. R. Mace. On the acoustoelectric current in a one-dimensional channel. *Journal of Physics: Condensed Matter*, 8(24):L337, 1996.

[3] V. Talyanskii, J. Shilton, M. Pepper, C. Smith, C. Ford, E. Linfield, D. Ritchie, and G. Jones. Single-electron transport in a one-dimensional channel by high-frequency surface acoustic waves. *Physical Review B*, 56(23):15180, 1997.

[4] A. K. Geim and K. S. Novoselov. The rise of graphene. *Nature Materials*, 6(3):183, 2007.

[5] A. H. C. Neto, F. Guinea, N. M. R. Peres, K. S. Novoselov, and A. K. Geim. The electronic properties of graphene. *Reviews of Modern Physics*, 81(1):109, 2009.

[6] P. Blake, E. W. Hill, A. H. C. Neto, K. S. Novoselov, D. Jiang, R. Yang, T. J. Booth, and A. K. Geim. Making graphene visible. *Applied Physics Letters*, 91(6):063124, 2007.

[7] A. C. Ferrari, J. C. Meyer, V. Scardaci, C. Casiraghi, M. Lazzeri, F. Mauri, S. Piscanec, D. Jiang, K. S. Novoselov, S. Roth, and A. K. Geim. Raman spectrum of graphene and graphene layers. *Physical Review Letters*, 97(18):187401, 2006.

[8] G. R. Nash, S. J. Bending, M. Boero, M. Riek, and K. Eberl. Surface-acoustic-wave absorption by quantum-dot arrays. *Physical Review B*, 59(11):7649, 1999.

[9] G. R. Nash, S. J. Bending, M Boero, P. Grambow, K. Eberl, and Y. Kershaw. Anisotropic surface acoustic wave scattering in quantum-wire arrays. *Physical Review B*, 54(12):R8337, 1996.

[10] A. Wixforth, J. Kotthaus, and G. Weimann. Quantum oscillations in the surface-acoustic-wave attenuation caused by a two-dimensional electron system. *Physical Review Letters*, 56(19):2104, 1986.

[11] A. Wixforth, J. Scriba, M. Wassermeier, J. Kotthaus, G. Weimann, and W. Schlapp. Surface acoustic waves on GaAs/$Al_xGa_{1-x}As$ heterostructures. *Physical Review B*, 40(11):7874, 1989.

[12] C. Rocke, S. Zimmermann, A. Wixforth, J. Kotthaus, G. Böhm, and G. Weimann. Acoustically driven storage of light in a quantum well. *Physical Review Letters*, 78(21):4099, 1997.

[13] B. Reulet, A. Kasumov, M. Kociak, R. Deblock, I. Khodos, Y. Gorbatov, V. Volkov, C. Journet, and H. Bouchiat. Acoustoelectric effects in carbon nanotubes. *Physical Review Letters*, 85(13):2829, 2000.

[14] M. Buitelaar, V. Kashcheyevs, P. Leek, V. Talyanskii, C. Smith, D. Anderson, G. Jones, J. Wei, and D. Cobden. Adiabatic charge pumping in carbon nanotube quantum dots. *Physical Review Letters*, 101(12):126803, 2008.

[15] K. S. Novoselov, A. K. Geim, S. V. Morozov, D. Jiang, Y. Zhang, S. V. Dubonos, I. V. Grigorieva, and A. A. Firsov. Electric field effect in atomically thin carbon films. *Science*, 306(5696):666, 2004.

[16] J. S. Bunch, A. M. van der Zande, S. S. Verbridge, I. W. Frank, D. M. Tanenbaum, J. M. Parpia, H. G. Craighead, and P. L. McEuen. Electromechanical resonators from graphene sheets. *Science*, 315(5811):490, 2007.

[17] I. W. Frank, D. M. Tanenbaum, A. M. van der Zande, and P. L. McEuen. Mechanical

properties of suspended graphene sheets. *Journal of Vacuum Science & Technology B*, 25(6):2558, 2007.

[18] X. Du, I. Skachko, A. Barker, and E. Y. Andrei. Approaching ballistic transport in suspended graphene. *Nature Nanotechnology*, 3(8):491, 2008.

[19] C. Mattevi, H. Kim, and M. Chhowalla. A review of chemical vapour deposition of graphene on copper. *Journal of Materials Chemistry*, 21(10):3324, 2011.

[20] K. S. Novoselov, V. I. Fal'ko, L. Colombo, P. R. Gellert, M. G. Schwab, and K. Kim. A roadmap for graphene. *Nature*, 490(7419):192, 2012.

[21] P. Thalmeier, B. Dóra, and K. Ziegler. Surface acoustic wave propagation in graphene. *Physical Review B*, 81(4):041409, 2010.

[22] S. H. Zhang and W. Xu. Absorption of surface acoustic waves by graphene. *AIP Advances*, 1(2):022146, 2011.

[23] R. Arsat, M. Breedon, M. Shafiei, P. G. Spizziri, S. Gilje, R. B. Kaner, K. Kalantarzadeh, and W. Wlodarski. Graphene-like nano-sheets for surface acoustic wave gas sensor applications. *Chemical Physics Letters*, 467(4-6):344, 2009.

[24] V. Miseikis, J. E. Cunningham, K. Saeed, R. O'Rorke, and A. G. Davies. Acoustically induced current flow in graphene. *Applied Physics Letters*, 100(13):133105, 2012.

[25] L. Rayleigh. On waves propagated along the plane surface of an elastic solid. *Proceedings of The London Mathematical Society*, 17(1):4, 1885.

[26] R. M. White and F. W. Voltmer. Direct piezoelectric coupling to surface elastic waves. *Applied Physics Letters*, 7(12):314, 1965.

[27] D. P. Morgan. Surface acoustic wave devices and applications. *Ultrasonics*, 11(3):121, 1973.

[28] R. H. Tancrell and M. G. Holland. Acoustic surface wave filters. *Proceedings of the IEEE*, 5(25):657, 1971.

[29] H. Sabine and P. Cole. Surface acoustic waves in communications engineering. *Ultrasonics*, 9(2):103, 1971.

[30] P. Dineva, D. Gross, R. Müller, and T. Rangelov. Dynamic fracture of piezoelectric materials: Solution of time-harmonic problems via BIEM. *Springer International, Cham*, 2014.

[31] J. G. Gualtieri. Piezoelectric materials for acoustic wave applications. *IEEE Transactions on Ultrasonics, Ferroelectrics, and Frequency Control*, 41(1):53, 1994.

[32] M. B. Schulz. Temperature dependence of surface acoustic wave velocity on $\alpha$ quartz. *Journal of Applied Physics*, 41(7):2755, 1970.

[33] E. F. Whitehead, E. M. Chick, L. Bandhu, L. M. Lawton, and G. R. Nash. Gas loading of graphene-quartz surface acoustic wave devices. *Applied Physics Letters*, 103(6):063110, 2013.

[34] J. C. Crabb, J. D. Maines, and N. R. Ogg. Surface-wave diffraction on $LiNbO_3$. *Electronics Letters*, 7(10):253, 1971.

[35] R. H. Parmenter. The acoustoelectric effect. *Physical Review*, 89(5):990, 1953.

[36] A. V. D. Beukel. On the theory of the acoustoelectric effect. *Applied Scientific Research, Section A*, 5(1):459, 1956.

[37] G. Weinreich. Acoustodynamic Effects in Semiconductors. *Physical Review*, 104(2):321, 1956.

[38] G. Weinreich, T. Sanders, and H. White. Acoustoelectric effect in n-type germanium. *Physical Review*, 114(1):33, 1959.

[39] G. Quentin and J. M. Thuillier. Contribution of acoustoelectric current to current saturation in piezoelectric semiconductors. *Physics Letters*, 23(1):42, 1966.

[40] H. Ozaki and N. Mikoshiba. Nonlinear theory of current saturation in piezoelectric semiconductors. *Journal of the Physical Society of Japan*, 21(12):2486, 1966.

[41] W. H. Haydl. Current oscillations in piezoelectric semiconductors. *Journal of Applied Physics*, 38(11):4295, 1967.

[42] P. Tien. Nonlinear thoery of ultrasonic wave amplification and current saturation in piezoelectric semiconductors. *Physical Review*, 171(3):970, 1968.

[43] G. Macchiarella and G. B. Stracca. SAW devices for telecommunications: examples and applications. *Ultrasonics Symposium*, page 247, 1982.

[44] D. S. Ballantine, R. M. White, S. J. Martin, A. J. Ricco, E. T. Zellers, G. C. Frye, and H. Wohltjen. Acoustic wave sensors: Theory, design, and physico-chemical applications. *Academic Press, San Diego*, 1997.

[45] H. Zu, Y. Wang, and J. Xie. Surface acoustic wave mass sensor based on 128° YX-cut lithium niobate for thermogravimetric analysis. *IEEE International Ultrasonics Symposium Proceedings*, page 2544, 2014.

[46] C. Caliendo, E. Verona, and V. I. Anisimkin. Surface acoustic wave humidity sensors: A comparison between different types of sensitive membrane. *Smart Materials and Structures*, 6(6):707, 1997.

[47] I. Voiculescu and A. N. Nordin. Acoustic wave based MEMS devices for biosensing applications. *Biosensors & Bioelectronics*, 33(1):1, 2012.

[48] C. H. W. Barnes, J. M. Shilton, and A. M. Robinson. Quantum computation using electrons trapped by surface acoustic waves. *Physical Review B*, 62(12):8410, 2000.

[49] V. Gurevich, V. Pevzner, and G. Iafrate. Giant quantum oscillations of acoustoelectric effect in nanostructures. *Physical Review Letters*, 77(18):3881, 1996.

[50] V. Gurevich, V. Kozub, and V. Pevzner. Acoustoelectric effect in nanostructures: Role of quasimomentum balance. *Physical Review B*, 58(19):13088, 1998.

[51] G. Gumbs, G. R. Aizin, and M. Pepper. Coulomb interaction of two electrons in the quantum dot formed by the surface acoustic wave in a narrow channel. *Physical Review B*, 60(20):954, 1999.

[52] Y. Levinson, O. Entin-Wohlman, and P. Wölfle. Acoustoelectric current and pumping in a ballistic quantum point contact. *Physical Review Letters*, 85(3):634, 2000.

[53] C. Wiele, F. Haake, C. Rocke, and A. Wixforth. Photon trains and lasing: The periodically pumped quantum dot. *Physical Review A*, 58(4):R2680, 1998.

[54] T. J. B. M Janssen and A. Hartland. Accuracy of quantized single-electron current in a one-dimensional channel. *Physica B: Condensed Matter*, 284-288(2):1790, 2000.

[55] L. J. Geerligs, V. F. Anderegg, and P. A. M. Holweg. Frequency-locked turnstile device for single electrons. *Physical Review Letters*, 64(22):2691, 1990.

[56] S. Hermelin, S. Takada, M. Yamamoto, S. Tarucha, A. D. Wieck, L. Saminadayar, C. Bäuerle, and T. Meunier. Electrons surfing on a sound wave as a platform for quantum optics with flying electrons. *Nature*, 477(7365):435, 2011.

[57] V. Kalinin. Passive wireless strain and temperature sensors based on SAW devices. *Radio and Wireless Conference, IEEE*, page 187, 2004.

[58] W. P. Jakubik. Surface acoustic wave-based gas sensors. *Thin Solid Films*, 520(3):986, 2011.

[59] S. Mouras, A. Hamm, D. Djurado, and J. C. Cousseins. Synthesis of first

stage graphite intercalation compounds with fluorides. *Revue de Chimie Minerale*, 24(5):572, 1987.

[60] P. R. Wallace. The band theory of graphite. *Physical Review*, 71(9):622, 1947.

[61] L. D. Landau. Zur theorie der phasenumwandlungen ii. *Physikalische Zeitschrift der Sowjetunion*, 11:26, 1937.

[62] R. E. Peierls. Quelques proprietes typiques des corpses solides. *Annales de l'Institut Henri Poincaré*, 5:177, 1935.

[63] B. J. Alder and T. E. Wainright. Phase transition in elastic disks. *Physical Review*, 127(2):359, 1962.

[64] N. D. Mermin. Crystalline order in two dimensions. *Physical Review*, 176(1):250, 1968.

[65] J. A. Venables, G. D. T. Spiller, and M. Hanbücken. Nucleation and growth of thin films. *Reports on Progress in Physics*, 47(4):399, 1984.

[66] M. S. Dresselhaus and G. Dresselhaus. Intercalation compounds of graphite. *Advances in Physics*, 51(1):1, 2002.

[67] J. C. Meyer, A. K. Geim, M. I. Katsnelson, K. S. Novoselov, T. J. Booth, and S. Roth. The structure of suspended graphene sheets. *Nature*, 446(7131):60, 2007.

[68] Z. Ni, H. Bu, M. Zou, H. Yi, K. Bi, and Y. Chen. Anisotropic mechanical properties of graphene sheets from molecular dynamics. *Physica B*, 405(5):1301, 2010.

[69] L. A. Falkovsky. Optical properties of graphene. *Journal of Physics: Conference Series*, 129(1):012004, 2008.

[70] A. S. Mayorov, R. V. Gorbachev, and S. V. Morozov. Micrometer-scale ballistic transport in encapsulated graphene at room temperature. *Nano Letters*, 11(6):2396, 2011.

[71] S. V. Morozov, K. S. Novoselov, M. I. Katsnelson, F. Schedin, D. C. Elias, J. A. Jaszczak, and A. K. Geim. Giant intrinsic carrier mobilities in graphene and its bilayer. *Physical Review Letters*, 100(1):016602, 2008.

[72] C. N. R. Rao, A. K. Sood, K. S. Subrahmanyam, and A. Govindaraj. Graphene: The new two-dimensional nanomaterial. *Angewandte Chemie International Edition*, 48(42):7752, 2009.

[73] N. Marzari, O. L. Sanchez, Y. Kung, D. Krasnozhon, M. Chen, S. Bertolazzi, P. Gillet, A. Fontcuberta, A. Radenovic, and A. Kis. Large-area epitaxial monolayer $MoS_2$. *ACS Nano*, 9(4):4611–4620, 2015.

[74] L. Tao, E. Cinquanta, D. Chiappe, C. Grazianetti, M. Fanciulli, M. Dubey, A. Molle, and D. Akinwande. Silicene field-effect transistors operating at room temperature. *Nature nanotechnology*, 10(3):227–231, 2015.

[75] E. Bianco, S. Butler, S. Jiang, and O. D. Restrepo. Stability and exfoliation of germanane: a germanium graphane analogue. *Acs Nano*, 7(5):4414–4421, 2013.

[76] X. Miao, S. Tongay, and M. K. Petterson. High efficiency graphene solar cells by chemical doping. *Nano Letters*, 12(6):2475, 2012.

[77] B. Seger and P. V. Kamat. Electrocatalytically active graphene-platinum nanocomposites. Role of 2-D carbon support in PEM fuel cells. *The Journal of Physical Chemistry C*, 113(19):7990, 2009.

[78] S. Watcharotone, D. A. Dikin, and S. Stankovich. Graphene-silica composite thin films as transparent conductors. *Nano Letters*, 7(7):1888, 2007.

[79] M. D. Stoller, S. Park, Y. Zhu, J. An, and R. S. Ruoff. Graphene-based ultracapacitors. *Nano Letters*, 8(10):3498, 2008.

[80] M. Dragoman and D. Dragoman. Graphene-based quantum electronics. *Progress in Quantum Electronics*, 33(6):165, 2009.

[81] F. Schedin, A. K. Geim, S. V. Morozov, E. W. Hill, P. Blake, M. I. Katsnelson, and K. S. Novoselov. Detection of individual gas molecules adsorbed on graphene. *Nature Materials*, 6(10):652, 2007.

[82] V. Dua, S. P. Surwade, S. Ammu, S. R. Agnihotra, S. Jain, K. E. Roberts, S. Park, R. S. Ruoff, and Sanjeev K. Manohar. All-organic vapor sensor using inkjet-printed reduced graphene oxide. *Angewandte Chemie International Edition*, 49(12):2154, 2010.

[83] G. Eda and M. Chhowalla. Graphene-based composite thin films for electronics. *Nano Letters*, 9(2):814, 2009.

[84] J. Wu, W. Pisula, and K. Müllen. Graphenes as potential material for electronics. *Chemical Reviews*, 107(3):718, 2007.

[85] F. D. M. Haldane. Model for a quantum Hall effect without Landau levels: Condensed-matter realization of the "parity anomaly". *Physical Review Letters*, 61(18):2015, 1988.

[86] E. Fradkin, E. Dagotto, and D. Boyanovsky. Physical realization of the parity anomaly in condensed matter physics. *Physical Review Letters*, 57(23):1, 1986.

[87] D. H. Kim, P. A. Lee, and X. G. Wen. Massless Dirac fermions, gauge fields, and underdoped cuprates. *Physical Review Letters*, 79(11):2109, 1997.

[88] D. Sheng, L. Sheng, and Z. Weng. Quantum Hall effect in graphene: Disorder effect and phase diagram. *Physical Review B*, 73(23):233406, 2006.

[89] N. Peres, F. Guinea, and A. H. C. Neto. Electronic properties of disordered two-dimensional carbon. *Physical Review B*, 73(12):125411, 2006.

[90] V. V. Cheianov, V. Fal'ko, and B. L. Altshuler. The focusing of electron flow and a Veselago lens in graphene p-n junctions. *Science*, 315(5816):1252, 2007.

[91] S. Chen, W. Cai, D. Chen, Y. Ren, X. Li, Y. Zhu, J. Kang, and R. S. Ruoff. Adsorption/desorption and electrically controlled flipping of ammonia molecules on graphene. *New Journal of Physics*, 12(12):125011, December 2010.

[92] J. H. Chen, C. Jang, S. Adam, M. S. Fuhrer, E. D. Williams, and M. Ishigami. Charged-impurity scattering in graphene. *Nature Physics*, 4(5):377, 2008.

[93] O. Leenaerts, B. Partoens, and F. Peeters. Adsorption of $H_2O$, $NH_3$, CO, $NO_2$, and NO on graphene: A first-principles study. *Physical Review B*, 77(12):125416, March 2008.

[94] C. R. Dean, A. F. Young, I. Meric, C. Lee, L. Wang, S. Sorgenfrei, K. Watanabe, T. Taniguchi, P. Kim, K. L. Shepard, and J. Hone. Boron nitride substrates for high-quality graphene electronics. *Nature Nanotechnology*, 5(10):722, 2010.

[95] A. Reina, X. Jia, J. Ho, D. Nezich, H. Son, V. Bulovic, M. S. Dresselhaus, and J. Kong. Large area, few-layer graphene films on arbitrary substrates by chemical vapor deposition. *Nano Letters*, 9(1):30, 2009.

[96] X. Li, W. Cai, J. An, S. Kim, J. Nah, D. Yang, R. Piner, A. Velamakanni, I. Jung, E. Tutuc, S. K. Banerjee, L. Colombo, and R. S. Ruoff. Large-area synthesis of high-quality and uniform graphene films on copper foils. *Science*, 324(5932):1312, 2009.

[97] N. Petrone, C. R. Dean, I. Meric, A. M. van der Zande, P. Y Huang, L. Wang, D. Muller, K. L. Shepard, and J. Hone. Chemical vapor deposition-derived graphene with electrical performance of exfoliated graphene. *Nano Letters*, 12(6):2751, 2012.

[98] J. W. Orton and M. Powell. The Hall effect in polycrystalline and powered semiconductors. *Reports on Progress in Physics*, 43(11):1263, 1980.

[99] Y. Ogawa, K. Komatsu, K. Kawahara, M. Tsuji, K. Tsukagoshi, and H. Ago. Struc-

ture and transport properties of the interface between CVD-grown graphene domains. *Nanoscale*, 6(13):7288, 2014.

[100] D. K. Efetov and P. Kim. Controlling electron-phonon interactions in graphene at ultrahigh carrier densities. *Physical Review Letters*, 105(25):256805, 2010.

[101] J. Chen, C. Jang, S. Xiao, M. Ishigami, and M. S. Fuhrer. Intrinsic and extrinsic performance limits of graphene devices on $SiO_2$. *Nature Nanotechnology*, 3(4):206, 2008.

[102] J. Heo, H. J. Chung, S. Lee, H. Yang, D. H. Seo, J. K. Shin, U. Chung, S. Seo, E. H. Hwang, and S. D. Sarma. Nonmonotonic temperature dependent transport in graphene grown by chemical vapor deposition. *Physical Review B*, 84(3):035421, 2011.

[103] Q. Li, E. H. Hwang, and S. D. Sarma. Disorder-induced temperature-dependent transport in graphene: Puddles, impurities, activation, and diffusion. *Physical Review B*, 84(11):115442, 2011.

[104] E. H. Hwang, S. Adam, and S. Das Sarma. Carrier transport in two-dimensional graphene layers. *Physical Review Letters*, 98(18):186806, 2007.

[105] C. Lee, X. Wei, J. W. Kysar, and J. Hone. Measurement of the elastic properties and intrinsic strength of monolayer graphene. *Science*, 321(5887):385, 2008.

[106] R. Ansari, B. Motevalli, A. Montazeri, and S. Ajor. Fracture analysis of monolayer graphene sheets with double vacancy defects via md simulation. *Solid State Communications*, 151(17):1141, 2011.

[107] L. M. Viculis, J. J. Mack, O. M. Mayer, H. T. Hahn, and R. B. Kaner. Intercalation and exfoliation routes to graphite nanoplatelets. *Journal of Materials Chemistry*, 15(9):974, 2005.

[108] C. Riedl, C. Coletti, and U. Starke. Structural and electronic properties of epitaxial

graphene on SiC (0001): A review of growth, characterization, transfer doping and hydrogen intercalation. *Journal of Physics D: Applied Physics*, 43(37):374009, 2010.

[109] K. S. Kim, Y. Zhao, H. Jang, S. Y. Lee, J. M. Kim, K. S Kim, J. Ahn, P. Kim, J. Choi, and B. H. Hong. Large-scale pattern growth of graphene films for stretchable transparent electrodes. *Nature*, 457(7230):706, 2009.

[110] S. Bae, H. Kim, Y. Lee, X. Xu, J. Park, Y. Zheng, J. Balakrishnan, T. Lei, H. R. Kim, Y. I. Song, Y. Kim, K. S. Kim, B. Ozyilmaz, J. Ahn, B. H. Hong, and S. Iijima. Roll-to-roll production of 30-inch graphene films for transparent electrodes. *Nature Nanotechnology*, 5(8):574, 2010.

[111] J. W. Suk, A. Kitt, C. W. Magnuson, Y. Hao, S. Ahmed, J. An, A. K. Swan, B. B Goldberg, and R. S. Ruoff. Transfer of CVD-grown monolayer graphene onto arbitrary substrates. *ACS Nano*, 5(9):6916, 2011.

[112] L. G. D. Arco, Y. Zhang, and C. W. Schlenker. Continuous, highly flexible, and transparent graphene films by chemical vapor deposition for organic photovoltaics. *ACS Nano*, 4(5):2865, 2010.

[113] F. Bonaccorso, Z. Sun, T. Hasan, and A. C. Ferrari. Graphene photonics and optoelectronics. *Nature Photonics*, 4(9):611, 2010.

[114] F. Xia, T. Mueller, Y. Lin, A. Valdes-Garcia, and P. Avouris. Ultrafast graphene photodetector. *Nature Nanotechnology*, 4(12):839, 2009.

[115] Y. Huang, X. Dong, Y. Shi, C. M. Li, L. Li, and P. Chen. Nanoelectronic biosensors based on CVD grown graphene. *Nanoscale*, 2(8):1485, 2010.

[116] Y. Wang, Y. Shao, D. W. Matson, J. Li, and Y. Lin. Nitrogen-doped graphene and its biosensing. *ACS Nano*, 4(4):1790, 2010.

[117] R. P. Vidano and D. B. Fischbach. Observation of raman band shifting with excita-

tion wavelength for carbons and graphites. *Solid State Communications*, 39(2):341, 1981.

[118] C. Thomsen and S. Reich. Double resonant Raman scattering in graphite. *Physical Review Letters*, 85(24):5214, 2000.

[119] J. H. Cho, J. Lee, Y. He, B. S. Kim, T. P. Lodge, and C. D. Frisbie. High-capacitance ion gel gate dielectrics with faster polarization response times for organic thin film transistors. *Advanced Materials*, 20(4):686, 2008.

[120] J. Temmyo, I. Kotaka, T. Inamura, and S. Yoshikawa. Precise measurement of SAW propagation velocity on lithium niobate. *IEEE Transactions*, 27(4):218, 1980.

[121] R. L. Willett, K. W. West, and L. N. Pfeiffer. Transition in the correlated 2D electron system induced by a periodic density modulation. *Physical Review Letters*, 78(23):4478, 1997.

[122] O. D. D. Couto, S. Lazić, F. Iikawa, J. A. H. Stotz, U. Jahn, R. Hey, and P. V. Santos. Photon anti-bunching in acoustically pumped quantum dots. *Nature Photonics*, 3(11):645, 2009.

[123] P. V. Santos, T. Schumann, M. H. Oliveira, J. M. J. Lopes, and H. Riechert. Acoustoelectric transport in epitaxial monolayer graphene on SiC. *Applied Physics Letters*, 102(22):221907, 2013.

[124] K. L. Grosse, M. Bae, F. Lian, E. Pop, and W. P. King. Nanoscale Joule heating, Peltier cooling and current crowding at graphene-metal contacts. *Nature Nanotechnology*, 6(5):287, 2011.

[125] T. O. Wehling, A. I. Lichtenstein, and M. I. Katsnelson. First-principles studies of water adsorption on graphene: The role of the substrate. *Applied Physics Letters*, 93(20):202110, 2008.

[126] H. Wang, Y. Wu, C. Cong, J. Shang, and T. Yu. Hysteresis of electronic transport in graphene transistors. *ACS Nano*, 4(12):7221, 2010.

[127] M. Ishigami, J. H. Chen, W. G. Cullen, and M. S. Fuhrer. Atomic Structure of Graphene on $SiO_2$. *Nano Letters*, 7(6):1643, 2007.

[128] A. Pirkle, J. Chan, A. Venugopal, D. Hinojos, C. W. Magnuson, S. McDonnell, L. Colombo, E. M. Vogel, R. S. Ruoff, and R. M. Wallace. The effect of chemical residues on the physical and electrical properties of chemical vapor deposited graphene transferred to $SiO_2$. *Applied Physics Letters*, 99(12):122108, 2011.

[129] M. Rotter, A. Wixforth, W. Ruile, D. Bernklau, and H. Riechert. Giant acoustoelectric effect in GaAs/$LiNbO_3$ hybrids. *Applied Physics Letters*, 73(15):2128, 1998.

[130] V. Fal'ko, S. Meshkov, and S. Iordanskii. Acoustoelectric drag effect in the two-dimensional electron gas at strong magnetic field. *Physical Review. B*, 47(15):9910, 1993.

[131] M. Levy, J. Schmidt, A. Schenstrom, M. Revzen, A. Ron, B. Shapiro, and C.G. Kuper. Ultrasonic attenuation and the resistive transition in a superconducting granular lead film. *Physical Review B*, 34(3):1508, 1986.

[132] P. Nemes-Incze and K. J. Yoo. Revealing the grain structure of graphene grown by chemical vapor deposition. *Applied Physics Letters*, 99(2):023104, 2011.

[133] Y. W. Tan, Y. Zhang, K. Bolotin, Y. Zhao, S. Adam, E. H. Hwang, S. D. Sarma, H. L. Stormer, and P. Kim. Measurement of scattering rate and minimum conductivity in graphene. *Physical Review Letters*, 99(24):246803, 2007.

[134] J. Schiefele, F. Sols, and F. Guinea. Temperature dependence of the conductivity of graphene on boron nitride. *Physical Review B*, 85(19):195420, 2012.

[135] L. Bandhu, L. M. Lawton, and G. R. Nash. Macroscopic acoustoelectric charge transport in graphene. *Applied Physics Letters*, 103(13):133101, 2013.

[136] I. J. Luxmoore, C. Adlem, T. Poole, L. M. Lawton, N. H. Mahlmeister, and G. R. Nash. Thermal emission from large area chemical vapor deposited graphene devices. *Applied Physics Letters*, 103(13):131906, 2013.

[137] Y. Zhang, V. W. Brar, C. Girit, A. Zettl, and M. F. Crommie. Origin of spatial charge inhomogeneity in graphene. *Nature Physics*, 5(10):722, 2009.

[138] H. S. Song, S. L. Li, H. Miyazaki, S. Sato, K. Hayashi, A. Yamada, N. Yokoyama, and K. Tsukagoshi. Origin of the relatively low transport mobility of graphene grown through chemical vapor deposition. *Scientific Reports*, 2(337):1, 2012.

[139] O. V. Yazyev and S. G. Louie. Electronic transport in polycrystalline graphene. *Nature Materials*, 9(10):806, 2010.

[140] A. Kumari, N. Prasad, P. K. Bhatnagar, P. C. Mathur, A. K. Yadav, C. V. Tomy, and C. S. Bhatia. Electrical transport properties of polycrystalline CVD graphene on $Si/SiO_2$ substrate. *Diamond and Related Materials*, 45(1):28, 2014.

[141] J. Ristein, S. Mammadov, and T. Seyller. Origin of doping in quasi-free-standing graphene on silicon carbide. *Physical Review Letters*, 108(24):246104, 2012.

[142] R. S. Weis and T. K. Gaylord. Lithium niobate: Summary of physical properties and crystal structure. *Applied Physics A*, 37(4):191, 1985.

[143] K. S. Novoselov, A. K. Geim, S. V. Morozov, D. Jiang, M. I. Katsnelson, I. V. Grigorieva, S. V. Dubonos, and A. A. Firsov. Two-dimensional gas of massless dirac fermions in graphene. *Nature*, 438(10):197, 2005.

[144] G. J. Milburn. Quantum optical Fredkin gate. *Physical Review Letters*, 62(18):2124, 1989.

[145] C. L. Foden, V. I. Talyanskii, G. J. Milburn, M. L. Leadbeater, and M. Pepper. High-frequency acoustoelectric single-photon source. *Physical Review A*, 62(1):011803, 2000.

[146] C. Lu, Q. Fu, S. Huang, and J. Liu. Polymer electrolyte-gated carbon nanotube field-effect transistor. *Nano Letters*, 4(4):623, 2004.

[147] V. E. Dorgan, M. Bae, and E. Pop. Mobility and saturation velocity in graphene on $SiO_2$. *Applied Physics Letters*, 97(8):082112, 2010.

[148] B. Chakraborty, A. Das, and A. K. Sood. The formation of a p-n junction in a polymer electrolyte top-gated bilayer graphene transistor. *Nanotechnology*, 20(36):365203, 2009.

[149] Y. Yao, X. Chen, J. Zhu, B. Zeng, Z. Wu, and X. Li. The effect of ambient humidity on the electrical properties of graphene oxide films. *Nanoscale Research Letters*, 7(363):1, 2012.

[150] J. Zhu, Y. Chen, G. Saraf, N. W. Emanetoglu, and Y. Lu. Voltage tunable surface acoustic wave phase shifter using semiconducting/piezoelectric ZnO dual layers grown on r-$Al_2O_3$. *Applied Physics Letters*, 89(10):103513, 2006.

[151] A. J. Budreau, P. H. Carr, and J. H. Silva. New configuration for electronically variable SAW delay line. *Proceedings IEEE Ultrasonics Symposium*, page 399, 1982.